UNIVERSITÉ DE GENÈVE
Département de Physique
de la Matière Quantique

FACULTÉ DES SCIENCES
Professeur
Alberto F. Morpurgo

Optoelectronic Phenomena in 2D Materials and Heterostructures

THÈSE

*présentée à la Faculté des Sciences de l'Université de Genève
pour obtenir le grade de docteur ès Sciences, mention Physique*

par

Daniil Domaretskiy
de
Astana (Kazakhstan)

Thèse n° 5653

GENÈVE
Atelier d'impression ReproMail
2022

UNIVERSITÉ
DE GENÈVE

FACULTÉ DES SCIENCES

DOCTORAT ÈS SCIENCES, MENTION PHYSIQUE

Thèse de Monsieur Daniil DOMARETSKIY

intitulée :

«Optoelectronic Phenomena in 2D Materials and Heterostructures»

La Faculté des sciences, sur le préavis de Monsieur A. MORPURGO, professeur ordinaire et directeur de thèse (Département de physique de la matière quantique), Monsieur J.-M. TRISCONE, professeur ordinaire (Département de physique de la matière quantique), Monsieur C. BERTHOD, docteur (Département de physique de la matière quantique), Monsieur F. KOPPENS, professeur (Institut de Ciències Fotòniques, Mediterranean Technology Park, Castelldefels, Spain) et Monsieur R. GORBACHEV, professeur (National Graphene Institute, University of Manchester, Manchester, United Kingdom), autorise l'impression de la présente thèse, sans exprimer d'opinion sur les propositions qui y sont énoncées.

Genève, le 31 mai 2022

Thèse - 5653 -

Le Doyen

N.B. - La thèse doit porter la déclaration précédente et remplir les conditions énumérées dans les "Informations relatives aux thèses de doctorat à l'Université de Genève".

To my maman, Svetlana

Lumi, potete piangere
non riderete più
Il cor, che lieto fu
nel duol si sente a frangere
Lumi, potete piangere

–Corradi, 1675.

Résumé

La dimensionnalité est l'une des pierres angulaires qui déterminent les propriétés fondamentales d'un matériau ainsi que ses applications. Pour un même matériau, ses atomes peuvent être disposés selon une structure différente : 0D, 1D, 2D, 3D. Connus depuis des siècles, les cristaux courants que l'on trouve dans la nature sont présents sous la forme 3D. Contrairement à leurs homologues tridimensionnels, les cristaux quasi-0D (molécules en cage) et -1D (nanotubes) sont des matériaux synthétiques. Ils représentent une classe de systèmes relativement nouvelle qui n'a été réalisée qu'à la fin du siècle dernier, au milieu des années 80 et au début des années 90. D'autre part, le comportement quasi-2D n'a été observé que dans des systèmes appelés hétérostructures où deux matériaux ou plus étaient réunis. Ces états quasi 2D ne pouvaient pas être observés séparément des interfaces de l'hétérostructure et l'on pensait que les cristaux 2D autoportants ne pouvaient théoriquement pas exister dans la nature. Les travaux théoriques de Peierls, Landau, Mermin et Wagner étaient la principale raison pour laquelle les gens pensaient qu'il ne pouvait y avoir de cristaux 2D. Cependant, la situation a changé en 2004, lorsque A. K. Geim et K. S. Novoselov (prix Nobel de physique 2010) ont isolé et étudié les propriétés de couches de carbone atomiquement fines jusqu'à la limite ultime de la monocouche, le graphène. Les propriétés électroniques du graphène ont stupéfié la communauté scientifique et ont suscité une immense attention pour ce matériau, si bien que de nombreux chercheurs ont rejoint la nouvelle ère de la ruée vers l'or.

La famille des matériaux qui peuvent être exfoliés jusqu'à la limite de l'épaisseur atomique ne se limite pas au graphène. Dès 2005, d'autres

matériaux 2D ont été obtenus et identifiés, tels que le nitrure de bore hexagonal (hBN, isolant à large bande), le disulfure de molybdène (MoS_2, semi-conducteur), le diséléniure de niobium ($NbSe_2$, supraconducteur) et le $Bi_2Sr_2CaCu_2O_x$ supraconducteur. Des calculs théoriques récents montrent qu'il existe près de 2000 matériaux 2D différents qui sont thermodynamiquement stables et peuvent donc être cultivés à la demande. Il n'y a pas si longtemps, de nombreux matériaux magnétiques 2D en couches (CrI_3, $MnPS_3$, $FePS_3$, etc.) ont été découverts grâce à une recherche continue. Ici, nous concentrons notre attention sur les dichalcogénures de métaux de transition. Dans cette famille, il y a plus de 60 composés avec diverses options structurelles qui démontrent une pléthore de propriétés. Ces matériaux sont connus depuis longtemps et étaient principalement utilisés comme lubrifiants solides. Déjà sous forme massive, ils démontrent une grande variété de propriétés électroniques. Dans la limite de la finesse atomique, par exemple, les cristaux monocouches de WTe_2 sont des isolants topologiques et les couches plus épaisses présentent une grande magnétorésistance ; le TiS_2 et le NbS_2 présentent des ondes de densité de charge ; le $TiSe_2$ présente une phase isolante excitonique. Le $PtSe_2$ désordonné présente des propriétés magnétiques similaires à celles du CrI_3. La famille TMD comprend également les semi-conducteurs MoS_2, $MoSe_2$, WS_2, et WSe_2– qui sont au cœur de l'intérêt de la thèse.

La thèse est consacrée aux phénomènes optoélectroniques dans les semi-conducteurs 2D et leurs hétérostructures de van der Waals. La palette des matériaux couverts dans la partie expérimentale est principalement présentée par les semi-conducteurs du groupe 6 des TMDs, et un monochalcogénure de métal de transition –InSe. En particulier, nous étudions les transitions optiques brillantes dans les hétérostructures de van der Waals de WS_2, MoS_2, $MoSe_2$ avec des cristaux d'InSe de différentes épaisseurs dans le *Chapter 5*. Ensuite, les cristaux de WSe_2, de graphène et de phosphorène rejoignent la palette de matériaux dans le *Chapitre 6*, où nous discutons d'une nouvelle approche pour observer les matériaux 2D avec la lumière réfléchie par diffusion. *Chapitre 7* est uniquement consacré aux mesures de transport dans les cristaux multicouches WSe_2. *Chapitres 2-4* fournissent au lecteur des bases théoriques et des méthodes expérimentales pour la compréhension et l'interprétation des résultats expérimentaux.

Les résultats expérimentaux commencent dans le *Chapitre 5* par la discussion des interfaces de van der Waals basées sur des matériaux 2D qui sont prometteurs pour l'optoélectronique, car les transitions entre couches entre différents composés permettent de personnaliser la réponse spectrale sur une large gamme. Nous soulignons que des problèmes tels que le décalage du réseau ou un léger désalignement des couches constitutives peuvent supprimer radicalement le couplage électron-photon pour ces transitions intercouches. Pour résoudre ces obstacles, nous concevons des interfaces de type II en assemblant des cristaux atomiquement minces dont le bas de la bande de conduction et le haut de la bande de valence se trouvent au point de contact, évitant ainsi tout décalage de momentum. Nous constatons que ces interfaces vdW présentent des transitions optiques radiatives indépendamment de la constante de réseau, de l'alignement rotationnel/translationnel des deux couches, ou du fait que les matériaux constitutifs soient des semi-conducteurs à gap direct ou indirect. Grâce à leur robustesse et à leur validité générale, nos résultats élargissent le champ d'application des futurs dispositifs optoélectroniques basés sur des matériaux bidimensionnels.

Dans le *Chapitre 6*, nous explorons une autre stratégie de détection des matériaux bidimensionnels, dans laquelle l'amélioration du contraste optique provient de l'utilisation de substrats optiquement inhomogènes, conduisant à une réflexion diffuse de la lumière. En raison de ses propriétés de polarisation particulières et de sa distribution angulaire, la lumière réfléchie de manière diffuse permet d'obtenir une forte amélioration du contraste par la mise en œuvre de schémas d'illumination-détection appropriés. Nous validons cette conclusion en effectuant une analyse quantitative détaillée du contraste optique, qui reproduit entièrement nos observations expérimentales sur plus de 60 monocouches, bicouches et tricouches de WSe_2. Nous validons également la stratégie proposée en étendant notre analyse aux cristaux de phosphorène, de InSe et de graphène atomiquement minces. Notre conclusion est que l'utilisation de la lumière réfléchie par diffusion pour détecter et identifier les couches atomiquement minces est une alternative intéressante au schéma de détection courant basé sur l'interférence de Fabry-Pérot, car elle permet de détecter les couches atomiquement minces sur des substrats autres que le Si/SiO_2 couramment utilisé, et elle peut offrir une sensibilité plus élevée en fonction du matériau 2D spécifique considéré.

Dans le *Chapitre 7*, nous avons réalisé des transistors à double grille ionique qui permettent l'application de très grands champs électriques nécessaires pour régler la structure de bande électronique des semi-conducteurs atomiquement minces à l'échelle eV. En utilisant ces dispositifs, nous montrons que la bande interdite de dichalcogénures de métaux de transition semi-conducteurs à quelques couches - de WSe_2 bicouche à heptalouche - peut être continuellement supprimée de 1.6 eV à zéro. Nos résultats illustrent un niveau de contrôle sans précédent de la structure de bande des semi-conducteurs 2D.

Acknowledgements

First of all, I would like to start with acknowledgements for my supervisor Prof. Alberto. F. Morpurgo for providing me the opportunity to do a Ph.D. thesis at the University of Geneva, and for a colossal reserve of patience when working together. I am also grateful to my colleagues and dearest friends Ignacio Gutiérrez-Lezama and Nicolas Ubrig, who supervised my work in the laboratory and helped me to grow not only as a scientist, but also as a person. Next, I thank Dr. Christophe Berthod who broadened my understanding of theory and prepared me for the candidacy exam. Also, I would like to acknowledge all our collaborators with whom we published papers.

Here, I would like to thank the committee members Prof. Frank Koppens, Prof. Roman Gorbachev, Prof. Jean-Marc Triscone, Dr. Christophe Berthod for the time and efforts to read and evaluate the thesis as well as for their role as jury members for my thesis defence.

While writing the acknowledgement section, I start to realize how much I am going to miss my colleagues and I will be forever grateful to them (Giulia, Margherita, Haijing, Florian, Enrico, Marc, Evgenii, Diego and Dumas, Hugo, David, Fengrui, Zhe, Gen, Marco, Ki, Young Woo, Lin, Fan, Chuanwu, and Dumitru). Each one of you already knows why and what for I thank them, so I will not disclose anything here.

It is also worth mentioning the friendly and mentally healthy atmosphere that has been maintained by Simone, Edoardo, Gianmarco, Irene, Andrew, and Julia from the neighboring office. I hope you will take care of the baby plants I gave you and that they will not die.

Apart from that, I thank my friend Il'ya –who has been following my path since the high school– for bringing me "luck" (even though I have never been a superstitious person) during my double-gating experiments on 4L-WSe_2 layers.

Contents

CHAPTER 1

General Introduction

1.1 2D materials and their van der Waals heterostructures

Dimensionality is one of the corner stones that determines fundamental properties of a material as well as its applications. For the same material, its atoms can be arranged in a different structure: 0D, 1D, 2D, 3D. Known for centuries, common crystals found in nature are present in the 3D form. Unlike the three-dimensional counterparts, quasi-0D (cage molecules) and -1D (nanotubes) crystals are synthetic materials. They represent a relatively new class of systems that was realised just at the end of the last century in the middle of the 80s and the beginning of 90s. On the other hand, quasi-2D behaviour was only observed in systems called heterostructures where two or more materials were brought together. Such quasi-2D states could not be observed separately from the heterostructure interfaces and it had been believed that freestanding 2D crystals could not exist in nature theoretically. Theoretical works of Peierls, Landau, Mermin, and Wagner were the main reason why people thought that there could not be 2D crystals [1]. However, the situation changed in 2004, when A. K. Geim and K. S. Novoselov (Nobel Prize in Physics 2010) isolated and studied properties of atomically thin carbon layers down to the ultimate monolayer limit –graphene [2]. The electronic properties of graphene stunned the scientific community and triggered immense attention to the material, so many researchers joined the new gold rush era [3].

Graphene is the thinnest material ever obtained. It is also a unique system to study various phenomena, even some unexpected ones for condensed matter physics such as “analogue gravity”, physics of black holes [4], Fizeau drag effect [5], quantum field theory in curved space-times, and Hawking effect [6] – the list goes on. In graphene, the charge carriers behave like massless fermions described by the relativistic Dirac equation [3, 7]. Even though charge carriers in graphene are not really relativistic because their speed is much smaller than the speed of light, their energy depends linearly on the momentum like for photons. This was revealed by the observation of new types of the integer quantum Hall effect that could only be described in terms of the Dirac fermions [2, 3]. Other relativistic effects such as Klein tunneling [8] that were believed as non-observable, were observed using devices based on graphene.

Another reason why the graphene boom happened was because of the highly accessible and straightforward way graphene was isolated from bulk crystal –graphite– and how it is identified. Being part of the so-called van der Waals (vdW) materials, graphite is a layered material where weak van der Waals forces hold individual graphene layers. Atoms within the individual monolayers, however, are held by strong covalent bonds. These properties allow cleaving the material across the vdW bonds into individual planes without affecting the surface of the crystal and creating no dangling bonds. To cleave the graphite crystal, there is no need of sophisticated equipment. In fact, many of us had performed this procedure as early as in the childhood by drawing with pencils on a piece of paper leaving numerous small atomically thin layers on it. As easy as writing on a paper, large enough graphene layers can be produced through the micro-mechanical cleavage technique by using a common consumable –a scotch tape. In this method, the top of the bulk crystal is removed by an adhesive tape and then the tape together with the crystals on it pressed against the substrate. When the adhesion of the crystal to the substrate is stronger than that between layers of the crystal, graphene is deposited onto the substrate surface via this extremely straightforward and easy technique. The accessibility of the scotch-tape exfoliation played an essential role in the rapid development of the 2D material field.

The family of materials that can be exfoliated down to the atomically thin limit is not limited to graphene. Already in 2005, there were obtained and identified other 2D materials [9] such as hexagonal boron nitride (hBN, wide band insulator), molybdenum disulfide (MoS_2, semiconductor), niobium diselenide ($NbSe_2$, superconductor), and superconducting $Bi_2Sr_2CaCu_2O_x$. Recent theoretical calculations show that there are almost 2000 different 2D materials [10] that are thermodynamically stable and therefore can be grown on demand. Not long time ago, plenty of 2D layered magnetic materials (CrI_3, $MnPS_3$, $FePS_3$, etc.) [11] were discovered with an ongoing research. Here, we focus our attention to Transition Metal Dichalcogenides (TMDs) [7, 12, 13]. In this family, there are more than 60 compounds with various structural options that demostrate a plethora of properties [7, 12–19]. These materials have been known for a long time and were mainly used as solid lubricants. Already in the bulk form, they demonstrate a wide variety of electronic properties. In the atomically thin limit, for instance, monolayer WTe_2 crystals are topological insulators and thicker layers show a large magnetoresistance [20–23]; TiS_2 and NbS_2 exhibit charge density waves [24]; $TiSe_2$ shows excitonic insulator phase [25]. Disordered $PtSe_2$ demonstrates magnetic properties [19] similar to the ones of CrI_3. The TMD family also includes semiconductors –MoS_2, $MoSe_2$, WS_2, and WSe_2– that are in the core interest of the thesis.

The band structure of semiconducting TMDs is what makes them so attractive. One of its peculiarities is the direct band gap in the monolayer form of TMDs [12, 15]. The band gap strongly depends on the selected material, and it covers a broad energy range reaching the infrared regions (favorable for telecom applications). Another point to mention is that the band gap can also be tuned by changing the thickness of TMDs. However, when changing the thickness of the layers from a monolayer to a bilayer and thicker, TMDs undergo a crossover from direct to indirect band gap semiconductors [7, 12, 13]. This plays a crucial role in the optical properties of TMDs.

The optical response of TMDs is dominated by the bound states of optically excited electrons and holes known as excitons [26, 27]. Due to the 2D nature and a weak dielectric screening in these materials, the excitons have very large binding energy (as large as 0.5 eV), a few orders of magnitude larger than in the conventional III-V systems such as GaAs. This makes TMDs a versatile platform to observe excitonic effects at room temperature.

Isolated atomically thin materials have already brought a lot of new possibilities to study novel phenomena that were either difficult or even impossible to observe with conventional systems. The options expand when 2D materials are reassembled into on-demand designed heterostructures (HTs) in a vertical stack [28, 29]. The same weak van der Waals forces that allow exfoliation of the 2D layers give the possibility to re-stack different layered materials on top of each other and hold them together. This type of interaction between the layers lifts limitations on the lattice parameters and the crystalline structure of the stacked materials as compared to conventional heterostructures based on III-V semiconductors [30] or

LAO/STO systems [31]. Such an absence of constraints for van der Waals heterostructures implies that all layered materials can be combined together, facilitating the possibility to engineer properties by design [29, 32–41]. With constantly improving fabrication techniques, new tools for designing material properties have become available for van der Waals heterostructures. For instance, control of the relative alignment between the layers in vdW HTs such as "magic" angle twisted bilayer graphene [42] and twisted TMDs [43] have opened up new routes to study Moire superlattices with extremely rich physics. Additionally, vdW heterostructures of semiconducting TMDs have demonstrated that the band gap of the HTs can be varied on the eV scale by choosing appropriate materials [35, 37, 44]. With the ongoing expansion of the 2D materials family, novel heterostructures emerge, and so do the new phenomena.

Since discovering graphene, the interest in 2D materials and later in van der Waals heterostructures has grown exponentially across multidisciplinary topics, with thousands of papers published each year. The wide range of physical properties of 2D materials makes them very promising for the current technology, and there is a hope to realize integrated electronic circuits based exclusively on 2D materials. Almost every new 2D material brings new physical phenomena that are expanded even further by combining the novel materials with the existing ones. This impressive progress shows no sign of slowing down and a growing effort is devoted to employing systems based on atomically thin layers to realize structures with desired properties for many more future technological applications [13, 16, 17, 45].

1.2 Thesis Outline

The thesis is devoted to optoelectronic phenomena in 2D semiconductors and their van der Waals heterostructures. The palette of materials covered in the experimental part is mainly presented by semiconductors of group 6 of TMDs, and a transition metal monochalcogenide –InSe. In particular, we investigate bright optical transitions in van der Waals heterostructures of WS_2, MoS_2, $MoSe_2$ with InSe crystals of various thickness in *Chapter 5*. Next, WSe_2, Graphene and Phosphorene crystals join the palette of materials in *Chapter 6*, where we discuss a new approach to observe 2D materials with diffusively reflected light. *Chapter 7* is solely dedicated to the transport measurements in WSe_2 multilayer crystals. *Chapters 2-4* provide the reader with a foundation in theory and experimental methods for the comprehension and interpretation of the experimental results.

The first of the introductory chapters –*Chapter 2*– acquaints the reader with the physical properties of the materials that we have studied. In the beginning, we discuss the structural and electronic properties of 2D semiconductors. *Sections 2.1-2.4* are devoted to transition metal dichalcogenides, while *Section 2.5* is dedicated to InSe. In these sections, significant attention is drawn to the peculiarity of the band structure and its sensitivity to the thickness of 2D crystals. Additionally, in *Sections 2.4*, we stress that strong perpendicular electric fields can provide an additional "knob" to alter the band structure. In particular, electric fields of a few V/nm can completely quench the band gap of TMDs.

Having discussed structural and electronic properties of the studied 2D semiconductors, we then move to their optical response, which is dominated by the bound electron-hole pairs – excitons, as we discuss in *Section 2.6*. We point to the pronounced peculiarities of 2D excitons –compared to their 3D counterparts– and give a general overview of their key features. Importantly, we bring particular focus on the radiative recombination of excitons.

In the last two sections of the chapter (*Section 2.7-2.8*), the discussion is devoted to van der Waals (vdW) heterostructures (HTs) of semiconductors and interlayer excitons. First, we discuss the advantages of vdW HTs over the conventional heterojunctions of semiconductors. The cornerstone of the discussion is the band alignment of individual semiconductors in HTs since the electronic structure determines physical properties of the devices based on the HTs. Later, we draw the attention to interlayer excitons formed in type II HTs and their benefits as compared to their intralyer counterparts. Most of all, in the last section we cover the aspects that are important for efficient light emission from the interlayer excitons.

Chapter 3 introduces the reader to the electrostatic gating technique that is widely used in the transport measurements of the thesis. Here, we first review key aspects of field-effect transitors (FETs) and their operational regimes. Later, having established the basic notions of FETs, we expand the discussion further by introducing ionic gating and elaborating how this type of gating is exploited as a spectroscopic technique. Finally, the last section of the chapter facilitates the understanding of double ionic gating that enables the application of very large electric fields, which have not been accessible with conventional FETs.

Chapter 4 focuses on experimental methods used in this work. Here, we describe essential fabrication steps of our high quality devices and van der Waals heterostructures. Notably, we provide a detailed overview of how we obtain and identify atomically thin crystals as well as how we manipulate them and assemble heterostructures. In addition, we cover basics of electron-beam lithography and contact deposition. At last, the reader is familiarized with the transport and optical measurements performed in this thesis.

The experimental results start in *Chapter 5* with the discussion of van der Waals interfaces based on 2D materials that are promising for optoelectronics, as interlayer transitions between different compounds allow tailoring the spectral response over a broad range. We point out that issues such as lattice mismatch or a small misalignment of the constituent layers can drastically suppress electron-photon coupling for these interlayer transitions. To solve addressed obstacles, we engineer type-II interfaces by assembling atomically thin crystals that have the bottom of the conduction band and the top of the valence band at the Γ-point, thus avoiding any momentum mismatch. We find that these vdW interfaces exhibit radiative optical transitions irrespective of lattice constant, rotational/translational alignment of the two layers, or whether the constituent materials are direct or indirect gap semiconductors. Being robust and of general validity, our results broaden the scope of future optoelectronics device applications based on two-dimensional materials.

In *Chapter 6*, we explore an alternative detection strategy of 2D materials, in which the enhancement of optical contrast originates from the use of optically inhomogeneous substrates, leading to diffusively reflected light. Owing to its peculiar polarization properties and to its angular distribution, diffusively reflected light allows a strong contrast enhancement to be achieved through the implementation of suitable illumination-detection schemes. We validate this conclusion by carrying out a detailed quantitative analysis of optical contrast, which fully reproduces our experimental observations on over 60 WSe_2 mono-, bi-, and trilayers. We further validate the proposed strategy by extending our analysis to atomically thin phosphorene, InSe, and graphene crystals. Our conclusion is that the use of diffusively reflected light to detect and identify atomically thin layers is an interesting alternative to the common detection scheme based on Fabry-Pérot interference, because it enables atomically thin layers to be detected on substrates others than the commonly used Si/SiO_2, and it may offer higher sensitivity depending on the specific 2D material considered.

In *Chapter 7* we have realized double ionic gated transistors that enable the application of very large electric fields needed to tune the electronic band structure of atomically thin semiconductors on the eV scale. Using these devices, we show that the band gap of few-layer semiconducting transition metal dichalcogenides –from bilayer to heptalayer WSe_2– can be continuously suppressed from 1.6 eV to zero. Our results illustrate an unprecedented level of control on the band structure of 2D semiconductors.

CHAPTER 2

Optoelectronic properties of 2D semiconductors and their heterostructures

In this Chapter we give an overview of properties of the 2D materials studied in the thesis: TMDs, InSe, and their heterostructures.

2.1 Composition and structure of semiconducting TMDs

Transition metal dichalcogenides (TMDs) is a family of materials with a general chemical formula of MX_2, where M stands for a transition metal and X denotes chalcogens. The palette of TMDs is composed of over 60 different materials (see Fig. 2.1) that give rise to a broad spectrum of properties due to different choices for Metal and Chalcogen atoms. Here, we discuss semiconductors from the Group 6. In these layered semiconductors, metal and chalcogen atoms are strongly bound via covalent bonds within the layer forming Chalcogen-Metal-Chalcogen planes (shown in the top panel of Fig. 2.1) with a total thickness of 6.5 A [12]. Unlike the intralayer bonds, the coupling between individual layers is weak and governed by van der Waals forces. Coupling of the layers through such a weak interaction makes the isolation of atomically thin crystals feasible even down to its ultimate monolayer limit.

Aside from the chemical composition, the relative arrangement of atoms in space plays a central role when determining properties of a material.

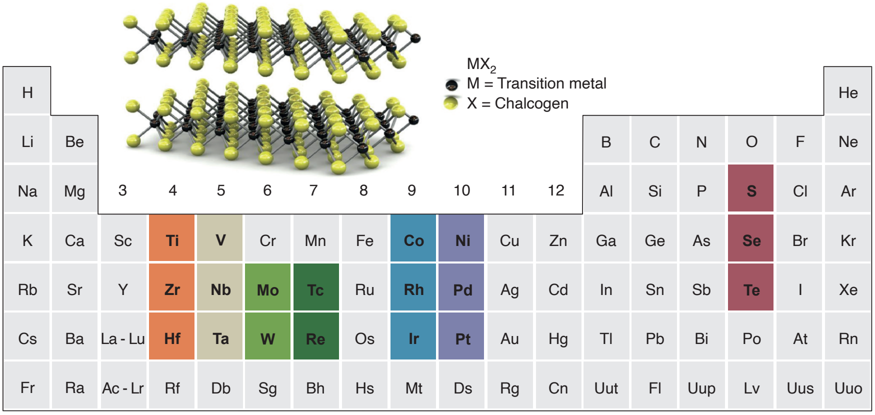

Figure 2.1: The Transition Metal Dichalcogendes family. The top inset shows a typical schematic of layered TMD with the chemical formula MX$_2$. The transition metals (M) are represented as dark balls, while the chalcogen atoms (X) are shown as yellow balls. The bottom panel shows various groups of transition metals and chalcogens (marked with violet squares) in the Periodic table of elements. In this thesis, we use semiconducting Mo- and W- (marked with light green squares) based TMDs. Adapted from Ref. [12].

Within a monolayer, the atoms in the Chalcogen-Metal-Chalcogen planes are arranged in one of the two possible coordinations – trigonal-prismatic or octahedral– as depicted in Fig. 2.2**A-B**. In the trigonal-prismatic arrangement, the chalcogen atoms of the bottom and the top planes are located on top of each other (mirrored relatively to the M plane) and results in the lack of inversion symmetry as shown in Fig. 2.2**A**. Contrary to that, in the octahedral coordination (see Fig. 2.2**B**), the position of chalcogen atoms in the bottom and top planes is inversion symmetric relative to the centres located at the position of M atoms. In practice, the exact coordination type depends on growth parameters.

In addition to the different arrangements of atoms within monolayers, the stacking order in thicker layers shows three different polytypes: 1T, 2H, and 3R [46, 47] as depicted in Figs. 2.2**C-E** [12]. The 1T polytype (Fig. 2.2**C**) is characteristic for the stacking of monolayers with octahedral coordination, while the 2H and the 3R stacking are specific for the trigonal-prismatic arrangement of atoms within monolayers (see Figs. 2.2**D-E**). As it can be seen from the Figs. 2.2**C-E**, the number in the polytype's name stands for the number of layers in a unit cell, whereas the letter represents the stacking symmetry. For instance, in the 1T form, the monolayers with the trigonal-prismatic (**T**) arrangement of atoms are directly positioned above

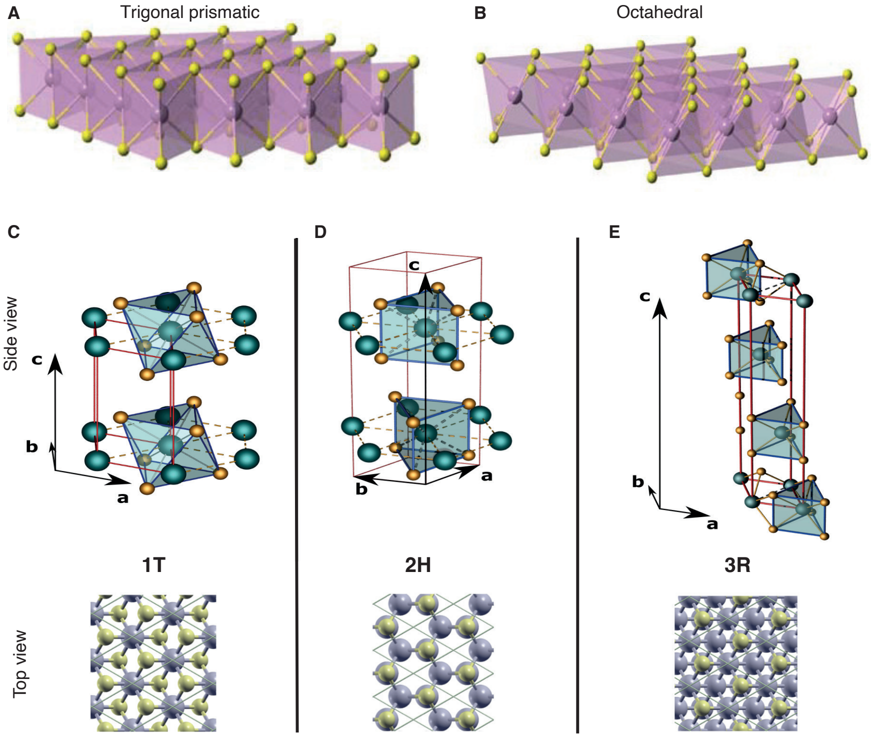

Figure 2.2: Crystal structure of the TMDs. Within monolayers, atoms are arranged either in **A** trigonal-prismatic, or **B** in the octahedral coordinations. In the multilayer form, the individual monolayers can be stacked in 3 different ways (polytypes): **C** 1T, **D** 2H, **E** 3R. Adapted from Ref. [12].

the neighboring layers with **1** layer per unit cell. The 1T stacking is typical for metalic/semimetalic TMDs. However, the 4 TMDs studied in this thesis are semiconductors in the 2H form and their monolyers have a hexagonal crystalline lattice as shown in the bottom panel of Fig. 2.2**D**. That is why, we only consider the 2H polytypes in the following discussions.

The structure of the lattice defines the reciprocal lattice, whose Wigner-Seitz primitive cell –often referred to as Brillouin Zone (BZ)– plays a key role to understand various aspects of the band structure. For the semiconducting 2D TMDs, the BZ is hexagonal as shown in Fig. 2.3. When describing the electronic structure, local band extrema are often referred to as valleys. For the semiconducting TMDs, the most relevant valleys are located at high symmetry points –Γ (center of the BZ), K (corners of the BZ), M (middle points between two neighboring K-points). Also, a prominent place have

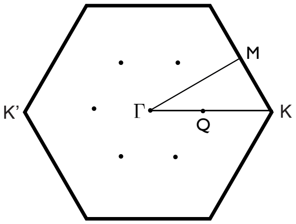

Figure 2.3: The Brillouin Zone of a hexagonal lattice. Γ, K(K'), M-points belong to the family of high symmetry points, while Q-points do not. The Γ-Q-K-M-Γ path (thin line) is often used in band structure calculations.

middle points between Γ and K-points –so-called Q-points– that do not belong to the high symmetry points.

2.2 Band structure of semiconducting TMDs

To understand key features of different optoelectronic phenomena studied in this thesis arising from the peculiar band structure of TMDs, we first discuss the case of monolayers. In monolayer form, TMDs are direct band gap semiconductors with conduction band minima and valence band maxima located at the K-points [12, 15, 48, 49], at the edges of the BZ (see Fig. 2.4). Also, there is a local maximum in the valence band located at the Γ-points, while a local minimum in the conduction band is at the Q-points. Irrespective of the choice for metal and chalcogen atoms, the monolayers of different TMDs have very similar band structure with material-specific band offsets and band gaps.

Without loss of generality, we discuss the band structure of 1L MoS_2 as an example. The valence and conduction bands result from hybridized $d_{x^2-y^2}$, d_{xy}, d_{z^2} orbitals of the metal atom and p_x, p_y, p_z orbitals of the chalcogen atoms [49–51]. Contribution of different orbitals to the band structure is shown in Fig. 2.4 (here we completely ignore the spin of electrons). Interestingly, even though the conduction and the band maxima are located at the same K-points of the BZ, we can see from the figure that the orbital contribution to the bands is different. For instance, the conduction band is mainly composed of $d_{x^2-y^2}$, d_{xy} of the Mo-orbitals, hybridized to the p_x, p_y orbitals of the S-atoms at the Q-points, and the d_{z^2} of Mo at K-points. On the other hand, the valence band has main contribution of the d_{z^2} of Mo at the Γ-point and the $d_{x^2-y^2}/d_{xy}$ orbitals at the K-points. Apart from the direct band gap at the K-points, there are several indirect band gaps due to the local conduction band minima at the Q-points, and the local valence band maximum at the Γ-point that plays a crucial role in the band

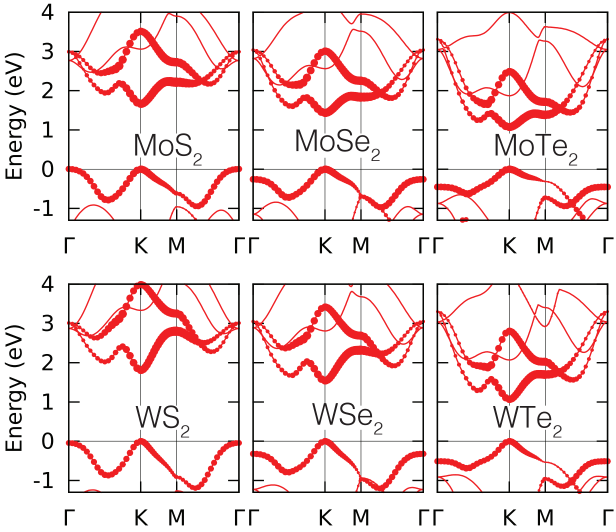

Figure 2.4: Density-functional theory calculations of the band structure (spin degenerate for the simplicity) of monolayer semiconducting TMDs. In all the cases, the band structure is very similar and the band gap is always direct. The valence band maximum and the conduction minimum are located at the K-points of the BZ. The band gap and the band offsets between different points of the BZ are material-specific. Adapted from Ref. [50].

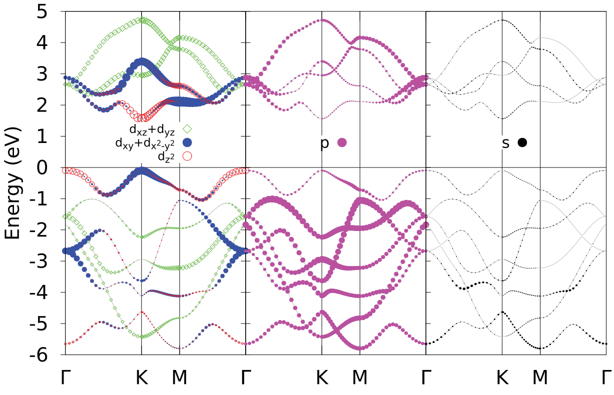

Figure 2.5: The contribution of different orbitals to the band structure of the 1L MoS$_2$. The size of the markers corresponds to the weight of the corresponding orbital in the band. The colour decodes the Mo $d_{x^2-y^2} + d_{xy}$ (filled blue circles), $d_{xz} + d_{yz}$ (empty green rhombuses), and d_{z^2} (empty red circles), and the S_p (filled purple circles), s (filled dark circles) orbitals. Adapted from Ref. [50].

structure of thicker layers.

So far, the electron spin has been completely ignored in the analysis. However, when comparing energy distances between the band extrema at different points in the BZ, it is important to consider spin-orbit coupling (SOC) that lifts spin degeneracy of the bands. This can be easily seen from the band structure calculations for 1L MoS_2 [50] in Fig. 2.6**A**. A clear splitting is observed in the valence band at the K-points, and at the Q and K-points in the conduction band. The strength of SOC depends strongly on the weight of transition metal, and induces significant energy splitting in the valence band at the K-points: it is as high as 150 meV in MoS_2.

It is worth mentioning a less important aspect for this thesis, but very important for spintronics –spin-valley coupling in monolayer TMDs– that arises from the inversion symmetry breaking together with strong SOC. The valley-dependent optical selection rule also becomes spin-dependent [12]. Transitions between different states in the conduction and the valence bands are only allowed for the states with same orientation of the spin depicted in Fig. 2.6**B**. Interestingly, carriers with various combinations of valley and spin indices can be selectively excited by optical fields of different circular polarization and frequency. Such a spin-valley locking enables observation of new phenomena when light can control the transport properties and vice versa.

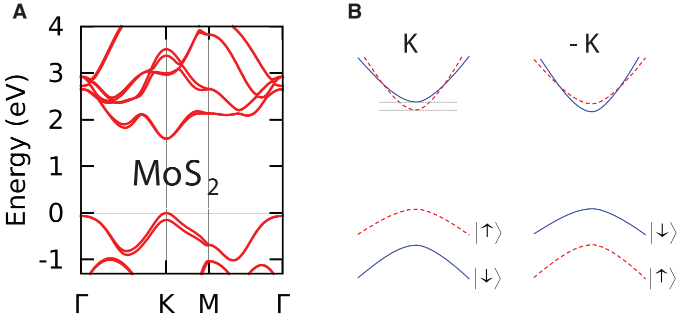

Figure 2.6: **A** Density-functional theory band structure calculations (spin included) of 1L 2H-MoS_2 crystal. Energy states at the K-points are spin-split. Panel **B** shows band edges in the vicinity of K-points. The colour red (blue) marks the spin-up (down) states. The energy states at K and -K points have opposite spin due to the time-reversal symmetry. Spin-valley locking in 1L TMDs allows exciting carriers with an on-demand combination of valley and spin degrees of freedom by the light of appropriate energy and helicity. Adapted from Ref. [50].

2.3 Thickness-dependence of the band structure of semiconducting TMDs

Having analysed the band structure of monolayers, we move to the aspects of the electronic structure of thicker TMD layers that are at the core of this thesis. In particular, the evolution of the band structure with the thickness of 2D semiconducting TMDs shows a few peculiarities that can be observed from the first principle calculations [12, 15, 46–49] shown in Fig. 2.7. First, the band-gap changes dramatically from 1L to bulk by about 1 eV. Second, the band extrema change their positions from K to Γ in the valence band, and from K to Q in the conduction band. As a consequence, the bandgap changes from a direct one in the case of 1L to indirect bandgap when the thickness is increased. These changes in the band structure can be understood in the context of interlayer coupling that depends on the overlap of the orbitals between neighbouring layers.

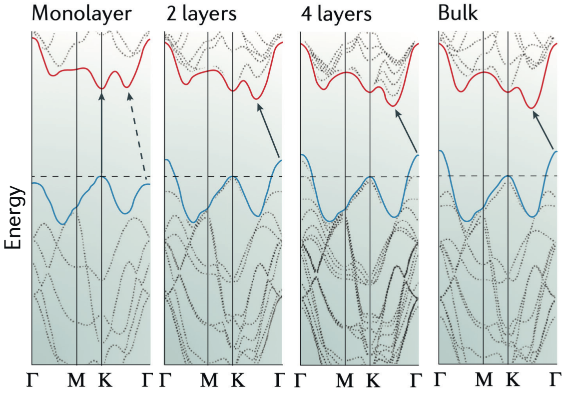

Figure 2.7: Calculated band structure of a monolayer, a bilayer, a quadrilayer, and bulk MoS_2 crystals along a high symmetry path in the Brillouine zone. The calculations demonstrate the transition from a direct (in monolayer) to an indirect (in thicker layers) bandgap semiconductor. Also, they show that the bandgap is tunable with the layer thickness. Adapted from Ref. [49].

To understand key features of how interlayer coupling affects the band structure when thickness is increased from 1L, we need to analyse the orbital contribution to the bands in details. As the simplest case we investigate the case of 2L MoS_2, whose band structure is shown in Fig. 2.8. The orbital contribution to the valence and the conduction bands at different valleys is different, and as a result, the interlayer coupling is valley dependent [51]. In particular, at the K-points, conduction band mostly composed of metal

d_{z^2} orbitals and the valence band is composed of $d_{x^2-y^2}/d_{xy}$ that are not sensitive to the thickness change due to their in-plane nature (there is almost no interlayer overlap between these orbitals). However, at the Γ-point in the valence band and Q-points in the conduction band, there is a significant contribution of the chalcogen p_z out-of-plane orbitals that are sensitive to the interlayer coupling because of their significant spacial overlap. Therefore, the strength of the interlayer coupling is large at the Γ-point in the valence band and Q-points in the conduction band and negligible at the K-points as calculations show in Fig. 2.8**B**.

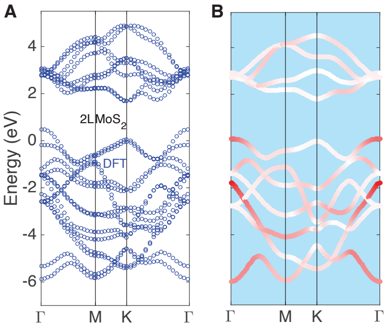

Figure 2.8: **A** Density-functional theory calculations of the 2L MoS_2 band structure. The valence band maximum is at the Gamma point and its energy position is well above the local maximum at the K-point. This indicates a significant interlayer coupling for the states in the valence band in the vicinity of the Brillouin zone center. **B** Interlayer coupling strength (shown with colour) along a high symmetry path in the BZ. The interlayer coupling is strong (red colour) at the Gamma point and almost absent (white colour) at the K-points due to the different nature of orbitals at these points in the BZ. At the Gamma point, valence band states are composed of out-of-plane orbitals that have a significant overlap in real space. That is why the interlayer coupling strength is large in the vicinity of the Gamma point. Adapted from Ref. [51].

To develop our analysis further, we now move to the qualitative description of the bandgap reduction when increasing number of layers in a TMD crystal. As we have discussed, the out-of-plane electronic coupling between the layers is significant at the Γ-point and the Q-points for the valence and the conduction bands correspondingly. The sensitivity of the band gap to the thickness of layers can be described in terms of the well-known "particle in a box" model. In this model, the energy of the charge carriers is inversely proportional to the square of the thickness of the barrier L ($E_n = n^2h^2/8mL^2$). Therefore, when the thickness of TMD layers is increased, the energy gap between the bands in the Q and the Γ valleys is decreased. Such bandgap tunability with number of layers and the indirect-to-direct band gap crossover are remarkable properties that make TMDs attractive for optoelectronics.

2.4 Controlling the band structure of TMDs with a perpendicular electric field

Apart from the tunability of the band structure by varying thickness of the 2D TMD layers, the band structure can be altered with an external electric field [52, 53]. The first demonstration of this effect was achieved in a bilayer graphene (zero band gap semiconductor) devices [14, 54, 55], where an external perpendicular field opened a band gap of a hundred meV. Even though the band structure could be first modified moderately with an electric field in a 2D material such as a bilayer graphene, the control of the band structure in other 2D materials [56–63] on a large energy scale has been elusive because of the magnitude of the accessible electric fields. Here we focus on the control of the band structure of TMDs on the electron-volt scale through the application of a large perpendicular electric field.

To understand qualitatively the modification of the band structure in a perpendicular electric field, we consider a bilayer system with no interlayer coupling. The logic described here can be expanded for thicker layers as well. When an external perpendicular field is applied to the system, it creates a potential difference between the two layers and shifts the bands of the layers as a whole towards each other. Now, if the created in this way voltage difference between the layers is larger than the band gap divided by the elemental charge, the valence and the conduction band overlap and the system becomes gapless. Even though such a model is very rough, the described scenario is very realistic in the vicinity of the K-points of TMDs, where the interlayer coupling is almost absent.

A more accurate picture of the effect of the perpendicular electric field on the band structure of TMDs [52], however, can be drawn by ab initio calculations that we show in Fig. 2.9 for MoS_2, $MoSe_2$, and WS_2. The calculations show that the band gap of these 2L TMDs continuously decreases with an increasing vertical field and eventually closes at an extremely large critical field ≈ 2 V/nm. The lowest conduction band and the highest valence band shift linearly with altered electric field, that goes along with the qualitative model we have discussed. Among common semiconducting TMDs, WSe_2 has the lowest critical field (top panel of Fig. 2.10) that is linked to its smaller band gap compared to the other TMDs. The value of critical field for a 2L WSe_2 [53] stimulated the choice of the material for the investigation of the effect of a perpendicular electric field on the band structure of TMDs discussed in **Chapter 7** of this thesis.

More interestingly, stepping away from bilayer WSe_2 to thicker layers,

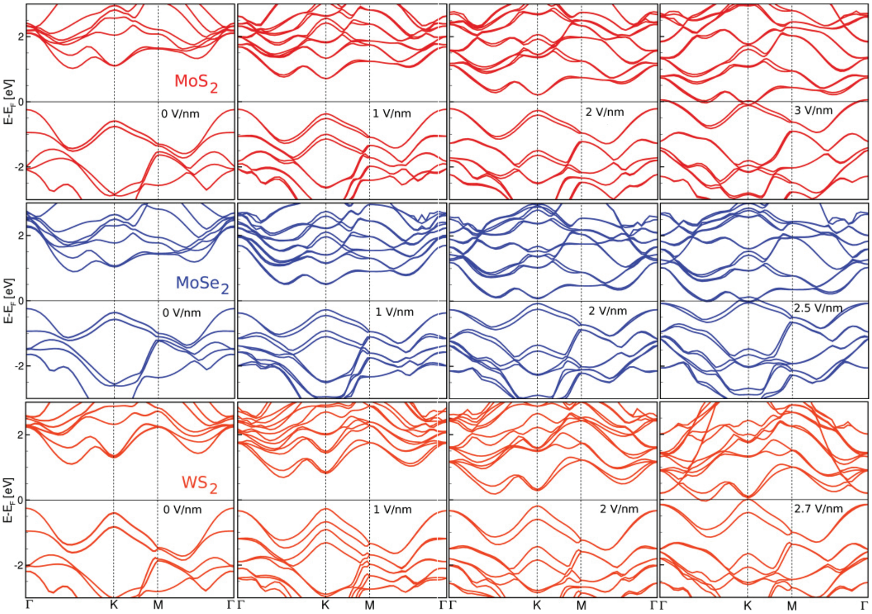

Figure 2.9: Density-functional theory calculations of the band structure of 2L MoS_2 (top row), 2L $MoSe_2$ (middle row), and WS_2 (bottom row) at different external perpendicular electric fields. The electric field increases from left (0 V/nm) to right. The band gap reduces when the electric field field is increased and completely closes at a certain critical field. These calculations also show that the critical field is lower in the materials with the smaller band gap. Adapted from Ref. [52].

the band gap reduces more rapidly with increasing electric field as demonstrated in Fig. 2.10 for 2L, 3L, and 4L crystals. Such a sensitivity of the tunability of band gap in a perpendicular electric field to the thickness of WSe_2 gives additional degree of freedom to control the band structure. From these calculations, we clearly see that the critical field decreases monotonically when the thickness of layers is increased, and already for a 4L WSe_2 it is $\approx 1/3$ of the critical field for a 2L WSe_2. A new type of gating technique discovered by us can realize such large electric fields as we discuss in great detail in **Chapter 3** with corresponding results presented in **Chapter 7**.

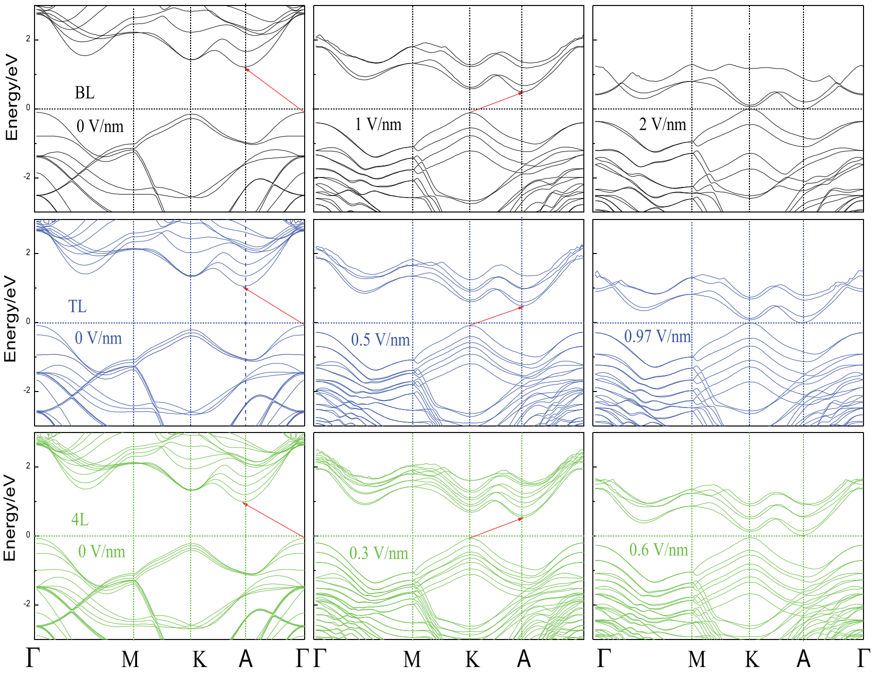

Figure 2.10: Density-functional theory calculations of the band structure of WSe_2 crystal of different thicknesses at different electric fields. The top three panels correspond to the band structure of a bilayer WSe_2 at zero electric field (left), at an intermediate electric field (middle), and at the critical electric field (right) where the band gap is closed. The thickness of WSe_2 changes by 1L from 2L on the top row to 3L on the bottom row. The critical field decreases with the thickness due to the larger induced electric dipole in thick layers as compared to the thin ones as can be interpreted in the manner of the Stark effect. Adapted from Ref. [53].

2.5 Structural and electronic properties of InSe

Transition metal monochalcogenides, among which is Indium Selenide, have recently attracted interest due to their unique properties and possible applications in solar energy, optoelectronics, and fundamental science [64]. Similar to the semiconducting TMDs, InSe is a layered material with strong in-plane bonds and van der Waals bonds between the layers. The crystal structure of InSe consists of Se-In-In-Se layers. Within each plane, atoms form hexagons (Fig. 2.11**A**) with lattice parameter a = 4.002 A [65, 66]. Within a multilayer crystal, individual monolayers are stacked such that chalcogen atoms of the top layer are directly above the metal atoms in the layer below. Chalcogen atoms of the bottom layer are not directly below the metal atoms in the layer above, similar to the ABC stacking of graphene as shown in Fig. 2.11**B**. Since InSe has an hexagonal lattice, the BZ is hexagonal with the same notion applied to the high symmetry points as we have discussed previously in **2.1**.

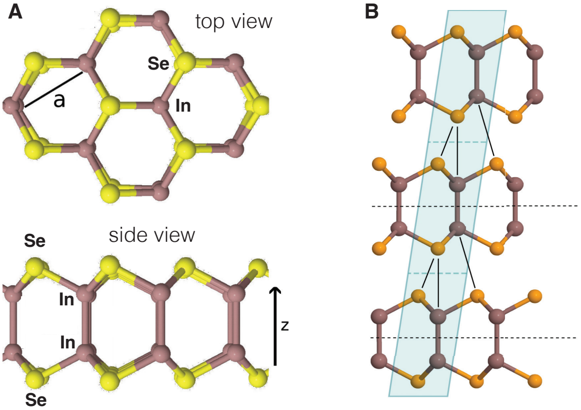

Figure 2.11: Structural composition of InSe crystals. **A** The top and the side view of the crystal with the lattice parameter a. In a monolayer form, chalchogen atoms (yellow balls) and transition metal atoms (brown balls) form a honeycomb-like lattice similarly to TMDs and graphene. In its multilayer form, the n-type InSe (γ-InSe) crystal has rhombohedral symmetry: individual monolayers follow the graphene's ABC-like stacking order. Adapted from Ref. [65, 66].

In the bulk form, InSe is a direct band gap semiconductor. Unlike TMDs, the band structure of InSe undergoes the transition to an indirect band gap semiconductor [67, 68] when thinning down to the monolayer limit. For thicknesses 1L-6L, the valence band maximum shifts from the Gamma point –where it is located in thicker layers– and has an unusual shape of inverted sombrero-like dispersion [66–68]. The conduction-band minimum stays at Gamma regardless of thickness –a property that we exploit in **Chapter 5** to demonstrate a new versatile platform for radiative interlayer transitions in van der Walls heterostructures (see also following sections). These peculiarities of the electronic structure can be seen from Density-Functional Theory (DFT) calculations [66] depicted in Fig. 2.12**A-E** for 1L to 5L InSe crystals. The calculations show that the band gap is highly-tunable with the thickness (Fig. 2.12**F**). Interestingly, the bang gap changes almost by 2 eV when stepping from bulk to monolayer crystals [69]. This sensitivity can be explained in the spirit of the spacial confinement effect as we have previously discussed. Other peculiarities include the relatively light effective mass of the electrons in conduction band that can be exploited in high mobility transistors [69]. Also, valence band has almost a flat edge, a property that may give the opportunity to explore strong correlations in hole-doped crystal.

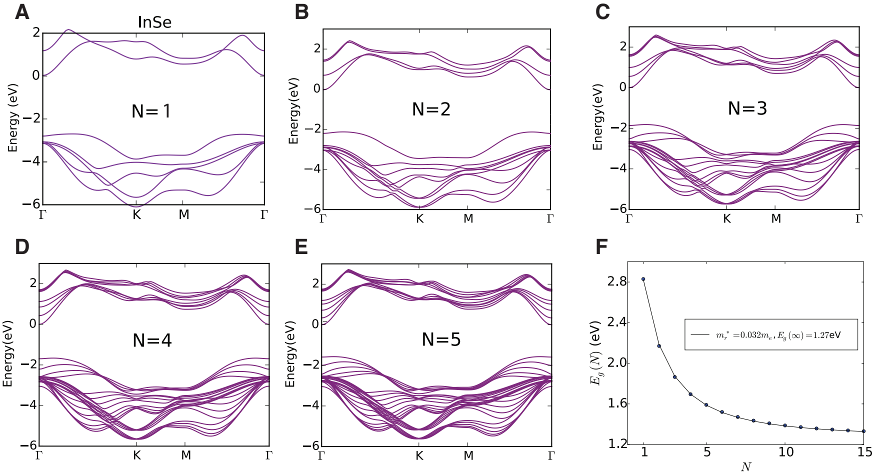

Figure 2.12: First principles band structure calculations for InSe crystals. Panels **A**-**E** show the band structure of 1L to 5L crystals consequently. The conduction band minimum is located at the Gamma-point, while the valence band shows a Mexican hat-like dispersion. **F** Evolution of the band gap for different layer thicknesses up to 15L. Adapted from Ref. [66].

2.6 Excitons in 2D TMDs and InSe

Light-matter interaction is responsible for optical properties such as absorption, reflection, transmission, emission, and light scattering [7, 12]. Upon illuminating a semiconductor with the light of energy larger than the band gap, an electron in the valence band is excited to a state in the conduction band. This creates a vacant place in the valence band known as a hole. The electrons and holes interact via a Coulomb-like interaction, which is greatly enhanced in 2D due to a weak dielectric screening compared to 3D. This leads to the formation of strongly bound electron-hole pairs, excitons. They are free to move through the crystal (Fig. 2.13**A**), and dominate the optical and optoelectronic response of materials [12–14, 26].

To describe their motion, excitons can be viewed as an analogy of hydrogen atom [26]. The difference of the description between them is mainly quantitative. First, the proton and electron masses are very different in the hydrogen atom, unlike in excitons with similar masses of holes and electrons. Second, the dielectric constant of 2D semiconductors ($\epsilon = 7$ for TMDs) is different from the one of hydrogen atom ($\epsilon \approx 1$). Using the mentioned analogy, the motion of excitons decomposes into two components: motion of the center-of-mass of the exciton, and relative motion of the hole and electron. Then, the exciton dispersion relation $E_{exc}(n, Q_{exc})$ can be written as a sum of three components: the gap of the semiconductor (E_g), the Rydberg series (depends on the principal quantum n), and the kinetic energy of the center-of-mass with the momentum $\hbar Q_{exc}$. The quantized Rydberg series are defined as $13.6\ eV \frac{\mu}{m_0 \epsilon^2 (n-1/2)^2}$, where μ is the reduced exciton mass and m_0 stands for the free electron mass. In other words, the exciton dispersion reads:

$$E_{exc}(n, Q_{exciton}) = E_g - 13.6 eV \frac{\mu}{m_0 \epsilon^2 (n-1/2)^2} + \frac{(\hbar Q_{exc})^2}{2M} \tag{2.1}$$

where $n = 1, 2, 3, \ldots$, and M is the total mass as shown in Fig. 2.13**B**. The excitonic resonance lies at lower energy than a non-interacting electron-hole pair by the amount equal to the binding energy E_B of the exciton described by the 1S-state (n=1) in the Rydberg series. In 2D, the binding energy of excitons reaches the scale of 1 eV. This originates from their small radius and low screening effects as compared to conventional 3D III-V semiconductors, and an additional factor of 4 (n=0 in Eq. 2.1) arising from the 2D nature of excitons. That is why there is a sizeable difference between the free particle band gap and the optical band gap.

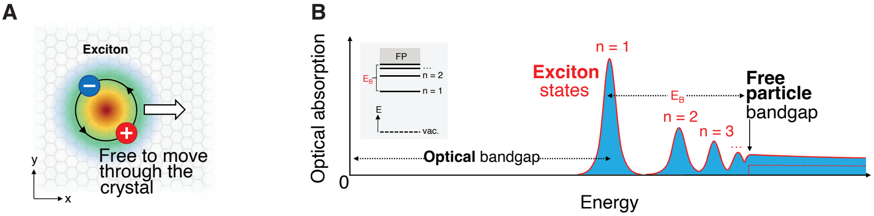

Figure 2.13: Excitons in 2 dimensions. **A** An electron and a hole coupled together via Culomb-like interaction forming an exciton that is free to move through the 2D crystal. **B** Energy dispersion of an exciton. The electronic band gap corresponds to the free particle band gap (with non-interacting electrons and holes), while the optical band gaps differs from it by the exciton binding energy defined by the exciton's 1S (n=1) state. Adapted from Ref. [26].

Besides excitons in intrinsic semiconductors, some additional resonances can appear in the optical spectra of doped semiconductors [12, 26]. An exciton can acquire an extra electron or a hole in these doped semiconductors, forming a three-particle state - a trion. The added electron/hole to the neutral excitons results in a new elementary excitation state of the crystal with a different energy resonance as compared to that of the neutral excitonic peak. Even though the binding energy of trions can be as large as 20-40 meV and they could be observed even at the room temperature, the trions are not discussed in depth in this thesis because our work focuses on intrinsic semiconductors.

Once formed, excitons can recombine in two ways: either emitting light (**bright excitons**), or through a non-radiative path (**dark excitons**) with no light emitted as we sketch in Fig. 2.14. To be radiative, first, transition has to meet optical selection rules. Second, the momentum of the emitted photon has to match the momentum of the exciton (within the light cone). In direct-band semiconductors, the photon momentum is small, so the radiative recombination happens for the $Q \approx 0$. In indirect-band semiconductors, excitons can recombine radiatively if the momentum conservation is satisfied by involving phonons.

As compared to bright excitons, the dark excitons, in turn, are present in a few forms. For example, if the optical selection rules are not met for a transition between two states with the same momentum, we deal with a spin-forbidden dark excitons. From the other hand, even if the optical selections rules hold true for a transition, but the separation of the electron and the hole is very large in the momentum space, we face a momentum-forbidden dark exciton.

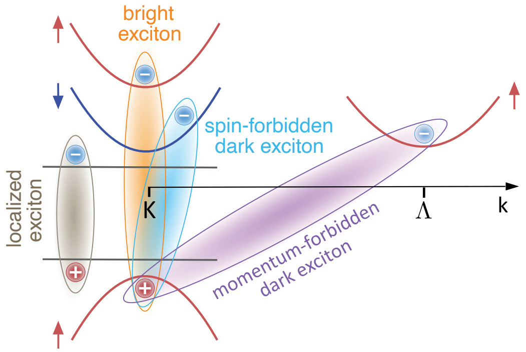

Figure 2.14: An excitonic zoo. The sketch shows a few band edges at different points in the Brillouin zone for a 1L TMD. The blue (red) colour of the bands corresponds to the spin down (up) orientation of the electron (hole) spins. Due to the optical selection rules, only the transitions between the states with the same orientation of the spins at the K-point are allowed (Bright Excitons). The transition between different orientations of the spin corresponds to the spin-forbidden dark excitons with no light emitted. Moreover, even if the hole and the electron are in the same spin states but largely separated in the k-space, these non-radiative transitions correspond to momentum-forbidden dark excitons. We also show excitons originating from localized states in the valence and conduction bands for a complete picture. Adapted from Ref. [26].

TMDs display a fascinating thickness-dependence of photoluminescence (light emission after absorption of photons, PL) signal. As we have discussed in *Section 2.2* and *Section 2.3*, the band gap of TMDs changes from an indirect gap in thick crystals to a direct gap in the 1L. This indirect-to-direct band gap transition has a strong effect on the PL signal of TMD crystals. When probing monolayers, the PL signal shows a sharp exciton peak from the lowest energy K-K transition, which is direct in the momentum space (A exciton) as we show in Fig. 2.15**A** for WS_2. PL from bilayers and thicker layers exhibits clearly a weaker signal as compared to monolayers. Also, there is an additional low energy peak attributed to the indirect Q-Γ transition. The PL peak originating from Q-Γ transition shifts towards lower energies as conduction and valence bands move towards each other due to quantum confinement effect, when layer thickness is increased. That is why the energy position of the PL peak from the indirect exciton can be used to identify the thickness of 2D layers as we later discuss in **Chapter 4**.

As compared to TMDs, the PL of InSe exhibits even stronger sensitivity to the thickness due to a more pronounced quantum confinement effect associated with a light effective mass for electrons in the conduction band [69]. From bulk to monolayer, the PL signal from the A-exciton shifts by almost 2 eV offering a great spectral tunability as depicted in

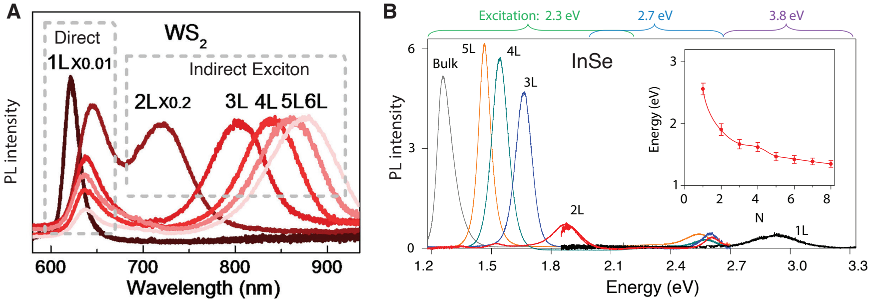

Figure 2.15: Photoluminescene spectra of **A** WS_2 and **B** InSe crystals. In WS_2 (a representative material from the TMD family) PL spectra show a dramatic increase of the intensity of signal from a monolayer as compared to thicker layers. Additionally, the position of the peak originating from the indirect exciton shifts significantly when the layer thickness is increased (due to the quantum confinement effect). For this reason, the thickness of a multilayer TMDs can be identified from their PL spectra. **B** PL spectra of 1L-5L InSe crystals. The PL intensity drops by an order of magnitude when reaching the 2L limit and down to 1L. This indicates the direct-to-indirect band gap transition (opposite to what happens in TMD crystals). The inset shows evolution of InSe band gap with thickness. In both panels, the spectra were taken at room temperature. Adapted from Ref. [69, 70].

Fig. 2.15**B**. Unlike in TMDs, the intensity of the PL signal in a few-layer InSe decreases more than 10 times (as expected from the direct-to-indirect band semiconductor transition) as thickness approaches the bi- and mono-layer limit. Although the band inversion in the valence band of InSe persists up to the 6 layers, it already becomes insignificant for trilayers. The reason for that is the comparability of the band inversion with thermal energy at room temperature (roughly 25 meV). That is why the A-exciton transition in InSe can be considered as quasi-direct in relatively thin layers and eventually becomes direct for the layers thicker than a hepta-layer.

2.7 Van der Waals heterostructures

Heterostructures (HTs) of semiconductors are the cornerstone of semiconductor physics and applications, as they are utilized in various devices. Their outstanding performance is quite crucial for the fields such as astronomy, satellite and mobile telecommunication, and many more. For instance, semiconducting HTs based on GaN and GaAs have been widely used in high-frequency and high-power devices such as microwave amplifiers due to their high electron mobility. Combining different materials together in heterostructures also allows controlling the band gap of such systems. This approach for band gap tuning is beneficial when engineering heterojunctions for efficient light absorption in multi-junction solar cells, cascade lasers, and effective light-emitting diodes.

Even though the progress has been immense in the field, there are not so many materials that can be combined to form heterostructures. The main issue is that the lattice parameters of HT constituents should match or be very similar. This lattice-matching is an essential requirement for the growth of one material on top of the other and a good quality heterojunction interface. In contrast, lattice mismatch in HTs leads to many defects at the interface (if HT constituents will grow on top of each other at all), which is impractical for most device applications. In contrast, van der Waals (vdW) materials offer a new platform to form heterostructures since there is no limitation on lattice and symmetry compatibility [28, 29]. Besides, a rotational degree of freedom is available for constituent materials in vdW heterostructures. It has given rise to a new field called Twistronics, and remarkable phenomena recently emerged [42]. Such versatility of vdW HTs makes them a desirable platform for discovering new physics.

The optoelectronic properties of heterostructures strongly depend on the relative band alignment of constituent semiconductors. For simplicity, we consider three types of possible band alignment between only two semiconductors that we call "A" and "B", whose valence and conduction bands are represented with different colours as illustrated in Figs. 2.16**A-C**.

In the first type of alignment (Fig. 2.16**A**), the conduction and the valence bands of "A" are completely inside the band gap of the "B". The energy difference between conduction (valence) bands of "A" and "B" –band offset- creates a potential barrier for electrons (holes) which confines them in "A". This type of heterostructures with III-V semiconductors has been exploited in lasers and vastly impacted the technological progress. For the invention of these structures that laid the foundation for the modern era of computers and information technology, Zhores Alferov together with

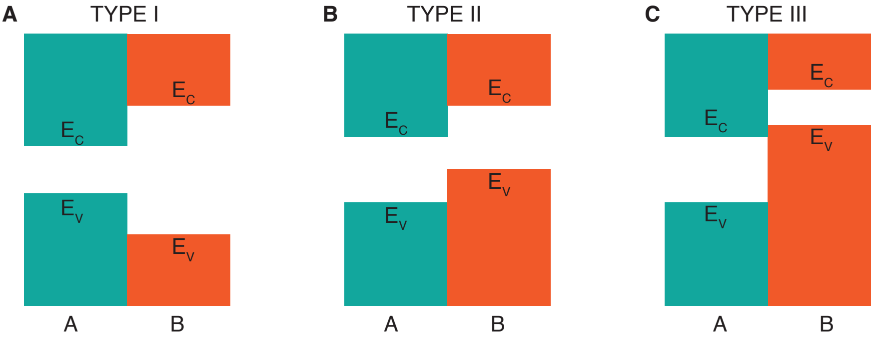

Figure 2.16: **A** Type I, **B** Type II, and **C** Type III band alignment of semiconductors in a heterostructure.

Herbert Kroemer and Jack S. Kilby recieved Nobel Prize in physics in 2000. Relating to the 2D semiconductors, such type of the band alignment can significantly improve light absorption and emission in the smaller band gap material, as it has been shown for $WSe_2/MoTe_2$ [71], and MoS_2/ReS_2 [72] heterostructures.

In the second type of alignment, both the conduction and the valence bands of "A" are located lower in energy than the bands of "B" as shown in Fig. 2.16**B**. Holes are confined in "B", while electrons are in "A". The effective band gap of such a heterostructure is defined by the offset of the "A" conduction band and the "B" valence band. This type of alignment opens the door to engineer the band gap of heterointerfaces by choosing appropriate materials. We extensively exploit this in **Chapter 5** where we demonstrate van der Waals heterostructures of various TMDs with InSe.

In the type III band alignment, the conduction band of the semiconductor "A" overlaps with the valence band of the semiconductor "B". The peculiarity of this system is that it has no band gap and the states for electrons and holes are available in the whole energy range. Effectively, the heterostructures of this type behave like semimetals [36].

2.8 Interlayer excitons in van der Waals heterostructures

Having introduced basic notions of excitons and vdW HTs, we now extend our discussion to new excitonic species that we have not discussed previously. In this section we will only consider type II heterostructures made of two semiconductors "A" and "B". When such a heterostructure is exposed to light with the energy greater than the band gaps of "A" and "B", a few excitonic resonances are formed. The first one, an intralayer exciton, is formed from electron and hole that are located within the individual layers of the HT (Fig. 2.17**A**) with their properties discussed in *Section 2.6*. However, electrons in semiconductor "A" also interact with holes from semiconductor "B" via a Coulomb-like potential. This leads to the formation of bound electron-hole pairs known as interlayer excitons [26, 27] as illustrated in Figs. 2.17**A** and **B**. Unlike intralayer counterparts, the interlayer excitons have their dipole moment oriented out-of-plane of the heterostructure (dark arrow in Fig. 2.17**A**) due to the spacial separation of electrons and holes. The difference in the orientation of the dipole moment of excitons plays a significant role when studying excitonic interactions. Also, it can be used to probe the intra/interlayer nature of excitons in a material or a heterostructure.

The spacial separation of holes and electrons in interlayer excitons leads to the control of exciton's radius a. Altering exciton radius allows tuning of exciton-exciton interactions in the system. This can be done either by changing the thickness of the constituents of an heterostructure, or by introducing an insulating spacer such as h-BN between the semiconductors. By moving electrons and holes apart from each other, the exciton life time is enhanced $\sim a^2$. As compared to intralayer excitons with a relatively short life time of a few tens of ps, the life time of interlayer excitons is significantly larger reaching the μs range. Such advantage of interlayer excitons over intralayer excitons in terms of the life time plays a crucial role for excitonic devices. The large lifetime of interlayer excitons allows traveling excitons over significant distances before they recombine, giving an opportunity to use them as information units. Moreover, the out-of-plane dipole moment can be exploited to control excitons by application of external electric field to make novel devices as well as widely tunable light sources.

However, to harvest the benefits of using interlayer excitons in optoelectronic devices, these excitons should recombine radiatively. For this reason, the interlayer transitions should meet the optical selection rules and the kinematic momentum of the exciton has to be within the light cone

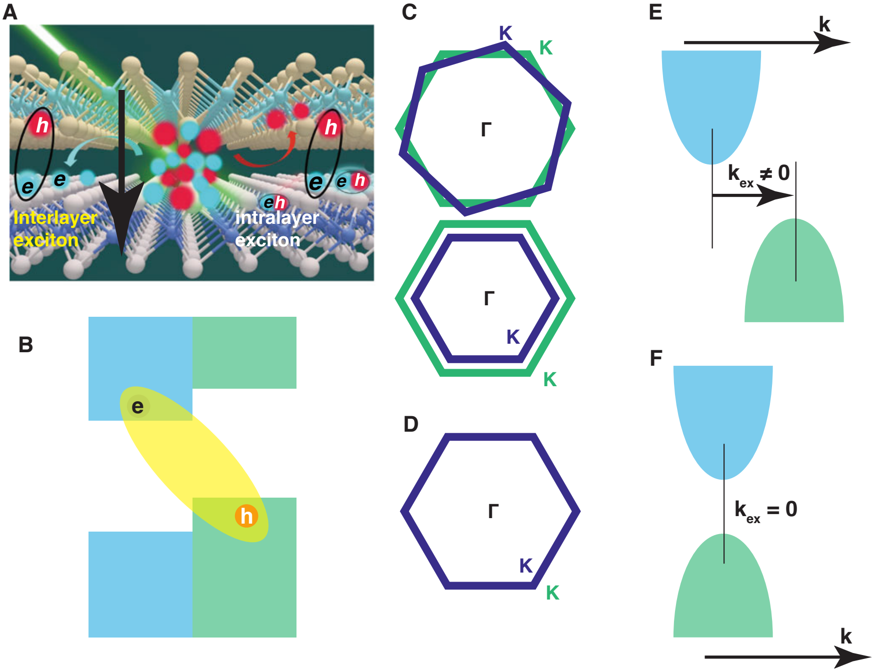

Figure 2.17: **A** Cartoon of spacial distribution of different excitons in a layered structure. In interlayer excitons, electrons and holes reside in different layers creating an out-of-plane dipole moment indicated with a dark arrow. **B** Interlayer exciton in a Type II heterostructure. **C** Alignment of Brillouin zones of two different monolayer TMDs (shown in green and blue): (top) the TMDs have same lattice parameters but they are rotationally misaligned; (bottom) two rotationally aligned monolayers that have different lattice parameters. In all these cases, the conduction and the valence band edges are misaligned in momentum space (**C**) and the interlayer excitons gain a finite kinetic momentum $\mathbf{k}_{ex}$. However, when both lattices of the semiconductors match and they are rotationally aligned (D), the conduction and the valence band edges match in the k-space and $\mathbf{k}_{ex} = \mathbf{0}$ as in the case of aligned $MoSe_2/WSe_2$ heterostructures. Adapted from Ref. [26].

as we have discussed in **Section 2.6**. For an efficient light emission, the interlayer transitions must be also direct in the momentum space. In type II heterostructures, this implies that the conduction and the valence band edges should have the same momentum coordinates for the semiconductors "A" and "B". This requirement is met if the Brillouin zones of the two semiconductors have the same size (same lattice parameter) and the same orientation/symmetry. For clarity, we illustrate this concept with HTs made of two TMD monolayers in Fig. 2.17**D** and Fig. 2.17**F**. In general, finding materials with the similar lattice parameters and the same symmetry is difficult. Even within the same family of materials such as TMDs, the lattice parameters of the materials are different. Therefore, the size of the BZ is different (bottom sketch in Fig. 2.17**C**), which leads to the indirect in the k-space transitions as shown in Fig. 2.17**E**. Even if the perfect match is found –such as monolayers of $MoSe_2/WSe_2$, the CBM and VBM can be easily mismatched due to the rotational misalignment as depicted in the top sketch of Fig. 2.17**C**. Thus, achieving direct interlayer excitonic transitions is a rather challenging task in general, and the number of the perfect matches is also extremely limited.

A radical solution to radiative transitions in van der Waals heterostructures is to use semiconducting materials that have CBM and VBM at the Gamma point – center of the Brillouin zone. In such a case, the interlayer transitions will be always direct in the momentum space irrespective of material lattice parameters and the relative orientation of the two semiconductors in a heterostructure. Possible candidates to implement this approach are multilayer TMDs with the VBM at the Gamma point, while the materials with CBM at the Gamma point can be transition metal monochalcogenides such as InSe. A detailed discussion of this novel approach and its experimental realisation is presented in **Chapter 5**.

CHAPTER 3

Electrostatic gating

Electrostatic gating is a key technique to control electronic properties of a material by the application of an external voltage. The technique is based on the use of field-effect transistors, cornerstones of modern electronics. These transistors can be found almost in every electronic device that we use in our daily life: computers, cameras, IPads, smartphones, Apple Watches– are just a few examples. The density of the transistors in a device such as modern memory card goes beyond imagination. A 32 GB RAM memory card has approximately 256 billion transistors –a quantity comparable with the number of stars in our galaxy– and it weights just half a gram. Apart from its wide use in transistors, electrostatic gating is also a versatile technique. For instance, one can study the electronic properties of materials as a function of carrier density and the rich phenomena happening in them by using this technique. The transport studies performed in the thesis highly rely on this approach, therefore we give an insight into physics behind electrostatic gating when using different types of transistors.

3.1 Field-effect transistors

Transistors have different geometries and suit different purposes. Here, we discuss the transistors where modulation of the conduction is governed by an electric field. This is the most relevant aspect to cover here, which is needed for understanding device operation principles in transport studies

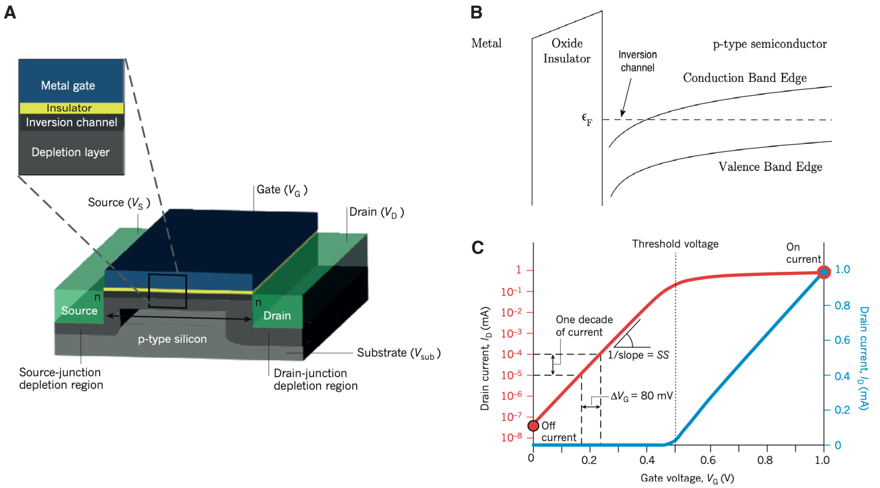

Figure 3.1: **A** A typical silicon MISFET. A p-doped silicon wafer that has two contacts –the n-doped Source/Drain regions – is covered with a thin layer of its native oxide covered with a metal gate. The charge at the gate/oxide and the oxide/silicon interfaces is governed by the gate voltage. When a positive voltage is applied to the drain (here the source contact and the substrate are grounded), there is no current flowing from the substrate to the source as in the reverse biased p-n junction. However, when a large positive gate bias is applied, it spills out electrons from the source and drain contacts forming an electron-rich layer – the transistor channel– letting the current flow between these two electrodes. **B** Energy band diagram for a MISFET under a finite positive gate bias. The conduction band crosses the Fermi level enabling current flow in the transistor channel. **C** The current in the transistor channel as a function of gate voltage (blue curve - linear scale, red curve - logarithmic scale). Once the gate voltage exceeds the threshold voltage, the transistor is in the "on" state. The switching into the "on" state is gradual due to the finite width of the band tail and the finite width of the Fermi-Dirac distribution for electrons at room temperature. Adapted from Ref. [73].

performed in the thesis. As a starting point, we first describe the operation principle of conventional field-effect transistors (FETs) – Metal-Insulator-Semiconductor (MIT) field-effect transistors, or shortly MISFETs [73]. The main component of MISFETs, the MIS stack, acts as a parallel plate capacitor where charge can be accumulated in a controlled fashion. In a typical MISFET depicted in Fig. 3.1 **A**, a metal electrode called the gate covers the insulator. Also, two electrodes –the source and the drain– are placed onto the semiconductor. In this capacitor-like geometry, the induced charge at different interfaces is controlled by the voltage applied to the gate. If there are mobile charges in the semiconductor, then a voltage difference between the source and the drain creates a current flow. The amount of the charges and, therefore, the current can be controlled by the gate electrode.

To understand the mechanism of the charge accumulation in field-effect transistors, we need to analyze the band diagram of the Metal-Insulator-Semiconductor stack. Since the position of the chemical potential is important in this system, we need to take it into account when describing the transport properties of the transistor. At zero gate voltage, the transistor is in its "off" state and there is no current flowing in the channel because the Fermi-level is inside the gap of the semiconductor. If the semiconductor is intrinsic, the chemical potential is in the middle of the gap. However, when the semiconductor is p-doped (n-doped), the chemical potential is closer to the valence (conduction) band. For instance, when a positive gate bias is applied, the conduction band of a p-type semiconductor bends towards the chemical potential. This happens due to the local increase of the charge density. As a result, the transistor switches into the "on" state once the conduction band crosses the chemical potential and a negative charge is accumulated at the Insulator-Semiconductor interface as it is shown in Fig. 3.1 **B**. The gate voltage needed to turn the transistor into the "on" state is referred as the threshold voltage V_{th}.

Nonetheless, there is no sharp transition from the "off" to the "on" states in MISFETs. The switching does not occur at a precise voltage applied to the gate, but instead it happens gradually over a range of gate voltages (Fig. 3.1 **C**). When the gate is biased below the threshold voltage, there will be still some current flowing in the channel because of the finite widths of the band tail and of the Fermi-Dirac distribution for electrons. Therefore, this sub-threshold regime defines the sharpness of the on/off transitions in transistors. To quantify the sharpness of on/off transitions, the so-called sub-threshold swing (S) –the value of the gate voltage V_G required to change the source-drain current I_{SD} by an order of magnitude– is often used:

$$S = \frac{dV_G}{d(\log(I_{SD}))} \tag{3.1}$$

At a finite temperature T, $S = \ln 10 \, \frac{k_B T}{e} \left(1 + \frac{C_Q}{C_G}\right)$ in a MISFET with a solid dielectric. C_Q and C_G denote the quantum capacitance of the charge accumulation layer and the gate capacitance correspondingly. Here, k_B and e are the well-known Boltzmann and elementary charge constants. The quality of transistors is directly linked to the sub-threshold swing, reaching its ultimate value of 59.6 mV per decade at room temperature ($T = 300$ K), when $C_Q/C_G \longrightarrow 0$.

3.2 Operation regimes of field-effect transistors

Apart from the gate voltage, the source-drain bias also plays a crucial role on how a transistor operates. This aspect is prominent in current-voltage characteristics –so-called output curves. In a typical measurement of output curves, the gate bias is fixed while the source-drain bias is being swept. Depending on the interplay between the gate and the source-drain voltage, FETs display different operational regimes: linear, pinch-off, and ambipolar injection.

To describe this interplay, we use the Ohm's law in the differential form as well as the gradual channel approximation when calculating the current flowing in the transistor channel. Then the current per unit area **j** of the transistor channel can be written as:

$$\mathbf{j} = ne\mu\,\mathbf{E} \tag{3.2}$$

where n is the charge density, and μ quantifies the mobility of the carriers driven by the electric field **E**. For the moment, we only consider the presence of just one type of charge carriers (i.e. electrons). Here the electric field is simply defined by the gradient of the potential of the transistor channel. If we consider the electric field being constant, this assumption leads us to the gradual channel approximation: the potential of the channel changes gradually from the source to the drain contact. In practice it works quite well, when the channel geometry is rectangular and the length of the channel is much longer than its width. Despite the fact that in real transistors the dependence of the potential is much more complex and defined by the Poisson equation, the gradual approximation for a long channel is sufficient enough to cover the basics aspects of the operation regimes of a transistor.

In the absence of gate voltage, the potential changes linearly from zero (at the source) to V_{SD} (at the drain) with no current flowing in the channel due to the absence of charge carriers. However, when a non-zero gate bias (V_G) is applied (a typical biasing configuration of a MISFET is shown in the Fig. 3.2 **A**), the effective potential across the channel ($V_G - V_{ch}(x)$) becomes gate-dependent as it is depicted in Fig. 3.2 **B**. Consequently, the density of charge carriers accumulated in the channel becomes spatially dependent, and determined by the local potential of the channel ($V_{ch}(x)$):

$$n = C_G(V_G - V_{ch}(x) - V_{th})/e \tag{3.3}$$

Substituting that into Eq. 3.2, in the rectangular geometry of the channel with width W and length L, we have:

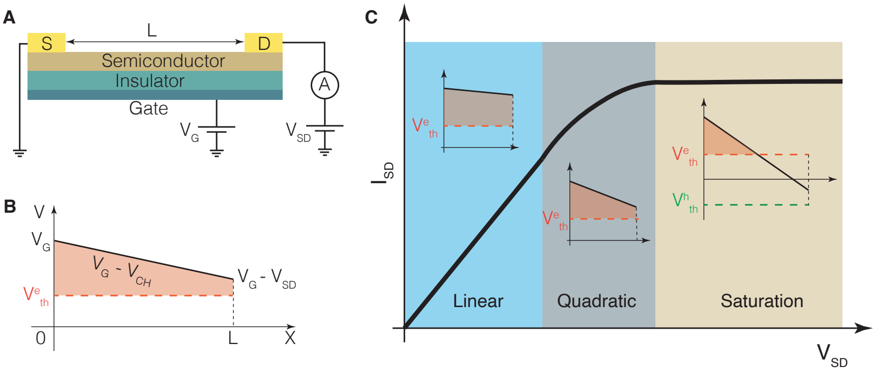

Figure 3.2: A Sketch of a MISFET under its typical biasing conditions. The two electrodes –the source (S) and the drain (D)– are placed onto the semiconductor. The gate bias V_G is kept constant during measurements of output characteristics. The source is grounded, while V_{SD} is applied to the drain electrode. The current I_{SD} in the channel (of a length L) is measured with an ampèremeter A. Under these biasing conditions, the effective potential of the channel (**B**) changes from V_G at the source electrode to V_G - V_{SD} at the drain electrode. When the V_{SD} is swept, the current shows different dependencies as a function of V_{SD} (**C**). At small V_{SD} compared to the V_G - V^e_{th}, the dependence is linear (the blue region with the effective potential pictured inside that region). Passing the intermediate region with the current changing quadratically, the current saturates at $V_G - V_{th} \leq V_{SD}$.

$$I_{SD} = W \mu C_G \left(V_G - V_{ch}(x) - V_{th}\right) \frac{dV_{ch}(x)}{dx} \tag{3.4}$$

Here, I_{SD} is a constant that does not depend on the coordinate along the channel. Solution of Eq. 3.4 (first-order differential equation) gives the exact form of the local potential of the channel:

$$V_{ch}(x) = V_G - V_{th} - \sqrt{(V_G - V_{th})^2 - \frac{2I_{SD}}{W \mu C_G} x} \tag{3.5}$$

Using the boundary condition $V_{ch}(x = L) = V_{SD}$, we can now solve Eq. 3.5 for I_{SD}:

$$I_{SD} = \frac{W}{L} \mu C_G \left([V_G - V_{th}] V_{SD} - \frac{V_{SD}^2}{2} \right) \tag{3.6}$$

Comparing the source-drain voltage to the difference of the gate and the threshold voltages in Eq. 3.6 indicates different possible operation regimes shown in Fig. 3.2 **C**. The overall dependence of the current as a function of gate voltage is quadratic. For small V_{SD} such as $V_G - V_{th} \gg V_{SD}$, the current varies linearly with the V_{SD} because $V_{SD} > V_{SD}^2$, and thus the

FET operates in the **linear regime**. The further increase of the V_{SD} brings to the point, where $V_G - V_{th} \leq V_{SD}$ and the transistor enters the **pinch-off/saturation** regime with the current being saturated at the level:

$$I_{SD} = \frac{W}{2L} \mu C_G \left(V_G - V_{th}\right)^2 \tag{3.7}$$

3.3 Ionic-gated field-effect transistors

Despite the simplicity of MISFETs operation, this type of transistors does not offer limitless possibilities to control electronic properties of semiconductors. One of the limitations is the low gate capacitance that poses constraints on the maximum charge density that can be achieved in a semiconductor. A naive solution to this problem –decreasing the thickness of the insulator, therefore increasing the capacitance of the MIS stack, or using high-k insulators– fails to increase the charge density due to a decrease of the breakdown voltage of the solid-state insulators [74, 75]. Therefore, there is a need for better techniques to accumulate large charge densities and higher electric fields.

A key to solve the problem with the relatively low charge densities and electric fields is the replacement of the solid-state insulators with an electrolyte. In electrolytes such as ionic liquids (IL), charged ions are free to move and can be driven towards electrodes in the presence of a potential difference between them as depicted in Fig. 3.3 **A**. In Ionic FETs, the applied gate bias moves ions in the electrolyte towards the electrodes and creates two electric double layers (EDLs) [76–78] between the IL/Semiconductor and the Gate/IL interfaces (Fig. 3.3 **B** (bottom)). For instance, if the gate is negatively biased, the negatively charged ions of the electrolyte move towards the semiconductor and holes (positively charged) are accumulated in the transistor channel. In the same spirit, when the gate is positively charged, the negatively charged electrons are induced in the channel. Since the electrolytes behave electrostatically like metals, the Debye screening length is in the order of 1 nm or even smaller. Such a small thickness of the EDLs leads to a large capacitance of these EDLs, and, therefore the whole voltage drops across the IL/Semiconductor interface (in contrast, the voltage drops across the whole thickness of the insulator in MISFETs).

As the majority of electrolytes is present in liquid or glass form, the transistors based on them have a specific geometry. Compared to the traditional FETs with solid dielectrics, the source and the drain contacts are

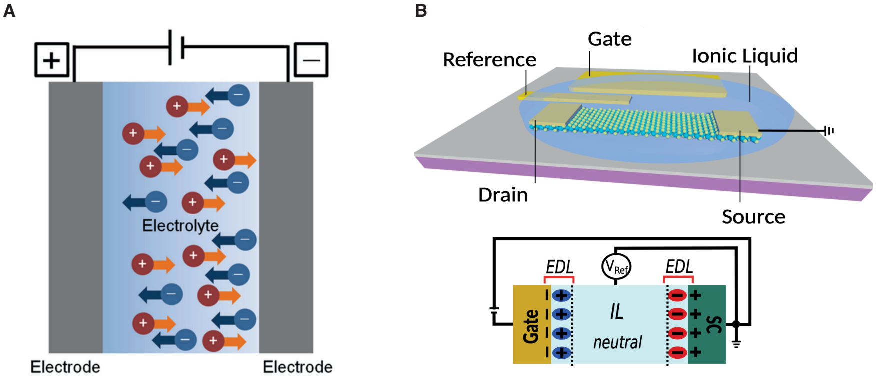

Figure 3.3: **A** Schematics of an electrolyte placed in between two electrodes. In the presence of a voltage difference between the electrodes, ions of the electrolyte move: positively charged ions move towards the cathode, and negatively charged ions move towards the anode. **B** (top) Schematics of an Ionic-gated transistor with the source and drain contacts. A side gate electrode controls the voltage applied to the ionic liquid. Another "Reference" electrode is introduced to monitor the potential drop between the transistor channel and the IL. **B** (bottom) Cartoon of electric double layers –that act as nano-capacitors– formed at the Gate/IL and IL/Semiconductor (SC) under typical bias conditions. Adapted from Ref. [79].

still on top of a semiconductor, but the gate is no longer located on top of the channel area (the gate moved to the side as we show in Fig. 3.3 **B** (top)). Apart from the different geometry, an additional "Reference" electrode –that is not usually present in MISFETs at all– is introduced in the structure of the transistor. The purpose of the Reference is to measure the potential drop between the channel and the electrolyte (it probes the electrostatic potential of the interior of the electrolyte regardless of the potential drop between the gate/IL interface). Strikingly, transistors of this type have enabled observation of phenomena previously inaccessible with traditional FETs such as gate-induced superconductivity, gate-induced ferromagnetism in thin platinum films.

The sub nm thickness of the EDLs leads to a dramatic increase of the gate capacitance $\approx 50\ \mu\mathrm{F/cm}^2$ [76–78, 80–82] as compared to the FETs with solid insulators. For instance, commonly used Si/SiO$_2$ wafers with 300 nm SiO$_2$ thickness give capacitance of 12 nF/cm^2, 4000 times lower than that of EDLs. Even if the thickness of the oxide can be decreased down to 20 nm, the capacitance of that layer –170 nF/cm^2– is 300 times lower than that of EDLs at Electrolyte/Semiconductor interface. The large capacitance of the EDLs makes it beneficial to accumulate enormous charge densities reaching almost 10^{15} carriers/cm^2 in 2D TMDs when applying relatively low gate biases as compared to the MISFETs. Indeed, in conventional FETs, the tuning of the chemical potential of a semiconductor is often insufficient to observe both types of the charge carries. It is limited by the breakdown voltage of the gate dielectric limiting the accumulated charge density. In practice, the voltages applied to IL gate are often in the range of ±3 V. This range is also known as the electrochemical window and its exact value is determined by the electrochemistry of used electrolyte. Outside this window, electrolytes are not stable and may decompose. Also, reduction–oxidation chemical reactions happen quite often destroying electrodes when the voltage exceeds the range of electrochemical stability. The ionic liquids and the lithium ion glasses used in this thesis have electrochemical windows of ±3 V making them a good choice for spectroscopic purposes and suitable for application of extremely large electric fields.

3.4 Ionic-gate spectroscopy

The Ionic FETs can be used as a spectroscopic tool that exploits the extremely large capacitance of EDLs to determine the single-particle gap of a semiconductor [79]. The spectroscopic property of Ionic FETs can be illustrated with a simple equation that relates the change of the chemical potential of the semiconductor $\Delta\mu$ and the variation of the electrostatic potential $\Delta\phi$ caused by the change of the gate voltage ΔV_G:

$$e\Delta V_G = \Delta\mu + e\Delta\phi = \Delta\mu + \frac{e^2\Delta n}{C_G}. \tag{3.8}$$

When the chemical potential is inside the gap, the electrostatic potential term $e\Delta\phi = \frac{e^2\Delta n}{C_G}$ can be neglected due to the very large gate capacitance ($\approx$ 50 μF/cm^2) and low in-gap density of states. Therefore, the change in the chemical potential in the semiconductor corresponds to the change in the gate voltage:

$$e\Delta V_G = \Delta\mu. \tag{3.9}$$

By sweeping the gate voltage in both polarities, we can observe electron and hole transport in the FET transfer curve as we show in Fig. 3.4 **A**. The hole and the electron conduction in the transistor channel begins when the chemical potential crosses the valence and the conduction band, respectively, as illustrated in Figs. 3.4 **B-C**. The gate voltage required for the band to cross the chemical potential is the threshold voltage. Here, the hole/electron threshold voltages are of crucial interest. As we show below, they can be used to quantify the value of the band gap of semiconductor using Eq. 3.9. To extract the threshold voltages, we extrapolate the I$_{SD}$ to 0 (dashed lines in Fig. 3.4 **A**) from the linear regimes of transfer curves.

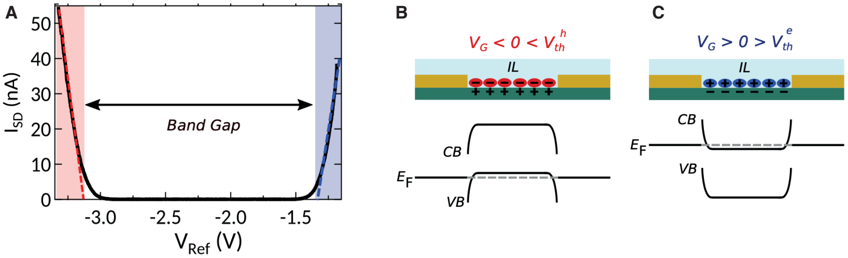

Figure 3.4: **A** The source-drain current I_{SD} (the transfer curve) of ionic-gated multilayer MoS_2 transistor measured as a function of the reference potential V_{Ref}. The dashed lines represent extrapolation of the linear part of transfer curves to zero current (red line is for holes, and blue one is for electrons). The intersection of the interpolated line with the abscissa gives the threshold voltage. When the gate voltage V_G is larger than the threshold voltage V_{th}^h, the valence band crosses the chemical potential and holes appear in the semiconductor from the contacts (**B**) (red region). (**C**) In the case when V_G is larger than the threshold voltage V_{th}^e, electrons are accumulated in the semiconductor (blue region). The difference in V_{Ref} between the hole and electron thresholds corresponds to the value of the band gap. Adapted from Ref. [79].

When the gate voltage is near its threshold values for the electron and hole conduction, the accumulated charge density in the semiconductor is vanishingly small so is the electric field perpendicular to the surface of the semiconductor. As we have seen in **Section 2.5**, only a very high perpendicular electric field modifies the band structure dramatically. As long as the chemical potential is in the gap, Eq. 3.8 is valid and the difference between the electron and hole threshold voltages gives the value of the band gap.

3.5 Double ionic gating

So far, we have only discussed transistors in a single gate configuration. There, the gate bias controls inseparably the electric field perpendicular to the semiconductor and the accumulated charge (the larger the electric field, the larger the induced charge). However, the situation changes when sandwiching the semiconductor between two gates. The new double gate configuration has now some advantages compared to the single gate geometry in FETs. Among them is an independent control of the charge density and the applied electric field as we will see from an example below. As the simplest case, we take equal capacitances for the top and the bottom gate. Then, the induced charge density is proportional to the sum of the gate voltages, while the electric field depends on the voltage difference between the gates. Since the gate voltages can be controlled independently, one can now control the charge density (by changing only the sum of the gate voltages) while keeping the electric field constant and vice versa. Typically, double-gated transistors have solid insulators for the top and the bottom gates. The use of common solid insulators limits the magnitude of achieved electric fields and charge densities as well as the number of phenomena that can be observed with this approach. Therefore, there is a need for better techniques and strategies for the field to develop further.

A solid substrate such as Li-ion glass-ceramic has enabled ionic gating of TMDs, and it allows the realization of a new type of devices – double ionic-gated transistors. Using ionic gates instead of common insulators is advantageous not only due to the possibility of reaching very large charge carriers densities, but also giant electric fields (of the order of a few volts per nanometer), which have not been accessible before with previous devices. Such large electric fields can strongly modify the band structure of semiconductors –multilayer TMDs as an example– as we have discussed in **Chapter 2**. The double ionic gate geometry consists of a Li-ion glass ceramic substrate acting as back-gate and of a top ionic liquid acting as top gate. The two gates are decoupled both physically and electrostatically by a grounded aluminium plate sandwiched in alumina as we show in the Fig. 3.5. This configuration allows one to control both gates independently from each other, with two reference electrodes measuring the response of the ionic liquid and the ceramics to their applied gate voltages. The exact fabrication details are discussed in **Chapter 4**.

What enables the application of very large electric fields in our devices is the extremely large geometrical capacitance of ionic gates, which originates from the formation of electrical double layers at the interface between the two electrolytes and the gated material. When a voltage is applied between the gate and the device, the resulting electric field is screened by very thin layers of charge accumulated next to the gate and next to the devices, so that the bulk of the electrolyte is equipotential. These screening layers at the two interfaces are the so-called electrical double layers. The extremely large density of charge in the electrolytes causes the thickness t of these layers to be typically 1 nm or smaller, so that the associated geometrical capacitance per unit area ($C_G = \epsilon/t$) is huge, typically of the order of 50 μF/cm^2 (as measured in a number of earlier studies [76, 77, 80], including a recent study of the quantum capacitance of ionic gated transistors based on TMD monolayers [82]). As discussed in Ref. [81], Li-ion glass substrates have a capacitance that is closely comparable to that of ionic liquid, and it is a good approximation to assume that the capacitance of the ionic liquid used in our devices and of Li-ion glass substrates is the same.

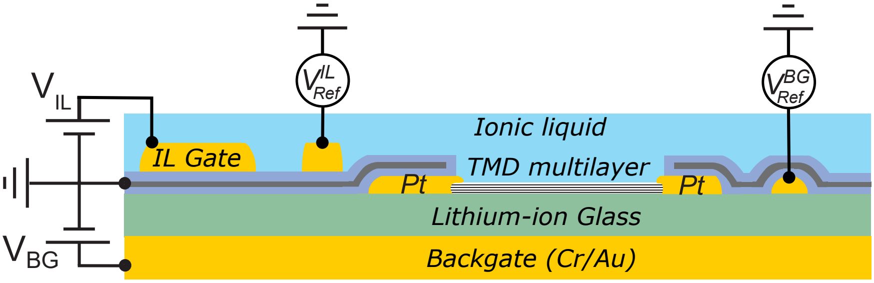

Figure 3.5: A Side view schematics of a double ionic gated device, showing a multilayer TMDs contacted with two Pt electrodes and the reference electrodes in contact with the Li-ion gate (buried below the decoupling trilayer) and with the ionic liquid (deposited above the decoupling trilayer). The schematics also shows the biasing configuration and the measurement units to record the voltage of the two reference electrodes.

In the transistors realized in this thesis, the applied gate voltages drop entirely over the interface between the electrolytes and the WSe$_2$ multilayer. Indeed, the voltage drop at the interface between electrolytes and gate electrodes is negligible (both for the gate in contact with the ionic liquid and for the gate on the back of the Li-ion glass substrate), because the gates are intentionally fabricated to have a much larger contact area with the electrolyte than the WSe$_2$ multilayer (including all the electrodes that also contribute to the capacitance), so that the gate-electrolyte capacitance is much larger than the electrolyte-device capacitance. The validity of these considerations is well-established from past work on ionic (single) gate transistors [79] and it can be checked experimentally by using the reference electrodes present in the devices fabricated for this thesis (see also **Chapter 7**). These electrodes measure directly the change in potential of the electrolyte upon a change in the potential applied to the gate, and allow monitoring that the voltage drop at the gate-electrolyte interface is indeed negligible. The net result is that the voltage applied to each one of the gates (the ionic liquid gate and the gate on the back of the Li-ion substrate) is transferred with virtually 100% efficiency to the interface between the corresponding electrolyte and the TMD multilayer (as discussed in **Chapter 7**, the Al shielding layer further ensures that there is no direct coupling between the two electrolytes and that the gate in contact with one of the electrolyte does not influence the other electrolyte).

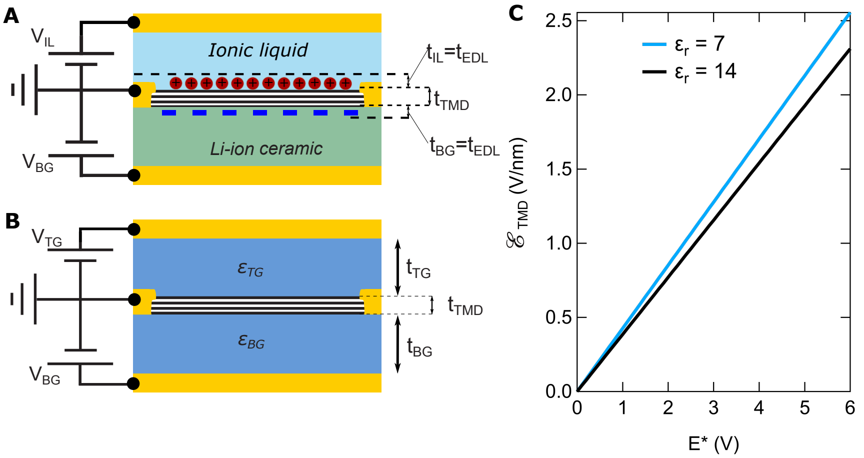

Figure 3.6: Schematics of a WSe_2 field-effect transistors equipped with top and bottom gates fabricated with electrolytes (**A**) and with conventional solid state gates (**B**). To estimate the electric field applied onto the TMD layer, the devices can be modeled as a stack of multiple dielectric layers arranged in series. In contrast with solid state dielectrics in which the applied gate voltages drop across the entire thickness of the material t, in the electrolytes the voltage drop occurs across the electric double layers (EDL), whose thickness (determined by the Debye screening length) is smaller than 1 nm. This results in huge values of the gate capacitance and has important implications for the applied electric field, as discussed in Section S5. **C** Calculated values of the electric field $\mathscr{E}_{TMD}$ present in a 3L WSe_2 crystal placed between top and bottom ionic gates, as a function of $E^* = V_{IL} - V_{BG}$ for different values of the relative dielectric constant of WSe_2. The plot shows that –owing to the very large capacitance of the ionic gate– the electric field applied onto the TMD is only weakly sensitive to the multilayer dielectric constant.

These considerations are important to properly describe the electrostatics of our devices, and to relate the total voltage drop $E^* = V_{IL} - V_{BG}$ to the electric field $\mathscr{E}$ applied across the TMD multilayer. To this end, we view the two electrical double layers at the surface of the electrolytes and the TMD multilayer itself as a stack of dielectric materials, each with its corresponding thickness and dielectric constant (see Fig. 3.6**A**). In the presence of a potential drop E^* across the stack, charge conservation ensures that the displacement field D has the same value in all layers. We can then write (see Fig. 3.6) :

$$D = \varepsilon_{IL}\mathscr{E}_{IL} = \varepsilon_{TMD}\mathscr{E}_{TMD} = \varepsilon_{BG}\mathscr{E}_{BG} \tag{3.10}$$

$$V_{IL} - V_{BG} = E^* = \Delta V_{IL} + \Delta V_{TMD} + \Delta V_{BG} \tag{3.11}$$

where the subscripts IL, BG and TMD stand for ionic liquid (the top gate), bottom gate and the transition metal dichalcogenide crystal. Since for each layer the electric field is $\mathscr{E} = \Delta V/t$ and the expression for the capacitance reads $C = \varepsilon/t$, the equalities in Eq. (3.10) can be rewritten as:

$$C_{IL}\Delta V_{IL} = C_{TMD}\Delta V_{TMD} = C_{BG}\Delta V_{BG} \tag{3.12}$$

As the capacitance of the ionic liquid and of the Li-ion glass ceramic gates are approximately equal ($C_{IL} \approx C_{BG} \approx C_G = \varepsilon_G t_G$), we also have $\Delta V_{IL} = \Delta V_{BG}$. We can then find the electric field inside the TMD, as :

$$\mathscr{E}_{TMD} = \frac{\Delta V_{TMD}}{t_{TMD}} = \frac{E^*}{t_{TMD}}\left[2\frac{C_{TMD}}{C_G} + 1\right]^{-1} \tag{3.13}$$

This expression illustrates the important role played by the extremely large capacitance of the electrolytes ($C_G = 50\ \mu$ F/cm^2), which ensures the efficient transfer of the applied gate voltage to the TMD. Indeed, because the ratio $C_{TMD}/C_G \ll 1$, virtually all the applied voltage drops across the TMD itself and not across the electrical double layers in the electrolytes. That is the reason why in our ionic gated devices $\Delta V_{TMD}/E^* \simeq 90\%$ or better and why electric field values $\mathscr{E}_{TMD}$ in excess of 2 V/nm can be reached at the largest gate voltage difference applied in our experiments (E^*= 5.5 V – 6 V).

To illustrate this conclusion –as well as its insensitivity to the precise value of the dielectric constant ϵ_r of the TMD multilayer– Fig. 3.6**C** shows the dependence of $\mathscr{E}_{TMD}$ on E^* for a 3L WSe$_2$ double ionic gated device, for $\epsilon_r = 7$ (the value commonly taken for atomically thin TMD layers, blue line) and for $\epsilon_r = 14$ (black line). Even when an unrealistically large value for $\epsilon_r = 14$ is used, the electric field in the TMD multilayer is reduced by only 10%, and values in excess of 2 V/nm can still be reached at the largest gate voltages applied in our experiments. As we show below, it is not possible to reach such large electric fields in devices equipped with conventional gates (note that we are discussing the actual electric field and not the displacement field $D = \epsilon_r\mathscr{E}$, which is often reported in the literature in the discussion of double gating experiments).

In comparing our double ionic gated devices with devices based on conventional solid state dielectrics, we also note that the maximum electric field reached exceeds 2 V/nm. This value is significantly larger than the breakdown electric field of virtually all insulators, as extracted from common electrical measurements. Such a conclusion may seem surprising, but it is nevertheless possible because the breakdown electric field measured by common electrical measurements (i.e., by using metallic electrodes and detect at which applied voltage an abrupt, irreversible increase in current occurs) does not represent the maximum, intrinsic field that an insulator can sustain. Indeed, although the precise microscopic mechanisms responsible for breakdown of insulators are still matter of investigation, there is broad consensus that the breakdown observed in conventional electrical measurements is induced by a runaway process caused by the flow of current through the insulator itself. In simple terms, the leakage current flowing at large applied voltage (due, e.g., to charge injection into defect states in the insulators) causes power dissipation that results in heating. Heating leads to a further increase in leakage current, thereby generating more dissipated power, starting a positive feedback loop that ends up with the insulator breakdown [74, 75]. In our double ionic gated devices this mechanism is not at play, because the charge that creates the electric field across the WSe_2 multilayer is due to ions, and not to electrons as in the case of conventional metallic gate electrodes. As a result, upon biasing the ionic gates, no leakage current flows through the WSe_2 multilayer, and no power dissipation occurs. This is why in our double ionic gated devices an electric field significantly larger than the field extracted from common breakdown measurements of insulators can be applied.

CHAPTER 4

Experimental methods

The realisation and characterisation of high quality devices and van der Waals heterostructures based on 2D semiconducting layers is a pivotal part of the experiments performed in this thesis. Here we describe in detail aspects of fabrication of these devices and heterostructures as well as various techniques used to identify individual layers and to explore their properties under different experimental conditions.

4.1 Exfoliation and identification of 2D materials

Mechanical exfoliation is a simple method to deposit atomically thin layers onto a substrate. This technique facilitated the discovery of 2D materials [3, 9] and it is still the most common way to produce them. To perform the exfoliation, there is no need of sophisticated tools. In fact, many of us already have the main instrument for exfoliation – a scotch tape. To start off the exfoliation, a piece of scotch tape is attached to a bulk crystal and then removed from it, leaving the top of the crystal on the scotch tape as we show in Fig. 4.1 **A**. The crystal on the tape is then further thinned down by another strip of a fresh tape (Fig. 4.1 **B**). In the next step the colour and the density of crystals remained on the tape are evaluated. Once the tape has a sufficiently large area of relatively thin crystals on it, such a tape is placed onto a clean Si/SiO_2 substrate (Fig. 4.1 **C**). The scotch tape together

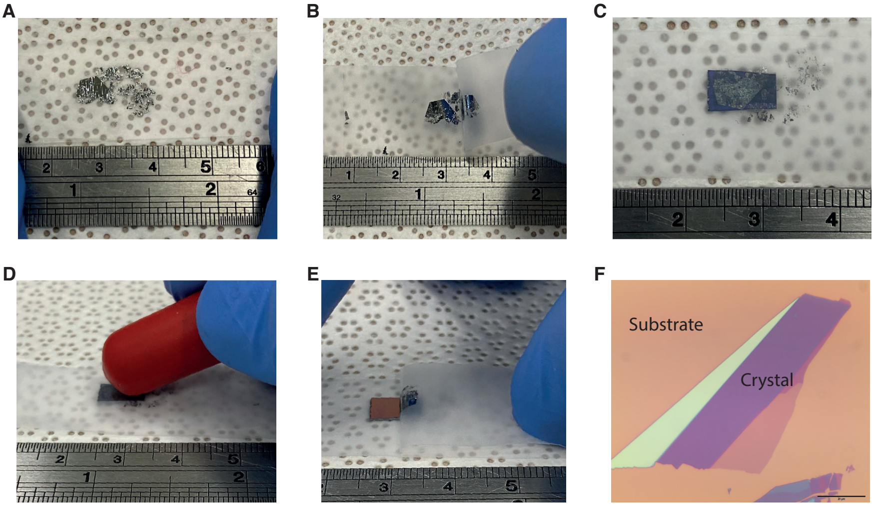

Figure 4.1: Isolation of atomically thin materials via micromechanical cleavage. **A** Image of the WSe_2 crystal on a scotch tape. **B** The crystal is thinned down by cleaving it with another scotch tape. **C** After the cleavage, the scotch tape with crystals is aligned with a Si/SiO_2substrate (the large part of the crystal should overlap with the substrate). **D** The tape is then rubbed by a soft piece of plastic (tweezers cap) for at least 5 minutes and later **E** removed from the substrate. This procedure results in the deposition of atomically thin crystals onto the substrate **F**. The scale bar in **F** is 20 μm, while the scale in **A**-**E** is indicated on the metallic ruler in mm (top ticks).

with the substrate is then rubbed for at least 5 minutes (Fig. 4.1 **D**) and then slowly peeled off (Fig. 4.1 **E**) leaving atomically thin layers on the substrate (Fig. 4.1 **F**).

To identify atomically thin crystals and discriminate their thickness, an optical microscopy is often used first. This type of identification of 2D materials is particularly interesting due to its simplicity and accessibility to promptly spot crystals and identify their thickness [83–87]. When a 2D crystal is deposited onto a substrate, it changes the reflectivity of the substrate (Fig. 4.2**A**) resulting in intensity contrast (optical contrast) between the substrate and the crystal when illuminated, therefore, allowing to spot and identify the crystals. In case of Si/SiO_2 substrates, carefully choosing the thickness of the oxide layer leads to the enhancement of the optical contrast due to the constructive Fabry-Pérot interference. The optimal thickness of the oxide layer of 275 nm results in significant sensitivity for the 2D layers (TMDs in particular) to be detected with eyes (Fig. 4.2**B**). As we discuss in **Chapter 6**, we recently discovered a new imaging technique. It allows observing 2D materials with diffusely reflected light and facilitates spotting crystals and determine their thickness in a fast and efficient way.

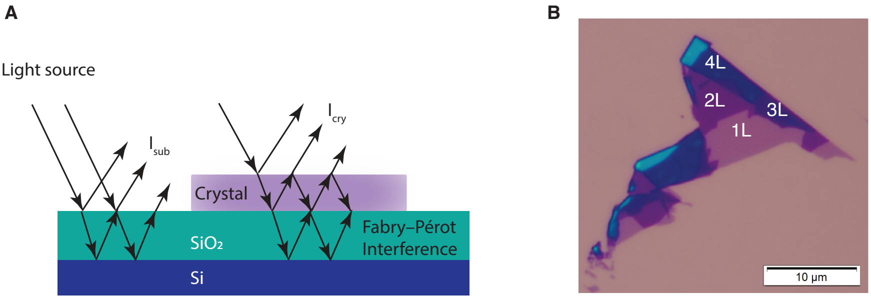

Figure 4.2: **A** Schematics of an atomically thin crystal placed onto a Si/SiO$_2$ substrate. The Si/SiO$_2$ stack acts as an open Fabry-Pérot cavity. Multiple reflections take place inside the oxide layer, when the stack is illuminated with light. The interference enhances the optical contrast proportional to the difference of intensities of the light reflected from the substrate I$_{sub}$ and from the crystal I$_{cry}$. **B** An optical image of a multilayer WSe$_2$ crystal on a Si/SiO$_2$ substrate with 275 nm thick SiO$_2$(this thickness is optimal to observe semiconducting TMDs). The crystal is easily visible, and the regions of different thickness (1L-4L) can be clearly recognized. The scale bar is 10 μm.

However, for materials giving a weak optical contrast regardless the use of imaging conditions or when doubting the thickness of a particular layer, other techniques are more useful.

To overcome the issue of poorly detecting thin layers and distinguishing their different thicknesses with an optical microscope, an Atomic Force Microscopy (AFM) can be used as an alternative to the optical contrast when identifying different thicknesses of the material of interest. In AFM, the thickness is measured with the pm precision. As a matter of fact, measurements of the absolute thickness of a 2D crystal in some cases can be difficult due to the electrostatic charging of the material on insulating substrates or the presence of adsorbents on the crystal surface and/or on the substrate surface. In those particular cases, the correct thickness can be sometimes identified if the AFM is used in the contact mode, and/or if the thin material is on an atomically flat substrate such as 2D layers of h-BN. As we can see from Fig. 4.3 **A** in the height topography of the flake shown in Fig. 4.2 **B**, the measurement of the height from the substrate to the 1L region of a WSe$_2$ crystal results in roughly 3.0 nm (Fig. 4.3 **B**), that is much larger than the real thickness of WSe$_2$ monolayer ($\approx$ 0.7 nm). Despite that, if the height is measured from the 1L to the 2L region of the WSe$_2$ crystal, the measurement gives a more reasonable step height of $\approx$ 0.8 nm.

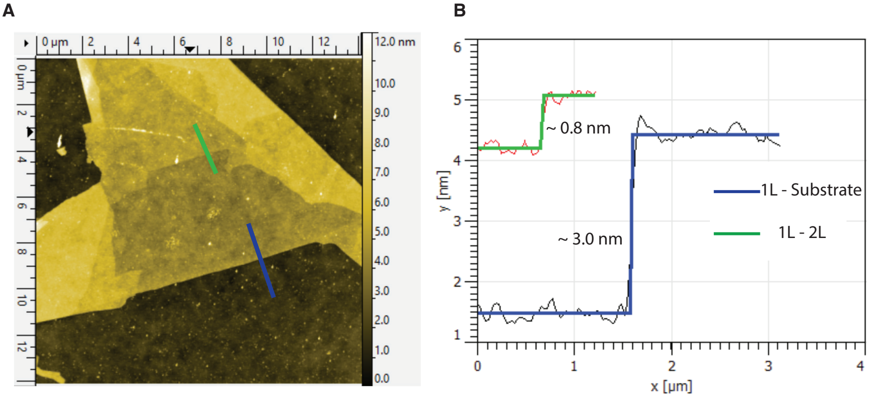

Figure 4.3: **A** A false colour AFM topography image of WSe_2 crystal shown in Fig. 4.2 **B**. The two lines cross the substrate-monolayer region (blue line) and the monolayer-bilayer region (green line), where the height profile is later analysed. **B** Step-like height profiles along the lines indicated in **A**. The step from the substrate to the monolayer is 3.0 nm (much larger than the thickness of a monolayer $WSe_2 \approx 0.7$ nm), while the step from the monolayer to the bilayer results in 0.8 nm.

Another powerful tool in thickness identification of atomically thin TMDs is Photoluminescence (PL) Spectroscopy [70], a technique based on the detection of radiative recombination of photoexcited electrons and holes. The photoexcited carriers relax to the lowest energy state –optical band– and then recombine emitting photons with the energy corresponding to the optical band gap. Depending on the nature of the band gap of a semiconductor –whether it is direct or indirect in momentum space– the intensity of the PL signal exhibits different behaviour. Optical transitions in direct gap semiconductors show higher PL signal compared to the PL from indirect gap semiconductors. The reason for that mainly originates from the requirement to emit a phonon for conserving the momentum in optical transitions of indirect band semiconductors. Since the band gap of TMDs and InSe is very sensitive to the layer thickness due to the spatial quantum confinement effect (see **Chapter 2**), so is the PL signal from these materials. This implies that the layer number identification is straightforward when performing PL measurements. For instance, as we show in Fig. 4.4 **A**, the PL signal from WSe_2 crystals of different thickness shows a PL peak from the direct K-K transition **(DT)** and from another indirect Q-Γ transition **(IT)**. The PL signal from 1L WSe_2 crystals is much stronger than from the thicker layers. The quantity λ_{IT-DT} – the difference in the peak positions of IT and DT– is often used to discriminate different thicknesses as depicted in Fig. 4.4 **B**. In practice, the peak position of direct/indirect transitions may slightly vary spatially from one place to another on the crystal. However, λ_{IT-DT}

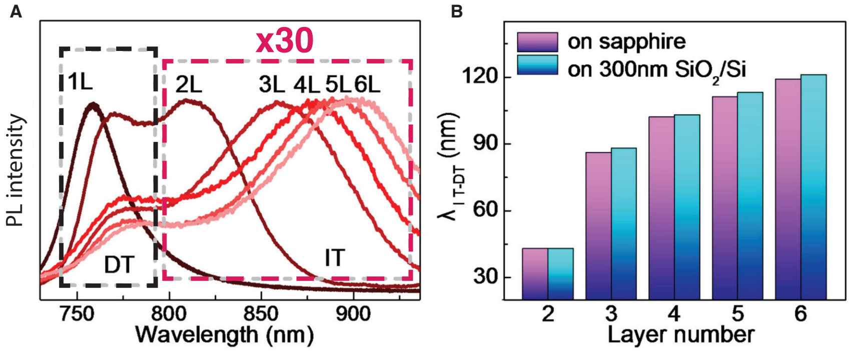

Figure 4.4: A Thickness dependence of WSe_2 PL spectrum. For 2L-6L thick WSe_2 crystals, the PL intensity is multiplied by a factor of 30. The spectrum of monolayers features a peak around 760 nm arising from the direct K-K transition. Its intensity is significantly larger than the one for the same transition in thicker layers. The position of the PL peak originating from indirect Q-Γ transitions (IT) in thick layers ($\geqslant$ 2L) shifts to the right (lower energies), as expected due to the spatial quantum confinement effect. **B** The difference in the peak position between the IT and DT λ_{IT-DT} as a function of WSe_2 layer number on different substrates (purple bars for sapphire, and blue bars are for the 300 nm SiO_2/Si substrate). λ_{IT-DT} increases as the crystal thickness is increased by a significant value to make layer identification feasible. Adapted from Ref. [70].

displays virtually no spatial dependence since the DT and the IT are affected in the same way. This is exactly why λ_{IT-DT} is a good quantity for layer identification of TMDs. Apart from the thickness identification, the PL signal can be also used to probe the nature of the band gap (direct/indirect) of a semiconductor or interfaces of semiconductors as we show in **Chapter 5**.

4.2 Transfer of 2D materials and assembling of heterostructures

Having been isolated and identified, atomically thin materials can be stacked on top of each other forming heterostructures (HTs) [42, 88–92]. The central idea is quite clear: take one material from substrate "A", then put it on top of another material on substrate "B", add other 2D layers and so on – almost like building toys from LEGO bricks. The resulting stack acts as an artificially created material assembled in a controlled fashion. The same weak van der Waals forces that allow exfoliation of the 2D layers hold the layered materials in a heterostructure. This type of interaction between the layers lifts limitations on the lattice parameters and the crystalline structure of the stacked materials allowing virtually all 2D materials assembled into vdW HTs.

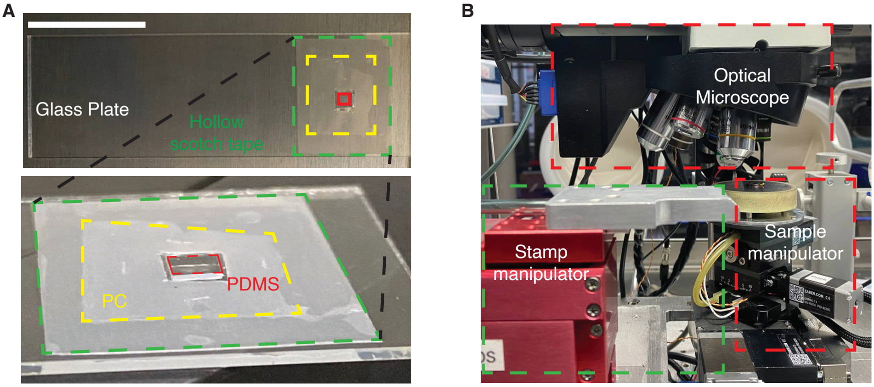

Figure 4.5: A Photograph of an in-house made PC transfer stamp (top). Dashed contours of different colour represent various parts of the stamp. The stamps are made of thin films of PC that cover rectangular pieces of PDMS placed onto glass-plates. The film is fixed by a piece of scotch tape with a rectangular hole. The PC films are obtained by spinning a clean glass-slide with a drop-casted PC solution in chloroform (50 mg/ml) on it at 3000 rpm for 60 seconds followed by a lift-off with the scotch tape. The scale bar is 2.5 cm. **B** Home-build transfer setup (placed inside a nitrogen-filled glove box). The setup consists of a motorized stamp manipulator, a sample manipulator with a temperature-controlled sample holder, and an optical microscope. Stamp, substrate, and microscope focal point are controlled with joysticks outside the glove box.

To built vdW HTs of different materials or to transfer a material from one substrate to another, we use the so-called all-dry pick-up/transfer approach [92, 93]. It is based on poly-carbonate (PC) transfer stamps (Fig. 4.5 **A**) that pick up 2D materials. A PC stamp is manipulated under an optical microscope to precisely control the stacking of layers. Substrates with target 2D materials for a pick-up are placed onto a sample manipulator. In our home-made transfer setup, we use nano-positioners (with the motor step size of 50 nm) allowing independent control of the stamp and the substrate. Also, there is an additional control of tilt/pitch/rotation degrees of freedom for a straightforward material alignment during transfers. Since we work with humidity/air sensitive materials such as InSe (**Chapter 5**) and black phosphorus (see **Chapter 6**), we perform all transfers in a nitrogen filled glove-box.

Once PC stamps are ready, they are mounted onto stamp manipulator and we can transfer crystals from one substrate onto another or onto a different 2D material. The process flow of the transfer of 2D layers is presented in Fig. 4.6. To pick a first crystal, the stamp is positioned above the target layer on the substrate preheated at 130° C. Next, the stamp is brought into contact

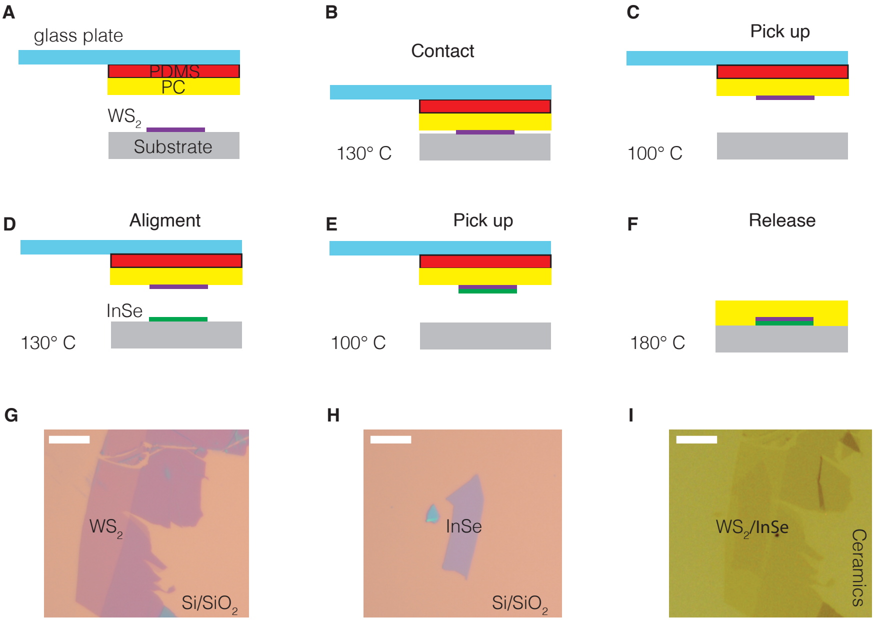

Figure 4.6: Schematics of the transfer technique based on PC-stamps. The process flow is illustrated for assembling InSe/WS_2 van der Waals heterostructures. **A** A PC stamp is first positioned above a WS_2 flake on a substrate, and then contacts the crystal on the substrate at 130°C (**B**). The WS_2 crystal sticks to the stamp and then detaches from the substrate (**C**) when the stamp is lifted up (adhesion of the crystal to the PC is higher than to the substrate). The substrate is then switched to the one with an InSe crystal. Next, WS_2 crystal is aligned with the InSe crystal (**D**). Similarly to the previous steps, the stamp picks up the InSe forming an WS_2/InSe stack. **F** As the final step, the heterostructure is released onto a fresh substrate at 180°C –just above the glass-transition temperature of the PC film– by tearing away the film from PDMS. The polymer is then dissolved in chloroform, leaving the surface of the stack clean. Optical images of **G** WS_2 and **H** InSe crystals on Si/SiO_2 substrate that are later transferred onto a lithium ion-glass ceramic substrate (**I**) using the described transfer technique. The scale bar in **G**, **H**, and **I** is 10 μm.

with the substrate and the crystal sticks to the PC film. After 1 minute, we cool down the substrate to 100° C. Once the temperature is stable, the stamp is lifted up from the substrate. The crystal stays on the stamp, and then –depending on the final goal– it can be either transferred onto the desired substrate or used for further pick-ups to assemble a complex heterostructure. Once the final stack of materials is assembled, it is then brought into contact with a clean substrate followed by heating up the substrate to 180° C and lifting up the stamp at that temperature from the substrate. By lifting up the stamp at 180° C, the assembled stack of materials stays on the substrate together with the PC-film, which is then removed with chloroform. The described technique to assemble van der Waals heterostructures, in principle, has no limits to the number of layers that can be placed on top of each other.

4.3 Electron beam lithography and contact deposition

Having assembled a heterostructure or transferred the desired material onto a new substrate, one needs to define electrical contacts in order to characterise the transport and optoelectronic properties of the system. Defining electrical contacts to the material is often not the only fabrication step required for a device. For instance, as we have discussed in previous chapter, double ionic-gated transistors require an Alumina/Al/Alumina trilayer to electrostatically decouple the two gates. The relative position of the trilayer and the TMD crystal is extremely important –there should be no gaps or big overlaps between them– to guarantee the correct operation regime of our double ionic gated transistors. For these transistors, the fabrication of masks for contacts, decoupling trilayer deposition, and etching requires high precision. In practice, that can be done using electron-beam (E-Beam) lithography. That is why we describe this powerful technique below.

The idea behind the e-beam lithography relies on the use of polymers or resists that can be exposed with a beam of electrons. Depending on the nature of a resist, the minimum feature size drawn with e-beam varies strongly. For our devices, we use poly methyl methacrylate (PMMA) resists of different molecular weight (MW) that are exposed with an e-beam to pattern desired masks (Fig. 4.7 **A**). The best resolution achieved with PMMA is approximately 10 nm when using a well-focused beam and a very good process flow. Being a positive resist, only exposed by e-beam areas of PMMA are removed when using a developing solution (Fig. 4.7 **B** and **C**). When the resist is developed, the device is ready for a next fabrication step.

In general, depending on the purpose of the resist mask, the PMMA of a suitable MW is selected. A two-layer PMMA process flow is used for standard contact pattering. To form the two layers, first, a low MW PMMA is spun onto the substrate and later baked at 180°C. Second, another layer of high MW PMMA is then spun and later baked at the same temperature as the first layer. After that, masks are ready to be patterned with an E-Beam lithographer. For the very well controlled development of resists and high resolution, we use the cold IPA/water solution with a volume ratio of 3:1. When the bilayer PMMA is developed, an undercut forms in the bottom layer. This happens due to the higher sensitivity of the bottom layer (as compared to the top layer of higher MW) to the electron beam. The undercut (Fig. 4.7 **B**) prevents the side-wall coating of the mask in the next fabrication step – metal deposition for contacts (Fig. 4.7 **D**. Typically, the metal is deposited in an electron-beam evaporator under a high vacuum.

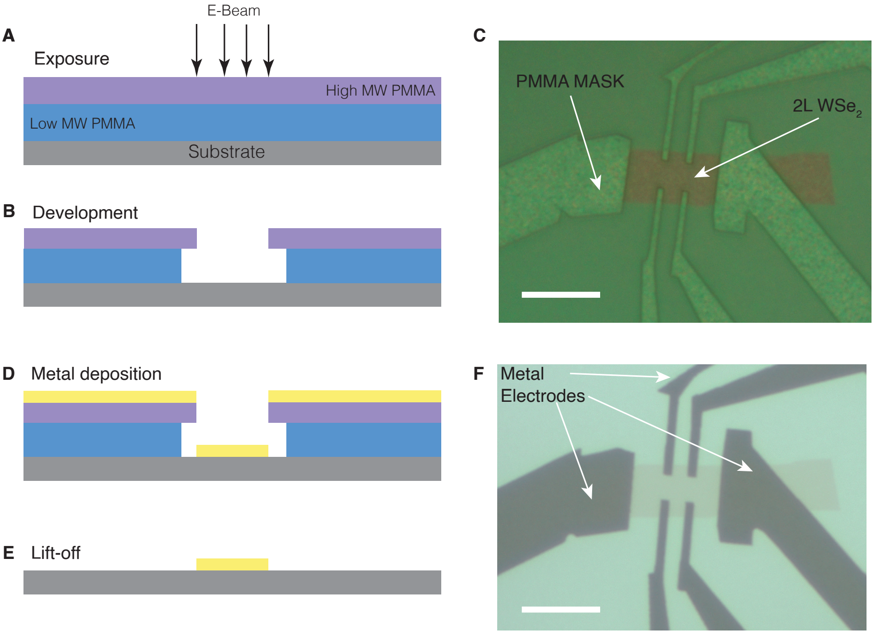

Figure 4.7: **A** Schematics of a substrate covered with bilayer PMMA that is exposed to an e-beam. **B** Exposed part of PMMA is removed during developing in the cold IPA/water solution. **C** A photograph of the developed PMMA mask for an actual device. The mask is designed for metal electrodes deposition onto a bilayer WSe$_2$ crystal. During metal deposition, the metal is deposited onto the substrate (through the developed area in the mask) and on the mask itself **D**. Next, the polymer mask is dissolved in acetone, with the metal covering it being lifted off. Metal deposited onto the substrate stays intact **E**. **F** An optical image of the device with deposited contacts (the mask is shown in panel **C**). The scale bar in **C** and **F** is 10 μm.

Later, to remove the mask with the metal covering it from the substrate, we place them in acetone. Acetone dissolves the PMMA mask lifting off the metal previously covering PMMA. The metal that was deposited through the mask stays on the substrate intact as we show in Fig. 4.7 **E-F**. Once the contacts are ready, further lithography steps might be needed depending on the device geometry. Otherwise the device can be bonded onto a chip carrier for transport measurements.

4.4 Fabrication of high-quality double ionic gate and conventional double-gated transistors

The results that will be presented in **Chapter 7** are obtained using high quality double ionic gated devices. This type of devices has never been realized before (all previous work on ionic gating has been done on devices comprising only one gate), and that is why in this section we discuss their fabrication in detail as well as how we implement previously described techniques. We also discuss the fabrication of conventional double-gated devices to compare the performance with double ionic gated transistors.

The devices rely on atomically thin, exfoliated crystals of WSe_2. Few-layer WSe_2 crystals can be exfoliated and identified [94] directly on the Li-ion conductive glass ceramic substrates (LASPT, purchased from MTI Corporation). However, we found that thick exfoliated crystals, which are commonly also present when exfoliating directly on Li-ion ceramics, can compromise the integrity of the layer used to electrostatically decouple the ceramic from the ionic liquid (see **Chapter 7** for more details). Therefore, it is preferable to exfoliate WSe_2 on Si/SiO_2 substrates (Fig. 4.8**A**), select atomically thin crystals of the desired thickness and size, and employ existing techniques [93] to transfer them onto the Li-ion glass ceramic substrate (Fig. 4.8**A**-**B**). The electrical contacts to the crystals and the reference electrode for the Li-ion ceramic substrate (see Fig. 3.5) are subsequently defined by means of electron-beam lithography, evaporation of a Pt/Au (5/15 nm) layer, and lift-off (Fig. 4.8**C**-**D**). The entire back side of the ceramic is covered with a Cr/Au (10/50 nm) layer, acting as gate for the Li-ion ceramic electrolyte. Up to this point, all fabrication steps are virtually identical to those that we employed to realize single-gate monolayer TMD transistor, using Li-ion ceramics as gate electrolytes (see Ref. [81]). The fabrication steps that follow are needed to ensure that the top ionic liquid gate is electrostatically decoupled from the bottom Li-ion gate, which is essential for the two electrolytes to have different potentials, and be controlled independently one from the other using the two different gate electrodes.

To electrostatically decouple the Li-ion ceramic electrolyte from the ionic liquid we deposit an $Al_2O_3/Al/Al_2O_3$ (60/30/30 nm) trilayer, and ground the central Al layer during all our experiments. In practice, we use electron-beam lithography to define a PMMA mask on top of the WSe_2 crystal (Fig. 4.8**E**), and then deposit the $Al_2O_3/Al/Al_2O_3$ trilayer in a RF-magnetron sputtering chamber, without breaking the vacuum between

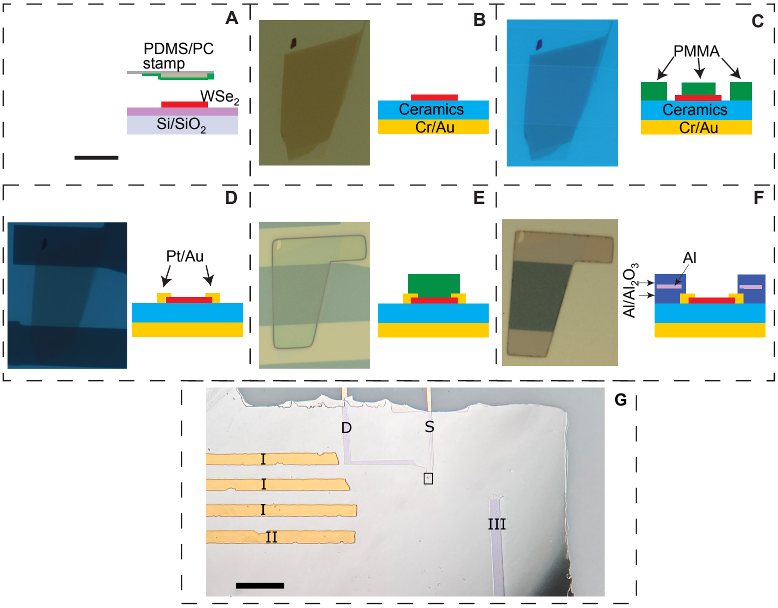

Figure 4.8: Fabrication of double ionic gated field-effect transistors. The left and right panels from **A** through **F** show optical microscope images and schematic side views of the device at different stages of the fabrication. **A** and **B** show the transfer of a 4L WSe$_2$ crystal from a Si/SiO$_2$ substrate to the Li-ion glass ceramic substrate equipped with a Cr/Au gate electrode. The scale bar in **A** represents 20 μm. **C** through **F** illustrate the nano-lithography steps followed to fabricate the electrical contacts to the device and the deposition of the Al$_2$O$_3$/Al/Al$_2$O$_3$ trilayer used to electrostatic decouple the Li-ion ceramic electrolyte from the ionic liquid. **G** Optical microscope image of a completed device (prior to the deposition of the ionic liquid). The IL gate and reference electrodes, labelled as I and II respectively, are visible on the left in the form of four golden stripes. The Drain (D) and Source (S) contacts are visible below the oxide trilayer, as well as the backgate reference electrode (III). The scale bar on the bottom left is 1 mm and the area delimited by the small black rectangle is shown in panel F.

the deposition of the different layers. Both the Al and the Al$_2$O$_3$ layers are deposited from an Al target, using a mixture of Ar and O$_2$ gas for the Al$_2$O$_3$ layers and pure Ar for the Al layer. Following lift-off, the whole substrate is covered with the trilayer, except the area masked by the PMMA, leaving behind a window for the ionic liquid to be in direct contact with the WSe$_2$ crystal (Fig. 4.8**F**). Prior to the deposition of the ionic liquid, Cr/Au metal stripes acting as gate and reference electrodes for the ionic liquid gate are defined by evaporation through a shadow mask onto the trilayer film (Fig. 4.8**G**). The image shows the shadow-evaporated top gate electrodes (labelled as I) and top gate reference electrode (labelled as II), as well as the Pt/Au Drain (D) and Source (S) contacts, and the backgate reference electrode (labelled III on the Fig. 4.8**G**) buried below the trilayer. Finally, a droplet of ionic liquid (1-butyl-1-methylpyrrolidinium tris(pentafluoroethyl)trifluorophosphate ($[P14]^+[FAP]^-$)) is drop casted onto the substrate covering the gate, the reference electrode, and the WSe_2 crystal (through the opening defined in the $Al_2O_3/Al/Al_2O_3$ trilayer).

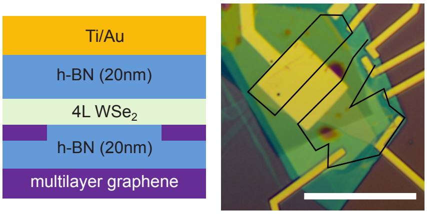

Figure 4.9: Schematic side view (left) and optical microscope image (right) of the device with double hBN gates. The black lines show the position of the multilayer graphene contacts. The scale bar represents 20 μm.

In **Chapter 7** we also discuss double gating experiments performed on a 4-layer (4L) WSe_2 device equipped with conventional solid state gates (with h-BN exfoliated crystals as gate dielectrics), in which we do observe a partial suppression of the band gap but not a complete quenching. The fabrication of this device is based on techniques that are by now conventional in the field of 2D materials, and here we only discuss the basic aspects. Fig. 4.9 shows a schematic cross section (left panel) and optical microscope image (right panel) of the device. The top gate is formed by a Ti/Au film separated from the WSe_2 multilayer by a top h-BN crystals, and the bottom gate consists of a graphite flake that is again separated from the WSe_2 multilayer by an h-BN crystal (both h-BN crystals are approximately 20 nm thick). The electrodes contacting the WSe_2 multilayer consist of exfoliated few-layer graphene strips. The structure was assembled by the consecutive stacking of all the crystals using a PDMS/PC stamp, following established procedures discussed in the previous sections. Electrical contacts to the few-layer graphene electrodes are so-called "side-contacts", which were defined by means of conventional electron-beam lithography, reactive ion etching (CF_4:O_2) of the h-BN/few-layer graphene/h-BN stack and e-beam deposition of Ti/Au (20/40 nm). The Ti/Au (10/50 nm) top gate electrode and the electrical contacts to the bottom graphite gate electrode were defined subsequently, in a second step, again using electron-beam lithography, evaporation, and lift-off.

4.5 Transport and optical measurements

To investigate electronic and optical properties of the devices that we have described in the previous sections, we use various experimental approaches and measurement systems that we discuss here.

Transport measurements. All the electrical measurements performed in this thesis were carried out at room temperature and under high vacuum (10^{-6} mbar) in cryostats. Since the investigated devices consist of different layers that are a few nm thick and a few μm in size, they are quite sensitive to electrostatic spikes, ground loops, or other deadly artefacts. The dimensions of the devices as well as the usage of ionic gates dictate the relatively low operating voltages and currents. We use home-built low-noise voltage and current amplifiers in conjunction with DC source-measuring units (Keithley K2400) and digital multimeters (Agilent 3410). The instruments are controlled using the state-of-art Labview programs that allow to run automatic set of complex measurements.

Optical measurements. Photoluminescence measurements in a backscattering geometry (illumination direction out-of-plane) are performed by using an optical microscope to illuminate the device with the incoming laser beam and to collect the resulting emitted light. The light source is a supercontinuum white light laser combined with a contrast filter, allowing to tune the laser wavelength between 400 and 1100 nm. The illumination wavelength for every spectrum is specified in the main text and the laser power kept at 50 μW, if not stated otherwise. All measurements are done with the sample placed in the vacuum chamber with a cryostat mounted on a piezoelectric driven x-y stage allowing positioning precision down to 50 nm (Cryovac KONTI). The laser beam is coupled onto the sample using an optical microscope with long working distance objectives producing a spot of approximately 1 μm in diameter that can be focused anywhere on the sample surface. The light collected from the sample is sent to a Czerny-Turner monochromator with a grating of 150 gr/mm (Andor Shamrock 500i) and detected with a Silicon Charge Coupled Device (CCD) array (Andor Newton 970 EMCCD).

CHAPTER 5

Design of van der Waals interfaces for broad-spectrum optoelectronics

5.1 Introduction

Van der Waals interfaces of interest for optoelectronics consist of two distinct layered semiconductors with a suitable energetic alignment of their conduction and valence bands, such that electron and hole excitations reside in the two separate layers [28, 29, 96, 97]. This allows the interfacial band gap to be controlled by material selection –as well as by application of an electrical bias or strain [34, 98–101]– so that electron-hole recombination across the layers generates photons with frequency determined over a broad range at the design stage. Choosing the interface components among the vast gamut of 2D materials –including semiconducting transition metal dichalcogenides (TMDs, MoS_2, $MoSe_2$, $MoTe_2$, WS_2, WSe_2, ReS_2, ZrS_2, etc.), III-VI compounds (InSe, GaSe), black phosphorous, and even magnetic semiconductors (CrI_3, $CrCl_3$, $CrBr_3$, etc.)– enables, at least in principle, to cover a spectral range from the far infra-red to the violet. In practice, however, efficient light emission from interlayer recombination requires the corresponding electron-hole transition to be direct in reciprocal (k-) space:

The results of this chapter have been published as N. Ubrig et al., "Design of van der waals interfaces for broad-spectrum optoelectronics", Nature Materials **19**, 299–304 (2020) the bottom of the conduction band in one layer has to be centered in k-space at the same position as the top of the valence band in the other layer [43]. This requirement poses severe constraints as concluded from heterostructures of monolayer semiconducting TMDs, the systems that have been so far mostly used to realize light-emitting vdW interfaces [99, 102–105]. Indeed, in this case the minimum of the conduction band and top of valence band are at the K/K' points in the Brillouin zone and the presence of radiative interlayer transitions requires combining compounds with both matched lattice constants and virtually perfect rotational alignment [43, 106]. If not, the k-space mismatch between the K/K' points in the two materials prevents interlayer radiative recombination [35, 105]. To bypass these limitations, it is important to identify a mechanism enabling the occurrence of robust radiative transitions in vdW interfaces, as well as classes of semiconducting 2D materials to implement it.

Here we propose a general strategy to form vdW interfaces of 2D semiconductors supporting interlayer transitions that are direct in k-space, irrespective of the crystal symmetry, lattice constant, or crystallographic alignment of the constituent materials. If the materials forming the interface are selected so that the conduction band minimum in one and the valence band maximum in the other are centered at the Γ-point of reciprocal space, interlayer transitions will be direct in k-space as long as the energetic alignment of the bands is of type II (because the Γ-point resides at $k = 0$, and hence coincides for all materials). To demonstrate this strategy, we use bilayers and thicker multilayers of different TMDs (WS_2, MoS_2, and $MoSe_2$) having the maximum of their valence band at the Γ-point [48], and show that they enable direct interlayer transition in vdW interfaces with InSe multilayers, which have their conduction band minimum at Γ [69, 107]. Light emission from Γ-point interlayer transitions is well known in covalently bonded heterostructures of GaAs/AlGaAs and CdTe/ZnSe [108–112], which form the basis for a multitude of technological applications including light-emitting diodes, different types of lasers, radiation detectors, etc [113–115]. The advantage of vdW interfaces is that the constituent materials neither need to be lattice matched nor satisfy any other stringent conditions, broadening the choice of materials that can be used and, correspondingly, the range of accessible photon frequencies.

5.2 Photoluminescence measurements

We perform photoluminescence (PL) measurements that allow the identification of spectral features in the light emitted by vdW interfaces originating from interlayer electron-hole recombination. The behaviour representative of the systems that we have studied is illustrated in Figs. 5.1 and 5.2, with data measured on structures formed by bilayer InSe (2L-InSe) and bilayer WS_2 (2L-WS_2), assembled to enable separate measurements of the PL coming from the individual layers and from their interface (see Fig. 5.1(a) for a schematic of the 2L-InSe/2L-WS_2 interface and Fig. 5.1(b) for the relevant aspects of the band structure). Lines of different colour in Fig. 5.1(c) represent the PL measured at $T = 5$ K on 2L-WS_2 (blue line), 2L-InSe (orange line), and on their interface (purple line), and can be readily interpreted in terms of the known band structure of the materials forming the interface (see the arrows in Fig. 5.1(b)). The PL spectrum of 2L-WS_2 shows a (split) peak at approximately 2 eV originating from direct recombination of excitons and trions at the K-point, and a lower energy peak at 1.73 eV due to k-indirect recombination of electrons at the Q-point with holes at the Γ-point, as expected [116, 117]. In the 2L-InSe spectrum a peak at approximately 1.9 eV is present, corresponding to the so-called A-transition in this system [107, 118, 119]. The vdW interface PL, in contrast, is dominated by a peak close to 1.55 eV, significantly lower than the energy of the peaks identified in the spectra of the constituent materials, without any pronounced feature corresponding to those of 2L-WS_2 and 2L-InSe. We directly conclude that the interfacial PL cannot be explained in terms of intralayer transitions, and that the 1.55 eV peak originates from an interlayer transition resulting from charge transfer that quenches the PL of the individual layers.

The temperature evolution of the interfacial PL intensity (Fig. 5.2**a**) and its dependence on the excitation laser power (Fig. 5.2**c**) do indeed exhibit the behaviour characteristic of interlayer transitions that are direct in k-space. Fig. 5.2**a** shows that upon reducing T from 250 to 5 K, the intensity of the 1.55 eV PL peak steadily increases, as expected for a transition that is direct in k-space. For comparison, Fig. 5.2**b** shows that in 2L-WS_2 the amplitude of the 2 eV peak originating from k-direct recombination at the K-point also increases upon cooling, whereas the amplitude of the 1.75 eV peak due to the k-indirect transition between the Q and the Γ point decreases, as typical for phonon mediated processes. Upon increasing the excitation laser power, the transition energy increases by more than 50 meV before saturating as the power exceeds 100 μW (see Fig. 5.2**c** and its inset). The blue-shift is a manifestation of the electrostatic potential generated by the “pumped” interlayer excitons, whose density increases (and eventually saturates) at higher excitation power. In simple terms, the photo-generated excitons consist of electrons residing in one layer (InSe) and of holes in the other layer (WS_2), so that a higher exciton density results in a net electrostatic potential difference between the two layers and

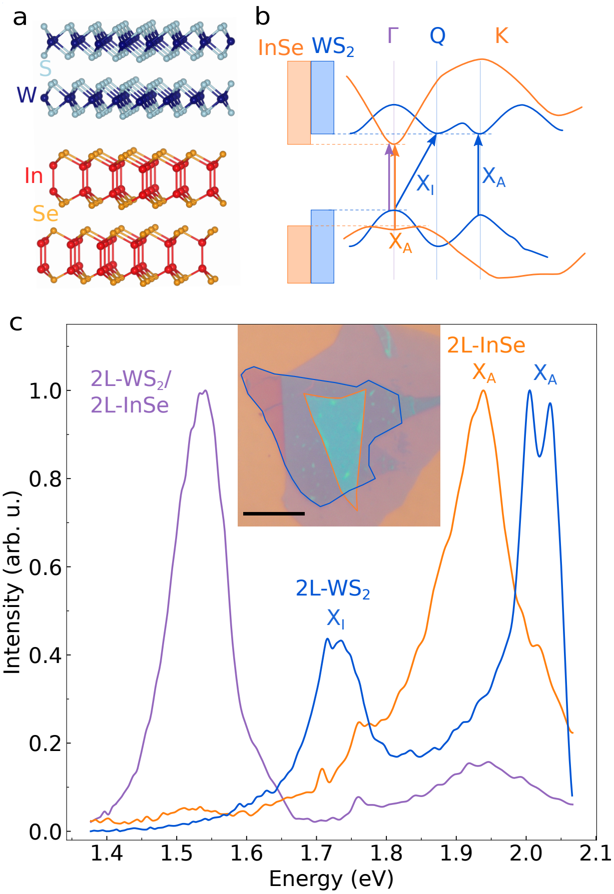

Figure 5.1: Photoluminescence of 2L-InSe/2L-WS$_2$ interfaces. a. Schematics of a 2L-InSe/2L-WS$_2$ interface with the WS$_2$ bilayer on top and the InSe on the bottom. These two systems have a honeycomb lattice structure with lattice constants differing by approximatively 15%. The relevant parts of the band structure of the two layers are shown in **b** (the orange and blue lines represent the conduction and valence band edge of 2L-InSe and of 2L-WS$_2$, respectively). The blue and the orange arrows indicate the transitions observed in the PL of the individual bilayers; the purple arrow represents the interlayer transition from the conduction band of 2L-InSe to the valence band of 2L-WS$_2$ that is observed in the interfacial PL. **c**. Measured photoluminescence spectra of bare 2L-InSe (orange line), bare 2L-WS$_2$ (blue line), and of their interface (purple line). The labels on the PL curves (X_A and X_I) measured on the individual InSe and WS$_2$ bilayers refer to the transitions pointed to by the arrows in panel **b**. Finding that the interfacial PL peaks at an energy smaller than that of all transitions occurring in the individual constituent layers indicates that the interfacial PL originates from an interlayer transition. The inset shows an optical microscope image of a h-BN-encapsulated (hexagonal-Boron Nitride) 2L-InSe/2L-WS$_2$ interface (the scale bar is 10 μm). Orange and blue lines delimit the edge of the InSe and WS$_2$ flakes.

–owing to the interlayer nature of the transition– in a shift of the transition energy (as discussed extensively in the literature –see for instance [120, 121]– this interpretation in terms of an interlayer electrostatic potential difference is fully equivalent to accounting for the effect of the dipole-dipole interaction between the photo-excited excitons). In the same power range, a virtually identical behaviour is observed in PL studies of interlayer excitons in vdW interfaces formed by $MoSe_2$ and WSe_2 monolayers [34, 122, 123], but it is never observed in individual monolayers. We conclude that the transition responsible for the 1.55 eV line in the PL power spectrum of the 2L-InSe/2L-WS_2 interface originates from an interlayer, k-direct transition, as expected for the Γ-Γ transition from the bottom of the conduction band of 2L-InSe to the top of the valence band of 2L-WS_2.

One more direct experimental indication of the origin of the interlayer transition that we observe comes from the analysis of polarization of the emitted light. At the Γ-point, the edge of the InSe conduction band and WS_2 valence band consist of atomic orbitals whose angular momentum component in direction perpendicular to the plane is zero [67, 124]. Theoretically this prescribes [125] that the polarization of the photons emitted in the interlayer transition should be perpendicular to the interface. To check if this expectation is satisfied we fabricated dedicated devices –by cutting into a lamella configuration a block of 2 μm x 20 μm x 0.7 μm out of h-BN encapsulated 2L-WS_2/6L-InSe using a focused ion beam (see Fig. 5.2(d))– and measured the light emitted in the plane of the interface from the side of the lamella. The resulting polarization map is shown in Fig. 5.2(e), with a very pronounced out-of-plane photon polarization, as expected.

On the basis of experimental observations similar to those just presented for 2L-InSe/2L-WS_2 interfaces, we conclude that also all other interfaces that we have investigated, based on combinations of thicker WS_2 and InSe multilayers, exhibit direct interlayer transition at Γ. The same is true for interfaces in which the WS_2 multilayers are substituted by $MoSe_2$, or MoS_2. In all these systems, the PL spectrum of the interfaces exhibits a peak at an energy smaller than that of the spectral features of the individual constituent materials, whose amplitude increases upon cooling and whose frequency blue-shifts upon increasing the power of the exciting laser. The observed behaviour is entirely consistent with the fact that all the semiconducting TMDs employed to assemble the interfaces have their valence band maximum centered at the Γ-point, and the same is true for the conduction band minimum of all the InSe multilayers [34, 120–122]. Interestingly, the PL of the interfaces can be even brighter than that of the individual constituents, showing that interlayer Γ-Γ transitions can result in an increased efficiency for light emission (see Appendix A.3).

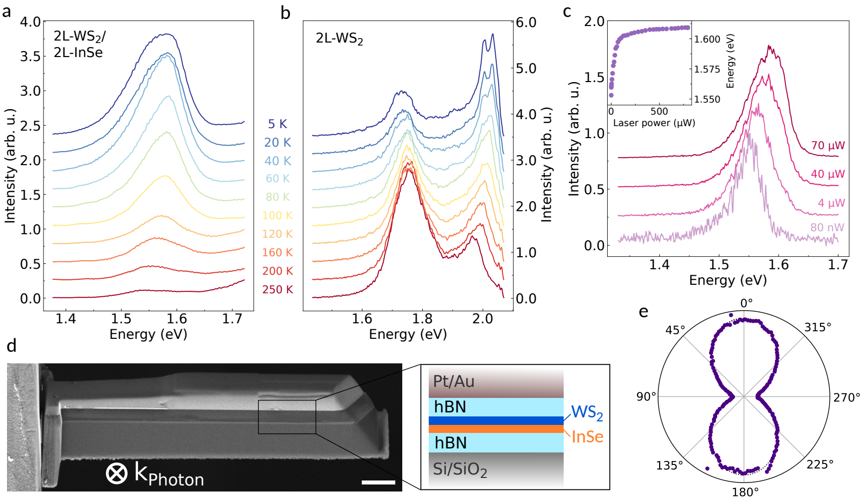

Figure 5.2: Direct interlayer transition in 2L-InSe/2L-WS$_2$ interfaces. a. PL emission spectrum of a 2L-InSe/2L-WS$_2$ interface at different temperatures (curves offset for clarity). Upon lowering T the peak intensity steadily increases as expected for a k-direct optical transition. For comparison, the PL emission spectrum of bare 2L-WS$_2$ is plotted in **b** (curves offset for clarity). It shows that the 2.0 eV peak due to the k-direct transition at the K-point also increases upon cooling, whereas the intensity of the 1.73 eV peak originating from the k-indirect transition (from Q to Γ) decreases as T is lowered. **c**. PL spectra of a 2L-InSe/2L-WS$_2$ interface measured at $T = 5$ K with different laser power (see indicated values; curves offset for clarity). The transition systematically blue-shifts upon increasing power (the full evolution of the peak position is shown in the inset, in the range between 80 nW - 800 μW). **d**. Scanning electron microscope image of a lamella-shaped sample consisting of the layers shown in the right scheme (the interface consists of a 6L-InSe and a 2L-WS$_2$). The lamella structure allows illumination with photons propagating in the plane of the interface, with an electric field polarized normal to the interface plane. The scale bar is 2μm. **e**. Polar plot of the PL of the interface in the lamella configuration, showing that the emitted light is predominantly polarized in the direction perpendicular to the interface (0° corresponds to a polarization perpendicular to the interface plane; the dashed line represents a fit of the data with a sinusoidal dependence).

5.3 Robustness of direct interlayer transitions at Γ in InSe-TMD multilayer interfaces

Figure 5.3 shows representative data reproduced in more than 40 structures that we have investigated experimentally. In Fig. 5.3**a** we show the evolution of the PL spectrum measured at $T = 5$ K on interfaces consisting of 2L-WS_2 and of InSe multilayers of increasing thickness (from 2L to 7L), and in Fig. 5.3**b** we compare the thickness dependence of the interlayer transition energy extracted from Fig. 5.3**a** (purple dots) to the energy of the intralayer transition in the corresponding InSe multilayers (orange dots). As stated above, for all thicknesses the interlayer transition occurs at a lower energy than the intralayer one. A similar behaviour is observed upon fixing the thickness of the InSe layer and varying that of the WS_2 multilayers, as illustrated in Fig. 5.3**c** for interfaces consisting of 4L-InSe and NL-WS_2, with N varying from 2 to 5. Data measured on interfaces based on InSe and semiconducting TMDs other than WS_2 are presented in Fig. 5.3**e**. Fig. 5.3**e** shows the PL originating from interlayer electron-hole recombination in 3L-InSe/2L-$MoSe_2$ and in 4L-InSe/2L-MoS_2: for these materials we did not systematically study the evolution of the interlayer transition energy upon varying thickness, but we did measure several interfaces combining multilayers of different thickness, and observed in all cases PL (again, with an amplitude that increases upon lowering temperature, at an energy that blue-shifts upon increasing excitation laser power). However, for interfaces based on WSe_2 and InSe we did not observe any PL signal, despite the expected presence of a k-direct interlayer transition at the Γ-point. We believe that this is because the transition occurs at an energy of 0.8-0.9 eV, approaching the limit of sensitivity of our detector camera (the presence of a non-radiative recombination path that quenches the PL, *e.g.* due to material-specific impurities creating in-gap states, can not be entirely ruled out at this stage).

We conclude that k-direct interlayer transitions at Γ are robust processes, as we have shown them to occur irrespective of the relative orientation of the multilayers forming the interface (in the majority of cases we did not align the crystals when assembling the structures), of a substantial lattice constant mismatch (approximatively 15 %) between the constituents, and despite the fact that the band structure of TMD multilayers changes significantly upon varying their thickness. Besides substantiating our initial strategy to engineer systems for broad-spectrum optoelectronics, the ability to detect interlayer transitions in so many different interfaces enables the

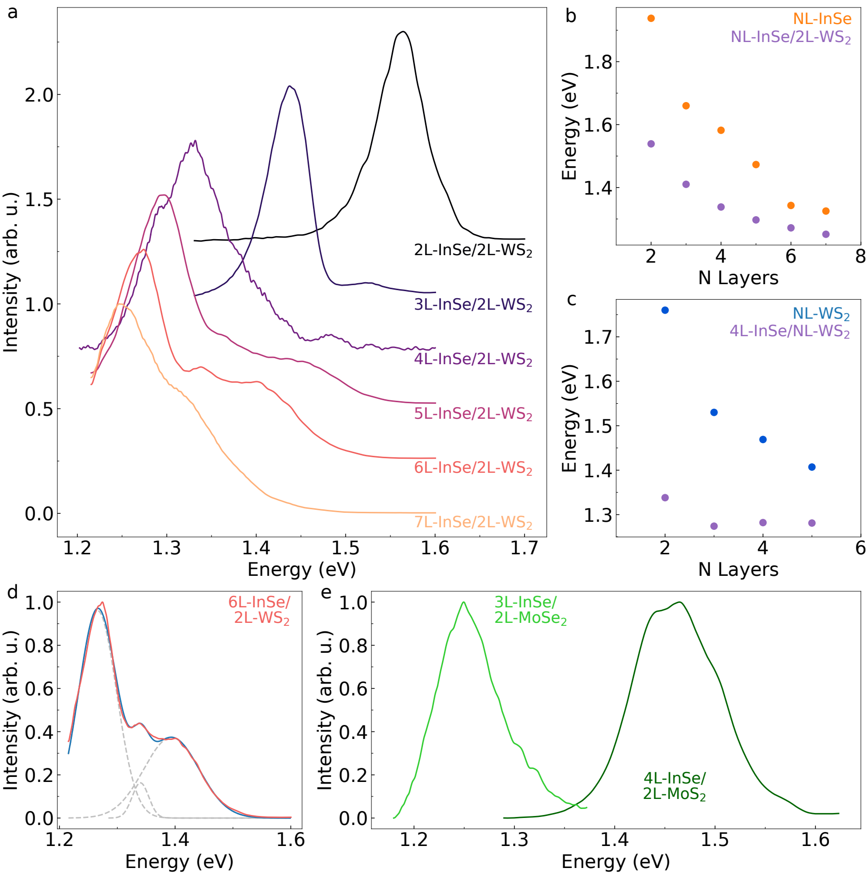

Figure 5.3: Robust k-direct interlayer transitions at Γ in InSe-TMD multilayer interfaces. **a**. PL spectra of NL-InSe/2L-WS$_2$ with N varying between 2 and 7, measured at 5 K (curves are offset for clarity). In all cases a peak originating from a k-direct interlayer transition is observed. **b**. Energy of the interlayer transition at Γ in NL-InSe/2L-WS$_2$ interfaces (purple dots) as a function of N. The interlayer transition always occurs at energy lower than the transitions in the two constituent layers (the orange dots represent the intralayer transition energy in NL-InSe). **c**. Interlayer transition energy in 4L-InSe/NL-WS$_2$ as a function of the number N of WS$_2$ layers (purple dots), extracted from the interfacial PL spectrum (the blue dots represent energy of the intralayer Q-Γ transition in NL-WS$_2$). **d**. Decomposition of the PL spectrum of a 6L-InSe/2L-WS$_2$ interface: the measured data (red solid line) are reproduced (blue solid line) by summing multiple Gaussian lines (gray dashed lines) originating from the interlayer transition, the intralayer transition in 6L-InSe, and from an additional peak that we attribute to the hybridization of states at the valence band edge of 2L-WS$_2$ and NL-InSe (see main text). **e**. PL spectra measured at $T = 5$ K on interfaces realized with TMDs other than WS$_2$ (light green curve: 3L-InSe/2L-MoSe$_2$; dark green curve: 4L-InSe/2L-MoS$_2$). The observed peaks originate from k-direct interlayer transitions at Γ.

relative optical band alignment of entire classes of materials to be determined quantitatively, in a rather straightforward and reproducible way. This is a significant result, because band offsets of semiconductors are often complex to measure precisely, and different techniques give different results depending on details of how experiments are done.

To understand how the alignment of the different band edges is determined, we discuss in detail the procedure for 2L-InSe/2L-WS_2 interfaces, whose relevant band edges are represented in Fig. 5.4**a**. The interlayer transition occurring at 1.55 eV measures the distance in energy between the bottom of the 2L-InSe conduction band and the top of the 2L-WS_2 valence band at the Γ-point. The intralayer transition in 2L-InSe fixes the energy distance between the valence band maximum and the conduction band minimum (both near the Γ-point) in this 2D semiconductor (approximately 1.93 eV). Similarly, the indirect intralayer transition in 2L-WS_2 (approximately 1.73 eV) fixes the position of the bottom of the conduction band in bilayer WS_2 at the Q-point, relative to the maximum of the valence band at Γ. Since in 2L-WS_2 the conduction band edge at the Q and K points are nearly degenerate [126] (the energy difference is at most a few tens of meV, which we neglect here), we can use the k-direct, 2.0 eV intralayer transition at K in 2L-WS_2 to determine the energy of the maximum at K of the valence band of 2L-WS_2. The relative alignment of all relevant band edges in 2L-InSe and 2L-WS_2 is then entirely determined. The same holds true for all other layers that we have investigated: 2L-WS_2 and InSe multilayers up to 7L-InSe (Fig. 5.4**b**), for 4L-InSe and WS_2 of thickness increasing from 2L to 5L (Fig. 5.4**c**), and for 4L-InSe combined with all the different semiconducting TMDs (Fig. 5.4**d**). We estimate the precision of the band-gap values extracted from this procedure to be 100 meV or better. A source of uncertainty comes from neglecting the binding energy of interlayer excitons, which is justified because for all interfaces investigated in our work this quantity is significantly smaller than 100 meV (see Appendix A.4). What also limits the precision of our analysis are the assumption that the conduction band edges at the K and Q points of 2L TMDs are energy degenerate (correct only within a few tens of meV), and having neglected hybridization effects between the valence band edges of InSe and TMD multilayers in which these edges are energetically aligned (based on previous studies of other vdW interfaces reported in the literature [127], we estimate the phenomenon to cause an indetermination of 50 meV or less).

The internal consistency of the band diagrams extracted from the measured interlayer and intralayer transition energies can be cross-checked directly with the measured data. For instance, all measurements on interfaces formed by 2L-WS_2 and NL-InSe shown in Fig. 5.3**a** were performed with the

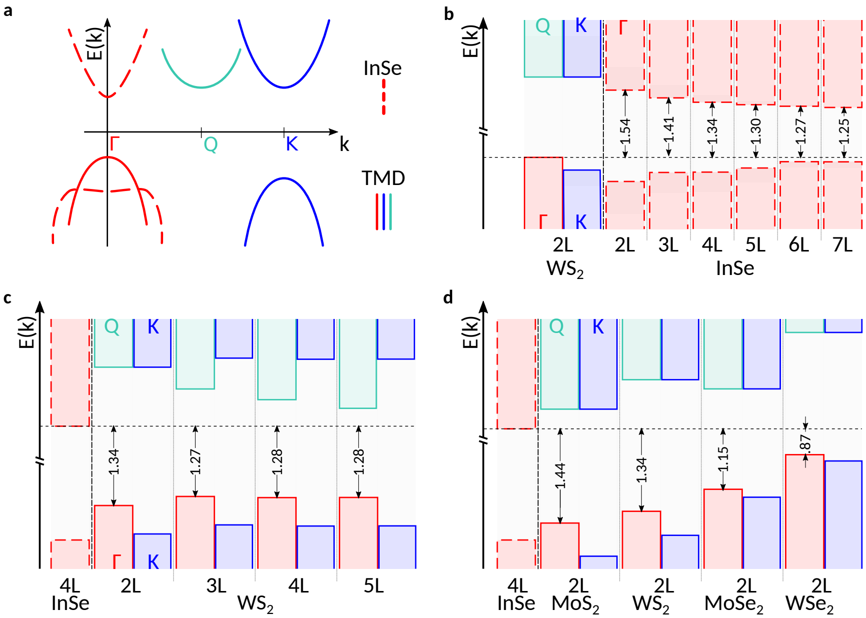

Figure 5.4: Band diagaram of vdW interfaces. **a**. Relevant conduction and valence band edges of interfaces based on multilayers of InSe and semiconducting TMDs. Lines of the same colour and style are used in the other panels of this figure to encode information about material and valleys: red lines indicates states at Γ, blue lines states at K, and green lines states at Q; if the line is continuous, the states belong to the TMD multilayers, if it is dashed to an InSe multilayer. **b**. Band alignment of NL-InSe/2L-WS_2 interfaces, showing that the interfacial band gap of these systems is always formed by conduction band states in the InSe multilayers and valence band states in 2L-WS_2, all centered around Γ. The size of the band gap is indicated in the figure (in eV). **c**. Same as **b** for 4L-InSe/NL-WS_2 interfaces. **d**. Band alignment between 2L-TMDs and 4L-InSe obtained from optical data. For $MoSe_2$ we measured the PL on 3L-InSe/2L-$MoSe_2$ and reconstructed the alignment of 4L-InSe/2L-$MoSe_2$ using the data in **b**, from which are known the relative alignment of the bands in 3L- and 4L-InSe.

excitation laser tuned at the K-K transition of 2L-WS_2. The photo-excited electron at the K-point of the 2L-WS_2 conduction band has always enough energy to be transferred to the InSe multilayer (Fig. 5.4**b**), which is why the interlayer transition in the PL spectrum is visible. For 5L-InSe and thicker layers, in addition, the top of the 2L-WS_2 K-valley becomes nearly degenerate with the top of the valence band of InSe at the Γ-point, so that also the hole in the K-valley of 2L-WS_2 can transfer into InSe. This has measurable consequences, since for 5L- and thicker InSe multilayers it leads to PL originating from the InSe intralayer transition, as well as to splitting of the transitions involving the Γ-point valence band edge (due to hybridization of states in 2L-WS_2 and in InSe). The PL spectra of 5L-, 6L-, and 7L-InSe (Fig. 5.3**a**) do indeed show multiple peaks, one of which is due to the intralayer transition in InSe, and another that we attribute to the hybridization-induced splitting (see Fig. 5.3**d** for the decomposition of the PL spectrum; a systematic discussion of hybridization effects will be presented elsewhere). Additional evidence in support of the band diagrams shown in Fig. 5.4 is obtained from PL energy spectroscopy –i.e., from measurements of the PL intensity as a function of the exciting energy of the photon– that we discuss in Appendix A.1. Finally, note also the different behaviour of the band edges in InSe and WS_2 multilayers (compare Fig. 5.4**b** and 5.4**c**): whereas in InSe both the conduction and valence band edges shift as thickness is increased (Fig. 5.4**b**), in WS_2 the valence band edge remains nearly constant as the thickness is increased past that of bilayers (Fig. 5.4**c**) in agreement with existing Angle-Resolved Photoemission Spectroscopy (ARPES) experiments [127].

5.4 Conclusion and outlook

Besides demonstrating the validity of the proposed strategy for the realization of vdW interfaces supporting k-direct transitions, the band diagrams in Fig. 5.4 show how the interfacial transition energy can be engineered by simply selecting different thicknesses of the most commonly available 2D materials. The heterostructures investigated here densely cover the interval between approximatively 1.0 and 1.6 eV, but a much larger interval can be spanned by employing other known materials. Bilayers or multilayers of $MoTe_2$, and of GaSe, for instance, will allow the energy interval to be extended further on the lower and higher end, respectively. It is this versatility and physical robustness that makes the use of interfacial transitions at the Γ-point ideally suited for the realization of broad spectrum optoelectronic applications. There is broad consensus that optoelectronics is one of the most promising domains for the development of devices based on interfaces of 2D materials, but the large-scale production and commercialization of such devices pose serious challenges as to the required level of material control. This is undoubtedly the case if device operation relies on a very fine control of the different constituents, such as a perfect alignment of 2D crystals, or combining materials with identical crystal lattices and lattice constants. While some of the challenges may be solved in the long term, these requirements are incompatible with virtually all large-area manufacturing techniques that are currently available. The results reported here, however, change the situation, since with an appropriate choice of materials vdW interfaces can be used as radiation sources covering a very broad frequency spectrum, in a mode of operation that is extremely robust against variations of interfacial structural details. This implies that even the simplest possible techniques to assemble large-area interfaces of atomically thin layers –such as liquid phase exfoliation followed by ink-jet printing– can be employed for the scalable fabrication of structures with useful optoelectronic functionality.

CHAPTER 6

Identifying atomically thin crystals with diffusively reflected light

6.1 Introduction

Following the discovery of graphene in 2005 [2, 128], the field of 2D materials has been continuing to develop extremely rapidly in many different directions [3, 18, 29]. Techniques have become available to manipulate atomically thin layers exfoliated from bulk crystals, which can now be stacked on top of each other with the desired orientation to form complex heterostructures [42, 88–92]. The gamut of compounds produced in the form of atomically thin crystals has broadened enormously [10, 15, 129], drastically expanding the scope of physical phenomena that can be accessed in these heterostructures [29, 32–41]. This impressive progress shows no sign of slowing down and a growing effort is devoted to employing systems based on atomically thin layers to realize structures of interest for future technological applications [13, 16, 17, 45].

What has enabled such an exceptionally fast progress in the field of 2D materials –and made the initial discovery of graphene possible– is the use of

---

The results of this chapter have been published as D. Domaretskiy et al., "Identifying atomically thin crystals with diffusively reflected light", 2D Materials **8**, 045016 (2021).

optical microscopes to rapidly detect and locate crystals of many different compounds. The strategy relies on substrates covered with a sequence of layers acting as a Fabry-Pérot cavity –typically a Si wafer covered by a SiO_2 layer, whose thickness is optimized depending on the material to be detected –that enhance the contrast of atomically thin crystals in the visible spectrum [83–87]. For a monolayer of graphene under optimized conditions, an intensity contrast as large as $\approx 5\%$ can be reached, which makes the visualization of the layers straightforward. The thickness of multilayers can also be identified, because the difference in contrast produced by crystals whose thickness differ by an individual monolayer is larger than the *noise* (*i.e.*, of random contrast variations measured on distinct layers of a same thickness).

It seems remarkable that the impressive progress in the field of 2D materials has not led to any substantial change to the way in which the thickness of atomically thin crystals is determined based on optical contrast. This lack of evolution is starting to pose problems for multiple reasons. For many of the atomically thin layers that have been explored more recently, for instance, the optical contrast on commonly used Si/SiO_2 substrates does not provide sufficient sensitivity to determine the thickness unambiguously [81, 130–133]. Also, an increasing number of experiments rely on the use of specific substrate materials, but atomically thin crystals exfoliated on those substrates cannot be detected because their optical contrast is too small, with a notable exception being the use of optical transmission-mode to observe atomically thin crystals on transparent substrates routinely used in the assembly of heterostructures [134]. For these reasons, it is important to explore new ways to enhance the sensitivity for imaging and detecting atomically thin crystals of different materials under different experimental conditions.

With this goal in mind, here we demonstrate a strategy to enhance the optical contrast of 2D materials, which relies on light that is diffusively reflected by substrates with optical inhomogeneous properties (*i.e.*, inhomogeneous refraction index). Exploiting the peculiar polarization properties of the diffusively reflected light, as well as its angular distribution, allows the contrast of atomically thin crystals to be optimized by employing different illumination and detection schemes. In particular, a large enhancement of contrast is found for a cross-polarization detection scheme, *i.e.*, letting the reflected light pass through polarizers oriented perpendicularly to the polarization of the incident light. We additionally reveal an unusually high sensitivity of the optical contrast to the numerical aperture (NA) of the microscope objective, which determines the amount of diffusely reflected light that is collected. We validate the proposed methods by investigating the optical contrast of more than 60 WSe_2m̃ono-, bi-, and trilayers and we reproduce our experimental observations quantitatively by carefully modeling the details of diffusive reflection. We further show that all basic aspects of the technique also work for different 2D materials, such as black phosphorous, InSe, and graphene, indicating the rather broad applicability of the proposed methods. These conclusions are interesting, because the proposed strategy for the detection of atomically thin crystals is based on principles different from those employed in the existing procedure. It may therefore be applied to situations in which the existing procedure does not work, thereby contributing to broadening the scope of fabrication processes of structures based on 2D materials.

6.2 Peculiar sensitivity of the optical contrast

Our work is motivated by the unexpected finding that the optical contrast of atomically thin WSe_2 crystals on a glass-ceramic substrate very strongly depends on details of the imaging conditions, as illustrated in Fig. 6.1A-C. A glass-ceramics is an inhomogeneous material formed by a matrix of different oxides, causing its physical properties to be spatially inhomogeneous. What is important in the present context is that the microstructure of the glass ceramic that we use (LIC-GC, Ohara corparation) [135] causes the refractive index to be inhomogeneous on a scale of 100-200 nm, i.e. a length scale comparable to the wavelength of light in the visible range. Fig. 6.1A shows the image of an atomically thin WSe_2 crystal (containing a bi and a trilayer region) exfoliated on such a glass ceramic substrate, taken using an optical microscope with a high numerical aperture (NA = 0.8) objective to both focus the light from a white source onto the substrate and to collect the reflected light. The reflected light is then recorded into an optical image using a three-channel (Red, Green, Blue) CCD-camera, according to the scheme illustrated in the Fig. 6.1D. This illumination-detection scheme is the one commonly employed to detect exfoliated crystals on Si/SiO_2 substrates, and we refer to it hereafter as *conventional* [136, 137]. Fig. 6.1A shows that the WSe_2 layer is barely visible when imaged in this way, making it impossible to identify the regions of different thickness.

If we polarize the incident light in the s-state, and let the reflected light pass through a polarizer oriented in the perpendicular direction before reaching the CCD camera (as illustrated in Fig. 6.1E), we find that the image contrast is very strongly enhanced (see Fig. 6.1B). Such an enhancement is unexpected, because for the same atomically thin crystal on a Si/SiO_2 substrate, letting the incident and reflected light pass through such a

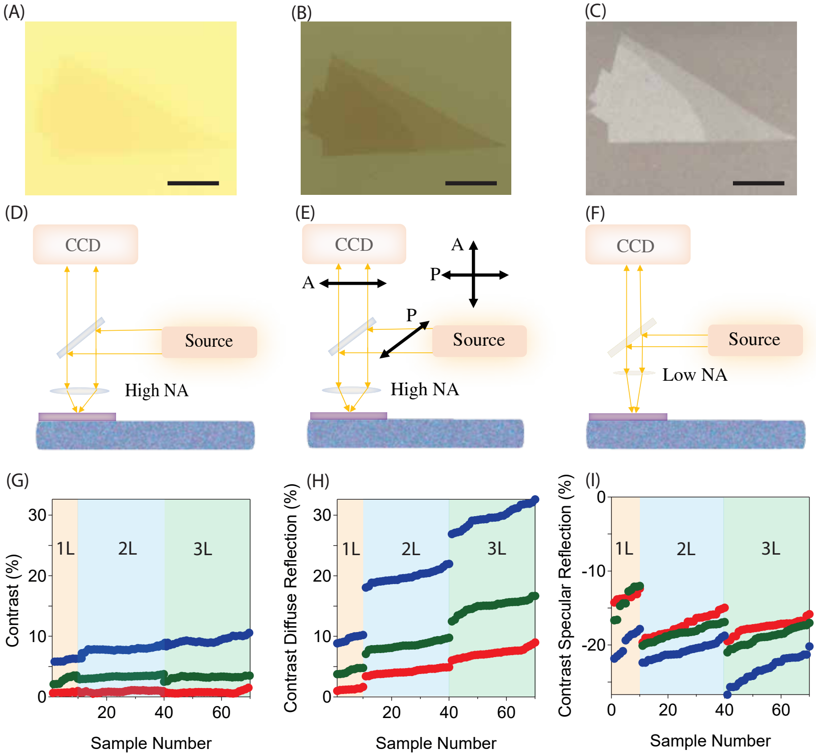

Figure 6.1: Optical contrast of WSe_2 thin layers on glass-ceramic substrates under different illumination-detection conditions: image taken (A) under the *conventional* [136, 137] conditions illustrated in (D). (B) Image taken with the cross-polarization illumination-detection scheme illustrated in (E). Here the incident light is polarized with a polarizer P (s-pol), while the reflected light is analyzed with another perpendicularly oriented polarizer A. (C) Image captured with the illumination-detection with a low numerical aperture objective illustrated in (F). In all images, the scale bar corresponds to 20 μm. The optical contrast of 1L, 2L, 3L WSe_2 (more than 60 different crystals) measured in the three channels (Red, Green, and Blue) of the CCD is shown in (G) for conventional imaging conditions, (H) for the cross-polarization illumination-detection scheme, and in (I) for illumination-detection with a low numerical aperture objective.

configuration of cross polarizers would extinguish the image completely. Instead, on glass ceramic substrates the thin crystals –which look darker than the substrate– are clearly visible and so are the regions of different thickness. Finally, we note that a drastic change in contrast –with the crystal that becomes brighter than the substrate– is observed when we modify the conventional illumination-detection (*i.e.*, without polarizing the incident and reflected light), by simply changing the numerical aperture of the objective from NA=0.8 to NA=0.3 (Fig. 6.1F).

It is clear from Figs. 1 A-C that the observed contrast of an atomically thin crystal on a glass ceramic substrate can be very strongly affected in the absence of any Fabry-Pérot interference, by acting on the polarization of the detected light or on its angular distribution (which is what changing the numerical aperture of the objective does). To quantify the differences between the different illumination-detection schemes we analyze the contrast of more than 60 exfoliated mono, bi, and trilayer (1L-3L) WSe_2. The result of this analysis is illustrated in Fig. 6.1G-I, where we have defined the contrast (in each of the R, G and B channels, and for each illumination-detection scheme employed) as the difference of the intensity measured on the substrate and that measured on the layer, divided by the intensity measured on the substrate. For conventional imaging conditions (Fig. 6.1G), the optical contrast is weak and does not vary significantly upon varying the WSe_2 thickness. The cross-polarisation illumination-detection scheme results in a much higher optical contrast (Fig. 6.1H), exhibiting a clear discretization upon varying the thickness of WSe_2 by one monolayer. As already noted, the contrast changes its sign (Fig. 6.1I) when the low NA = 0.3 objective is used.

6.3 Sensitivity of the contrast to the illumination/detection techniques

The mechanism of this unusual sensitivity to the polarization (and to the numerical aperture of the objective used) originates from light that is diffusively reflected from the glass ceramic substrate, as we now first discuss qualitatively. For homogeneous substrates such as Si/SiO_2 incident light is reflected specularly, according to the usual Fresnel laws of reflection and refraction. On the contrary, the inhomogeneous microstructure of the glass ceramic substrate causes part of the incident light to undergo multiple reflection processes inside the substrate itself, before being eventually reflected with a wide angular distribution (Fig. 6.2A). This process –which is what we refer to as diffusive reflection– occurs in parallel to the conventional specular

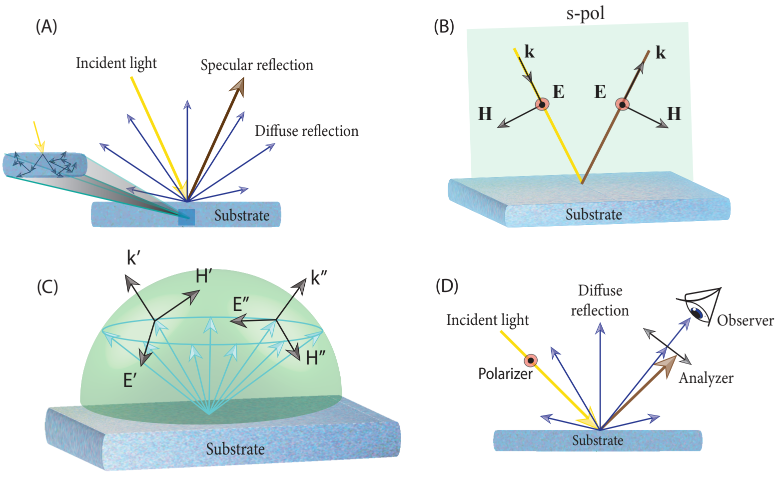

Figure 6.2: Schematic illustration of the different reflection channels and of their polarization properties, exploited in the different detection schemes. (A) Conventional specular reflection (orange arrows) is accompanied by diffusive reflection (blue arrows) originating from the optical inhomogeneity of the substrate, which cause multiple internal reflection and refraction processes (as illustrated in the zoomed-in region). (B) Polarization of the incoming and reflected light in a conventional specular reflection process of an s-polarized beam. (C) Absence of polarisation of the diffusively reflected light, with $\mathbf{k}'$, $\mathbf{k}''$ denoting the wave-vector of different partial waves of the diffusively reflected light, and $\mathbf{E}'$/ $\mathbf{E}''$ and $\mathbf{H}'$/ $\mathbf{H}''$ the corresponding electric and magnetic fields. (D) Specularly reflected light is completely extinguished by the analyzer in the cross-polarization illumination-detection scheme, which allows us to detect only the diffusively reflected non-polarized light from the substrate.

reflection determined by the average refractive index of the substrate. The intensity associated to the two channels –diffusive or specular reflection– is determined by the details of the microstructure in the material. The two reflection channels can be detected separately from each other by using their polarisation and angular distribution properties. Indeed, specularly reflected light is completely extinguished in the cross-polarisation scheme (Fig. 6.1E), because for incident light in the s-polarized state, specularly reflected light always preserves the polarization state (Fig. 6.2B). Diffusively reflected light, instead, has no polarization due to multiple scattering processes on the microstructure (Fig. 6.2C), and therefore half of the intensity of the diffusively reflected light passes through the polarizer on the detection path (Fig. 6.2D). In addition, the use of low numerical aperture objective –which collects light from narrow angles– results in a predominant detection of the specularly reflected light. Indeed, under normal incidence conditions, all specularly reflected light is detected with a low numerical aperture objective, whereas most of the diffusively reflected light –which has a much broader angular distribution– is not. It is such a separation of two reflection channels that is responsible for the drastic differences observed in the images shown in Fig. 6.1A-C.

6.4 Quantitative analysis of the diffuse light

To confirm the scenario just outlined, we perform a quantitative analysis of diffusely reflected light in terms of its angular distribution and polarization properties, which enables us to calculate the intensity of the light detected by the CCD camera mounted on our microscope. Reflections and refractions of light in an inhomogeneous medium, whose refractive index changes randomly from its average value, can be described in terms of scattering cross section per-unit-volume $\sigma\left(\varphi\right)/V$, using an expression developed in the study of the physics of atmosphere (where electromagnetic radiation propagates through mist, clouds, turbulent flows of air, or under other conditions that locally change the refractive index)[138]. This expression reads:

$$\frac{\sigma\left(\varphi\right)}{V} = \frac{2}{\pi}\frac{1}{l}\,\frac{\left(kl\right)^4\cos^2\left[\widetilde{n}^2\varphi + \frac{\pi}{2}\left(\widetilde{n}^2 - 1\right)\right]}{\left[1 + 4\left(kl\right)^2\sin^2\frac{\varphi}{2}\right]^2} \tag{6.1}$$

Here $\widetilde{n}$ quantifies the magnitude of the spatial inhomogeneity of the refractive index, k is the wave-number of the incident light, φ is the angle between the incident and scattered light, and l is a correlation length of the refractive index in the inhomogeneous medium.

To apply Eq. (6.1) to our glass ceramic substrates we take $l = 100$ nm, corresponding to the characteristic size of the crystalline grains in the material. The magnitude of the variation in refractive index is $\widetilde{n} \approx 1$, determined by the refractive indexes of the oxides that compose the material (Li_2O, Al_2O_3, SiO_2, P_2O_5, and TiO_2, see the material specification sheet[135]) and by its microstructure, with TiO_2 particles having $n \approx 2.7$ that are dispersed in a matrix of other oxides having $n \approx 1.6$ (see also our own ellipsometry measurements discussed below). Eq. (6.1) then becomes:

$$\frac{\sigma(\varphi)}{V} = \frac{2}{\pi}\frac{1}{l}\,\frac{(kl)^4\cos^2\varphi}{\left[1+4(kl)^2\sin^2\frac{\varphi}{2}\right]^2} \tag{6.2}$$

This relation describes the angular distribution of the scattered light, that is reflected back towards the microscope objective. Because the electric field of the diffusively reflected light is perpendicular to the direction of propagation, such light has no polarization. Using Eq. (6.2), we can directly compute the total intensity of the diffusive light that we collect with the NA=0.8 objective (a cone with the opening angle of $\sin^{-1}$(NA):

$$I_D = \frac{2\pi}{\frac{1}{2}4\pi r^2} I_0 \int_{\pi-\sin^{-1}(0.8)}^{\pi+\ \sin^{-1}(0.8)} V\frac{2}{\pi}\frac{1}{l}\,\frac{(kl)^4\cos^2\varphi}{\left[1+4(kl)^2\sin^2\frac{\varphi}{2}\right]^2}d\varphi \tag{6.3}$$

where $r = 5$ mm is the focal distance of the objective, I_0 is the intensity of the incoming light. The factor 2π at the numerator results from the integration over the polar angle, and the factor $\frac{1}{2}$ accounts for the fact that only back-scattered light is collected. The scattering volume V is determined as the product of the area of the field of view (a circle of radius 170 μm) and the substrate thickness (150 μm). Eq. (6.3) is the total intensity of diffusively reflected light that reaches the camera; if a polarizer is included in the detection path, as shown in Fig. 6.1E, the intensity is reduced by a factor of 2. Eq. (6.3) gives a quantitative prediction for the reflectance of the diffuse light I_D/I_0 as a function of wavelength, which can be tested experimentally.

To this end, we perform reflectance measurements of diffuse light as a function of wavelength. We use a dedicated glass ceramic substrate that is covered in part with a sputtered 200 nm thick Al film, which acts as a virtually perfect mirror in the entire visible range. Measuring the intensity of the light reflected from the Al layer allows I_0 to be measured, whereas the intensity reflected by the ceramic glass itself – for the same intensity of the source – gives us the value of I_D (see the scheme in Fig. 6.3A). In practice, the Al reference is illuminated with an s-polarized beam of white light

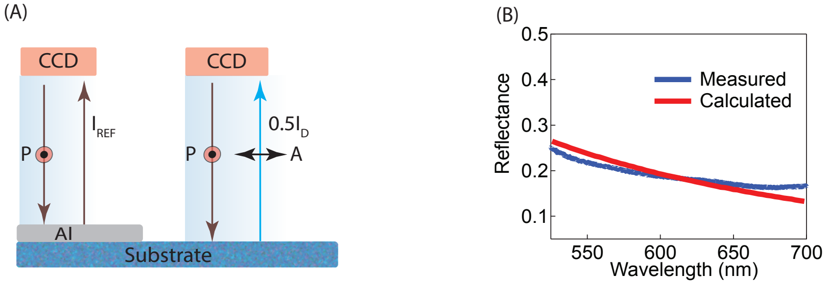

Figure 6.3: Measuring the reflectance of diffusively reflected light. (A) Schematics of the reflectance measurements, in which the intensity of the diffusively reflected light (right) is compared to the intensity of the light reflected from a 200 nm thick layer of Aluminum, which acts as a virtually perfect mirror. The incident light is polarized with a polarizer P (s-pol). The reflected light from the glass-ceramics is analyzed with another perpendicularly oriented polarizer A. (B) Experimentally determined (blue line) and theoretically calculated reflectance spectra of the diffusively reflected light.

focused with a NA = 0.8 objective. The reflected light is collected with the same objective and analyzed with the CCD-camera of a spectrometer. The same illumination procedure is used to illuminate the bare glass-ceramics, but the light diffusively reflected from the glass-ceramics is sent to the spectrometer after passing through a polarizing filter oriented perpendicularly to the polarization direction of the incident light (which fully eliminates the intensity due to the light originating from specular reflection). The ratio of I_D and I_0 measured as a function of wavelength is shown in Fig. 6.3B (blue curve) and compared to the reflectance calculated using Eq. (6.3) (red curve). The excellent quantitative agreement confirms the proposed scenario of diffusively reflected light and validates our quantitative analysis.

6.5 Optical contrast of 2D crystals

Having established that diffuse light originates from the inhomogeneity of the refractive index, we proceed to compute the optical contrast of 2D crystals on a glass-ceramics substrate, to check if we can quantitatively reproduce the observations made in the different illumination-detection schemes (see Fig. 6.1). We describe the diffusively reflected light originating from the multiple reflection and refraction processes caused by the substrate inhomogeneities inside the substrate as a fictitious source of light (also positioned inside the substrate), which emits light with the angular distribution given by $\sigma(\varphi)/V$ (see Eq. (6.2)). The contrast that we detect in the diffusive reflection channel (*i.e.*, what we measure when we insert an analyzer in the

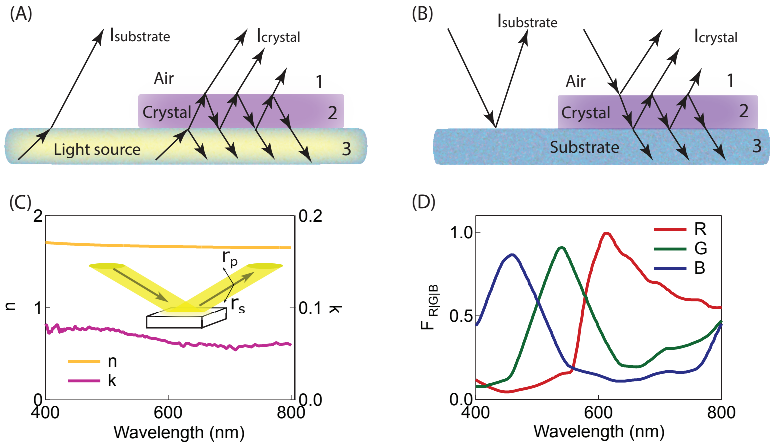

Figure 6.4: Calculation of the optical contrast for the diffusively and specularly reflected light. (A) Schematics of an atomically thin crystal (region 2) placed on a glass-ceramic substrate (region 3) in air (region 1). Calculations assume that the diffusively reflected light can be treated as a light source inside the substrate, emitting with the angular distribution given by Eq. (6.2), as discussed in the main text. The contrast can then be calculated as a transmission problem across the atomically thin crystal. (B) Multiple reflections at the substrate-crystal-air interfaces are considered to calculate the contrast of the specularly reflected part of the incident light. (C) Wavelength-dependent, complex refractive index ($n + ik$) of the glass-ceramics, as obtained from ellipsometry measurements. The inset illustrates the geometry of the measurements, where the ratio of r_p and r_s (Fresnel reflection coefficients for a linearly polarized incident light at the angle of incidence of 72°) is used to obtain n and k. (D) Spectral response functions of our CCD camera in the Red, Green, and Blue channels.

detection path) corresponds then to calculating the transmission of light emitted by this fictitious source in the presence (T_{321}) and absence (T_{31}) of an atomically thin crystal at the surface of the substrate, and can be written as:

$$C_D = \frac{T_{31} - T_{321}}{T_{31}} \tag{6.4}$$

The indexes 1, 2, and 3 indicate respectively air (complex refractive index n_1), an atomically thin crystal (complex refractive index n_2), and the substrate (complex refractive index - n_3; see Fig. 6.4A), so that T_{321} is the transmittance from the substrate to air passing through the atomically thin crystal and T_{31} is the transmittance from substrate to air. For normal incidence, the transmittance from the substrate to air $T_{31} = Re\left\{\frac{n_1}{n_3}\right\}|t_{31}|^2$, where $t_{31} = \frac{2n_3}{n_3+n_1}$ is Fresnel's transmission coefficient. The transmittance of the substrate-thin crystal-air system reads [139, 140] (also for normal incidence):

$$T_{321} = \frac{\frac{n_1}{n_3}|t_{32}|^2|t_{21}|^2\exp\{(-\alpha d)\}}{1-2|r_{32}||r_{21}|\exp\{(-\alpha d)\}+|r_{32}||^2|r_{21}|^2\exp\{(-2\alpha d)\}} \approx \frac{n_1}{n_3}|t_{32}|^2|t_{21}|^2\left[\frac{1}{(1-|r_{32}||r_{21}|)^2}+\frac{(1+|r_{32}||r_{21}|)^3}{(1-|r_{32}||r_{21}|)^2}\alpha d\right] \quad (6.5)$$

Here $r_{ab} = \frac{n_a - n_b}{n_a + n_b}$ denotes Fresnel's reflection coefficient, α is the optical absorbance of the thin flake of thickness d, and we Taylor expand $\exp\{(-\alpha d)\} \approx 1 - \alpha d$ since $\alpha d \ll 1$ for atomically thin layers. We have checked that the Fresnel coefficients in Eq. (6.5) are nearly constant for the incident angles accessible with the NA $= 0.8$ for unpolarized light [140], so that the transmission process does not alter the angular distribution of the emitted light. Eq. (6.5) can then also be used to calculate quantitatively the optical contrast with the microscope objectives used in our experiments.

The contrast that we measure in the specularly reflected channel (*i.e.*, when light is detected with a low numerical aperture objective to cut out most of the incidence angles, and without using a cross-polarization scheme) can be obtained using the usual relation for the contrast:

$$C_S = \frac{R_{13} - R_{123}}{R_{13}} \quad (6.6)$$

where R stands for reflectance and the subscripts have the same meaning as described above for the transmittance. Indeed, specular reflectance of the substrate-air and the substrate-thin crystal-air system (Figs. 6.4B) is a well-known problem that we model with the Fresnel equations for a normal incidence [139, 140], which depends only on the average refractive index (the inhomogeneity of the substrate plays no role). We obtain:

$$R_{123} = \frac{|r_{12}|^2 - 2|r_{12}||r_{23}|\exp\{(-\alpha d)\}+|r_{23}|^2\exp\{(-2\alpha d)\}}{1-2|r_{12}||r_{23}|\exp\{(-\alpha d)\}+|r_{12}|^2|r_{23}|^2\exp\{(-2\alpha d)\}} \approx \left[\frac{(|r_{12}|-|r_{23}|)^2}{(1-|r_{12}||r_{23}|)^2} - \frac{|r_{23}|(|r_{12}|-|r_{23}|)(|r_{12}|^2+1)}{(1-|r_{12}||r_{23}|)^3}\alpha d\right] \quad (6.7)$$

from which R_{13} can be obtained by setting $d = 0$ and substituting the index 2 with 1 in the Eq. (6.7). We have implicitly assumed that the Fresnel reflection coefficient in Eq. (6.7) are the same as those that one would have for a uniform substrate with a refractive index equal to the average value of our (inhomogeneous) substrate. Clearly, this assumption cannot be exact because the diffusively reflected light takes part of the incident power.

However, the excellent agreement that we find with experimental data (see below) shows that our assumption about the Fresnel coefficient corresponds to a good description of the experimental situation. This is probably because the total amount of intensity of the light reflected diffusively is relatively small, so the modification to the Fresnel coefficients is also small.

To determine quantitatively the contrast, we need to know the transmission and reflection coefficients in the Eqs. (6.5) and (6.7), which depend on the complex refractive indexes of the glass-ceramic substrate and of the WSe_2 thin crystals. We obtain the complex refractive index of the substrate by performing wavelength dependent ellipsometry measurements (the geometry of the experiment is presented in the inset of Fig. 6.4C). In these measurements the light spot has a size of approximately 3 mm and probes the average behaviour of the refractive index; the diffusive part of the reflected light can be neglected due to a large distance between the substrate and the detector ($\approx$ 30 cm; due to its broad angular distribution, only a negligible intensity due to diffusively reflected light is detected for such a large distance). The obtained refractive index of the class-ceramics is almost constant ($n \approx 1.65$) for wavelengths in the visible range, with almost no absorption (Fig. 6.4C). The refractive indexes of WSe_2 are taken from literature [141]. As a final step to calculate the measured contrast for the diffusive and the specular reflection channels we need to convolve the wavelength dependent quantities in Eqs. (6.4) and (6.6) with the spectral response $F_R(\lambda)$, $F_G(\lambda)$, $F_B(\lambda)$ of the individual R, G, and B channels of a CCD camera that we use (given by the manufacturer and reproduced in Fig. 6.4D). We obtain:

$$C_{D,R|G|B} = \frac{\int (T_{31}(\lambda) \ - T_{321}(\lambda))F_{R|G|B}(\lambda)\,d\lambda}{\int T_{31}(\lambda)\,F_{R|G|B}(\lambda)\,d\lambda} \tag{6.8}$$

$$C_{S,R|G|B} = \frac{\int (R_{12}(\lambda) \ - R_{123}(\lambda))F_{R|G|B}(\lambda)\,d\lambda}{\int R_{12}(\lambda)\,F_{R|G|B}(\lambda)\,d\lambda} \tag{6.9}$$

Eqs. (6.8) and (6.9) can then be directly compared to the experimental values, as we proceed to do next.

We use the data from the Fig. 6.1E-F to calculate the average values of the contrast in the R, G, and B channels of the CCD camera for 1L-3L WSe_2 crystals imaged under the different illumination-detection schemes. The experimental data obtained in this way are shown together with the theoretically calculated values in Fig. 6.5A and B, from which the excellent agreement between calculated and measured quantities is apparent. The contrast changes nearly linearly as predicted by Eq. (6.5) and (6.7) (with deviations due to the strong dependence of the complex refractive index of WSe_2 on the thickness of the crystal and the wavelength of incident

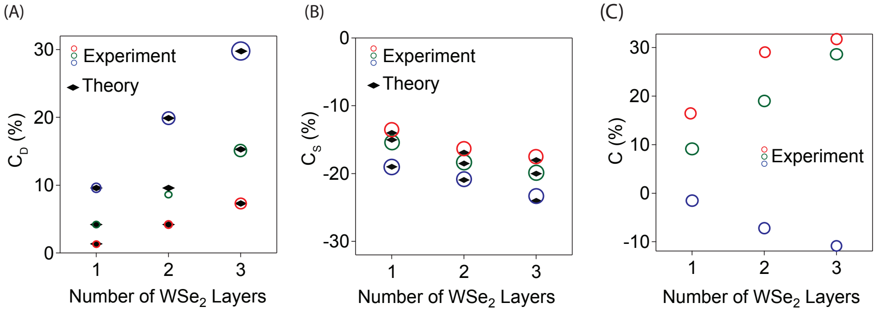

Figure 6.5: Quantitative analysis of the optical contrast of WSe_2 layers in the different illumination/detection schemes. (A) Optical contrast of diffusively reflected light for mono-, bi-, and trilayers on glass ceramic substrates. The experimentally determined values of the contrast for the RGB channels are represented with red, green, and blue empty circles, whose size corresponds to the standard deviation of the contrast measured on many different samples. The theoretical values of the contrast are shown as black full symbols. (B) Optical contrast in the case of specularly reflected light. Symbols have the same meaning explained for (A). (C) Optical contrast of WSe_2 crystals on Si/SiO_2 substrates with a SiO_2 thickness of 275 nm, optimal for detecting a few-layer WSe_2.

light). The sensitivity that we obtain from the contrast measured in the diffusively reflected light channel is as large as –or possibly even better than– the contrast measured for the same crystals on Si/SiO_2 substrates with the conventional illumination-detection scheme, based on Fabry-Pérot interference (see Fig. 6.5C). Indeed, in the diffusively reflected light channel, the contrast allows to discriminate between 1L, 2L, and 3L in each of the individual R, G, and B channels. Overall, the quantitative agreement between the experimental values and the calculated ones fully confirms the relevance of diffusively reflected light and the way in which we have modelled the diffusive reflection process.

For completeness, we also analyze the optical contrast in the case in which light is detected from both diffusive and specular reflection channels, corresponding to imaging in the conventional detection scheme (see Fig. 6.1A and D). The total intensity of the light reflected from the substrate I_{sub} is the sum of intensity of the specularly and diffusively reflected light, respectively $I_{\text{sub,S}}$ and $I_{\text{sub,D}}$ (and the same is true for the light reflected from a thin crystal on the substrate, $I_{crys} = I_{crys,D} + I_{cryst,S}$). From the definition of optical contrast, we have:

$$C = \frac{I_{\text{sub}} - I_{crys}}{I_{\text{sub}}} = \frac{I_{\text{sub,D}}}{I_{\text{sub,D}} + I_{\text{sub,S}}} C_D + \frac{I_{\text{sub,S}}}{I_{\text{sub,D}} + I_{\text{sub,S}}} C_S \tag{6.10}$$

$I_{\text{sub,S}}$ is obtained from Fresnel law using the measured refractive index of the glass ceramic substrate and $I_{\text{sub,D}}$ is known from the reflectance measurements discussed earlier (see Fig. 6.3). As Fig. 6.1A and 1G show that the optical contrast is nearly thickness independent, it is sufficient to analyze its value for the case of bilayer WSe_2 . Using the values of C_D and C_S calculated theoretically (see Fig. 6.5) we find from Eq. (6.5) that in the Red channel C=0.2%, in the Green channel C=2.0%, and in the Blue channel C=9.6%, in very good agreement with the experimental data shown in Fig. 6.1G. The values observed in this conventional imaging mode are the result of the competition between two reflection channels (Eq. (6.10)), which contribute with opposite sign, thereby decreasing the total contrast and explaining the faintness of the crystal as imaged in Fig. 6.1A.

6.6 Versatility of the technique and perspectives

Having established the role of diffusively reflected light and understood the origin of the contrast differences in the different imagining modes that we introduced at the beginning (see Fig. 6.1D-F), we test whether the conclusions obtained for WSe_2 also hold true for other 2D materials. To this end, we look at different families of materials (black phosphorus, InSe, and graphene), and analyze images taken in the conventional imaging mode, with cross polarizers, and with low numerical aperture (see Fig. 6.1) to check if all the key aspects of these different imaging modes are present irrespective of the material considered. We do not repeat the complete quantitative analysis and only focus our attention on layers of the same thickness –4L– for the three materials. Conventional imaging of the crystals on a glass-ceramics results in a weak contrast that does not allow spotting any crystal easily (Fig. 6.6A-C) as in the case of WSe_2(Fig. 6.1 A). Using the cross-polarization illumination-detection scheme, instead, makes all crystals become clearly visible (Fig. 6.6D-F). With this scheme, the crystals look darker than the substrate, just as WSe_2. The resulting positive contrast is approximately 5% per layer for phosphorene and graphene, and 2% per layer for InSe in the Blue channel. Again similarly to the case of WSe_2, the crystals look brighter than the substrate when imaged under the illumination-detection scheme with low NA (Fig. 6.6G-I). The negative contrast then is as high as 6% and 5% per layer for InSe and phosphorene, and 3% per layer for graphene (again, in the Blue channel). Therefore, the technique works for all materials tested and the sensitivity in optical contrast that can be obtained by exploiting diffusively reflected light is at least as large as that given by Fabry-Pérot interference on Si/SiO_2 substrates in the conventional illumination-detection scheme. We therefore conclude that the use of diffusively reflected light in combination with one of the illumination-detection schemes discussed here is a promising alternative to identify many different exfoliated 2D crystals

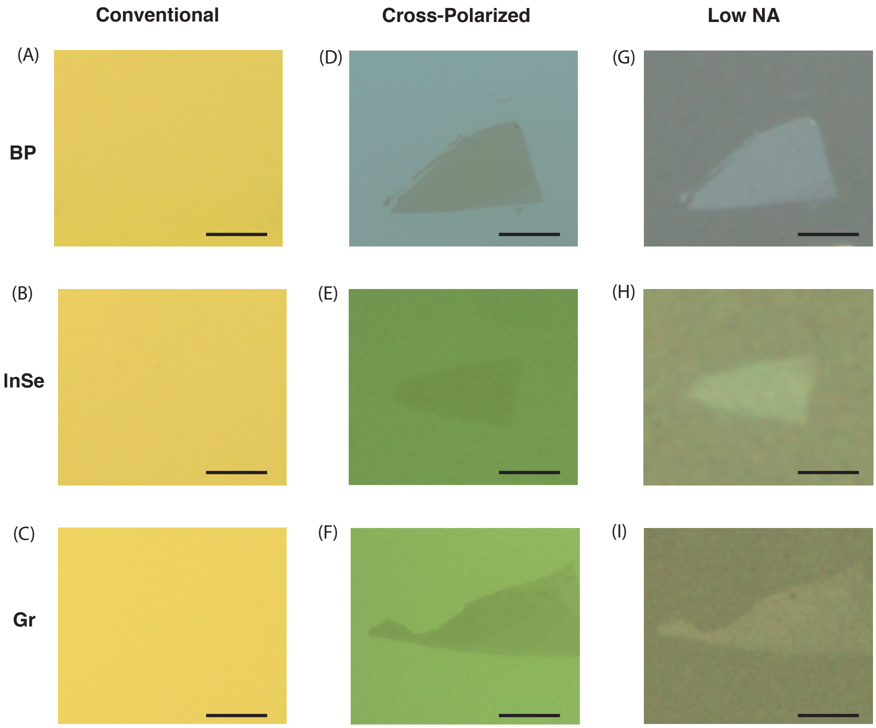

Figure 6.6: Optical contrast of black phosphorus (BP), InSe, and graphene thin layers on glass-ceramic substrates under different illumination-detection conditions. Panels (A) - (C) show images of the different materials taken under conventional illumination and detection conditions, resulting in a virtually vanishing optical contrast. Images in panels (D) - (F) are taken using the cross-polarisation illumination-detection scheme. The atomically thin layers are darker than the substrate (positive contrast) and are easily detected. Panels (G) - (I) show images taken with a low numerical aperture objective, resulting in a negative contrast that also easily allows the detection of the atomically thin crystals. The overall behaviour of black phosphorous, InSe and graphene on a glass-ceramic substrate is therefore identical to that of WSe_2, and can be understood as due to diffusively reflected light from the optically non-uniform glass-ceramic substrate. In all images, the scale bar corresponds to 10 μm.

on a substrate, and determine their thickness.

CHAPTER 7

Quenching the band gap of 2D semiconductors with a perpendicular electric field

7.1 Introduction

An electric field applied perpendicular to the surface of a bulk semiconductor is screened over a finite length, leaving the material interior unaffected. In atomically thin semiconductors [143], however, the small thickness prevents efficient screening, so that a perpendicular electric field uniformly influences the entire system, modifying its band structure [14, 52–55, 144–148]. Indeed, a zero-gap semiconductor such as bilayer graphene can be turned into a gapped insulator using double-gated transistors to apply a perpendicular electric field [14, 54, 55]. Despite representing a true conceptual breakthrough, continuous control of the band structure in transistors has not found widespread use because –as it has become apparent in multiple, recent experiments [145, 147, 149]– the limited maximum electric field that can be applied in common devices does not allow significant changes to be induced in most 2D materials. Here we demonstrate the ability to fully quench band gaps as large as 1.6 eV in WSe_2 bilayers and thicker multilayers, employing a new type of transistors based on double ionic gates that allows the application of electric fields up

---

The results of this chapter have been submitted to Nature Nanotechnology and published as a preprint: D. Domaretskiy et al., "Quenching the band gap of 2D semiconductors with a perpendicular electric field", arXiv:2108.06117 [cond-mat] (2021).

to one order of magnitude larger that the maximum field accessible with conventional double-gated transistors.

7.2 Double ionic gate transistors

Ionic gating relies on electrolytes to transfer the potential from a metallic gate to the surface of a semiconductor [76–78]. In our devices (See **Section 4.4** for details on device fabrication), two electrolytes in contact with two independent gate electrodes are coupled to the same atomically thin semiconductor (see Fig. 7.1**A**). The top electrolyte is a commonly used ionic liquid ($[P14]^+$-$[FAP]^-$) [76–79, 82], and the bottom one is a Li-ion glass ceramic substrate [81, 131] (LASPT [135] purchased from MTI Corp). The atomically thin semiconductor is also connected to two metal electrodes functioning as source and drain contacts, and surrounded by a ground plane (an Aluminum film sandwiched between two Al_2O_3 layers). The ground plane covers the entire substrate, leaving exposed to the ionic liquid only the 2D semiconductor, and eliminates any direct electrostatic coupling of the top and bottom electrolyte. This is important for a proper device operation, because –if the two electrolytes were in direct contact and not decoupled electrostatically– their potential would equilibrate (as it happens in recently realized double-side ionic gated devices [150], with a single ionic liquid in contact with opposite surfaces of a 2D semiconductor), preventing the potential of the bottom (the Li-ion substrate) and of the top (the ionic liquid) electrolyte to be controlled independently. The effectiveness of the electrostatic decoupling can be checked experimentally using two reference electrodes in direct contact with either the Li-ion glass or the top ionic liquid (not shown in Fig. 7.1**A**) as discussed in detail in Appendix B.2. The $Al_2O_3/Al/Al_2O_3$ trilayer also prevents diffusion of Li-ion from the substrate into the ionic liquid that causes degradation of the ionic liquid itself.

As extensively reviewed in the literature [76–79], what makes ionic gate devices effective is their huge gate capacitance ($\approx 50\mu F/cm^2$ [76–78, 80–82]) associated with the electrical double layer that forms at interfaces with metals or semiconductors. It is well established that in single ionic gate devices such a large capacitance allows the accumulation of charge densities unattainable with conventional gating, enabling the observation of new physical phenomena [76, 78, 151–156]. Double-gated devices do not only allow the accumulation of large densities of charge, but also provide independent control of charge density and perpendicular electric field: simultaneously applying a positive voltage V_{IL} to the ionic liquid gate and a negative voltage V_{BG} to the back gate allows an electric field to be established with no net charge accumulated on the semiconductor. Owing to the very large capacitance of the electrical double layer, most of the applied

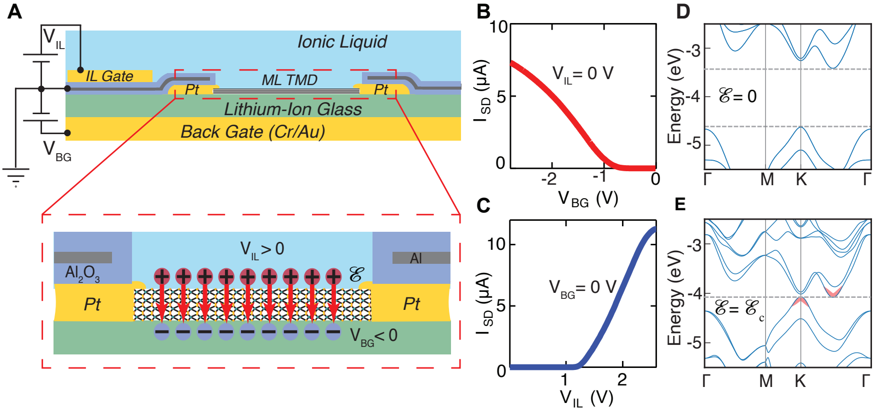

Figure 7.1: Double ionic gated field-effect transistors. A (top panel) Schematic cross-section of a multilayer WSe_2 transistor equipped with top (ionic liquid) and bottom (Li-ion conductive glass ceramic) electrolyte gates. Also shown are the Platinum contacts to the TMD multilayer and a $Al_2O_3/Al/Al_2O_3$ trilayer to decouple electrostatically the top and bottom electrolytes. (bottom panel) Zoom in on the device channel area (not to scale). When the two gates are biased with opposite polarity the charges accumulated on the double layers of the two electrolytes (schematically shown in the figure as red and blue balls) compensate, and a uniform perpendicular electric field $\mathscr{E}$ is established across the TMD (represented by the red arrows in the scheme). **B** Source-drain current I_{SD} measured on a WSe_2 bilayer device, for negative voltages V_{BG} applied to the Li-ion glass gate (with the ionic liquid gate grounded, $V_{IL}=$ 0 V), resulting in the accumulation of holes. **C** I_{SD} measured on the same device as a function of $V_{IL} > 0$ V for $V_{BG} = 0$ V, to cause electron accumulation (the applied source-drain voltage is $V_{SD} = 0.1$ V in **B** and **C**). Note that the application of positive V_{IL} and negative $V_{BG} < 0$ V causes the Li ions to be pulled away from the TMD, ensuring that intercalation does not take place. **D** and **E** represent the band structure of 2L WSe_2 computed within density-functional theory –respectively for zero perpendicular electric $\mathscr{E} = 0$ V/nm, and at the critical field $\mathscr{E} = \mathscr{E}_c$– and show that quenching of the gap with an electric field is expected theoretically (see Appendix B.5 for details; in (**E**), the conduction and valence band edge at $\mathscr{E}_c$ are denoted by red shaded lines).

potential difference falls across the gated material (see **Section 3.5** for a fully detailed analysis), enabling electric fields in excess of 3 V/nm (see below) to be reached in our experiments.

Theory [52, 53], as well as our own calculations (see Fig 7.1**D** and 7.1**E** and Appendix B.5), predict that fields of this strength can quench the band gap of few layer semiconductors. To test this prediction, we employ WSe_2 multilayers belonging to the family of semiconducting transition metal dichalcogenides (TMDs), which we have already employed to realize high quality single ionic gate transistors based on both ionic liquid and on Li-ion glass [44, 81, 82, 157]. It is then crucial to select an appropriate experimental strategy to detect that the band gap closes. All spectroscopic techniques requiring direct access to the material surface –such as tunneling spectroscopy– are excluded because the semiconducting layer is buried in between the two electrolytes used for gating and cannot be accessed. Optical spectroscopy is also not straightforward. A reduction of the gap has been detected in photoluminescence measurements on conventional double gate transistors, confirming that a perpendicular electric field can be used to tune the band gap [145, 149]. In these earlier works the gap was decreased by 10 % or less (because of the small electric field that can be reached in conventional devices), and experiments could be done in the visible/near infrared part of the spectrum. However, to monitor the closure of the gap occurring at much larger electric fields, measurements need to be performed at much lower frequencies, drastically increasing the technical complexity of the experiments and making it nearly impossible to follow the evolution of the gap continuously with a single measurement set-up.

An optimal solution is provided by gate-dependent transport measurements. In single ionic-gate devices, conductivity measurements as a function of gate voltage have been shown to provide spectroscopic capabilities, enabling band gaps of individual 2D semiconductors to be determined quantitatively [79]. In double gated devices, the same technique can be applied to determine the presence or absence of a gap. In simple terms, gate-induced transport can be mediated by electrons –when a positive applied gate voltage is sufficiently large to set the chemical potential in the conduction band– or by holes –when the applied gate voltage is large and negative, and the chemical potential is located in the valence band. The two regimes are separated by an interval of gate voltages in which transport is suppressed by orders of magnitude, corresponding to having the chemical potential located in the gap. To determine whether the gap can be quenched, we can then look at the interval of gate voltages over which transport is suppressed, and see whether we can reduce its extension to zero by applying a sufficiently large perpendicular electric field. This is the strategy that we adopt here.

7.3 Gate-dependent transport measurements

This strategy to determine whether the gap of WSe_2 multilayers can be quenched requires measuring the gate-induced device conductivity as a function of V_{IL} and V_{BG}, and plotting it as a function of $V^\star = V_{IL} + V_{BG}$ (proportional to the potential applied to the semiconductor channel) for different values of $E^\star = V_{IL} - V_{BG}$ (proportional to the applied electric field, see **Section 3.5**). However, since double ionic gate devices have never been realized earlier, it is useful to analyze different aspects of the behaviour of the devices before discussing data plotted in this way.

We start by looking at measurements in which only one of the gate voltages is swept, while keeping the other grounded. In that case, double gate devices function as conventional transistors, as illustrated by the transfer curves (I_{SD} measured as a function of gate voltage) recorded on a WSe_2 bilayer (2L) device (see Fig. 7.1**B** and 7.1**C**, measured with $V_{IL} =$ 0 V and $V_{BG} =$ 0 V, respectively; for additional characterization measurements on this and other devices, see Appendix B.1). These curves are in all regards identical to those measured on single gated devices, including –for instance– the trend of I_{SD} to saturate at large positive V_{IL} observed in Fig. 7.1**C**. In all cases measurements are done by applying a positive voltage to the ionic liquid and a negative voltage to the back gate, since under these conditions Li ions in the glass substrate are pushed away from the semiconducting layer, and cannot intercalate.

We then look at how the transfer curves I_{SD}-vs-V_{IL} of our device evolve for increasing negative V_{BG} values (Fig. 7.2**A**). For $V_{BG} = -0.4$ V, the device transfer curve is qualitatively identical to that measured for $V_{BG} = 0$ V (Fig. 7.1**C**): the current I_{SD} increases as V_{IL} is swept past the threshold for electron accumulation ($V_{IL} = 1.8$ V), and no current flows for $V_{IL} < 1.8$ V, when the chemical potential is in the gap. At $V_{BG} \sim -1$ V, however, the transfer curve exhibits clear qualitative differences, as the current flows even for V_{IL} well below 1.8 V. As V_{BG} is further increased to more negative values, the source-drain current I_{SD} remains large for all values of V_{IL}, without ever vanishing (the square resistance $R_{sq} \sim h/e^2$ for all V_{IL}). Analogous considerations hold true when looking at the evolution of the I_{SD}-vs-V_{BG} transfer curve upon applying a positive voltage V_{IL} to the ionic liquid gate (Fig 7.2**B**).

The complete evolution of I_{SD} as a function of V_{IL} and V_{BG} is illustrated by the colour plot in Fig. 7.2**C**. The measurements are fully reproducible and reversible, as discussed in Appendix B.1; if the gate voltages are swept sufficiently slowly –the typical sweeping rate in our measurements is 5 mV/s– they exhibit negligible or at most small hysteresis originating from bias stress effects. In different measurements, the applied source drain bias was varied between 10 and 100 mV, to keep it smaller or comparable than the thermal energy $\simeq 3.5\ k_BT/e$, without any qualitative influence on the measurements. The observed behaviour is not the one expected if the only effect of the gate voltages was to affect the electrostatic potential in the transistor channel, i.e., the mechanism that determines the operation of a conventional transistor. In that case, both V_{IL} and V_{BG} would just shift the

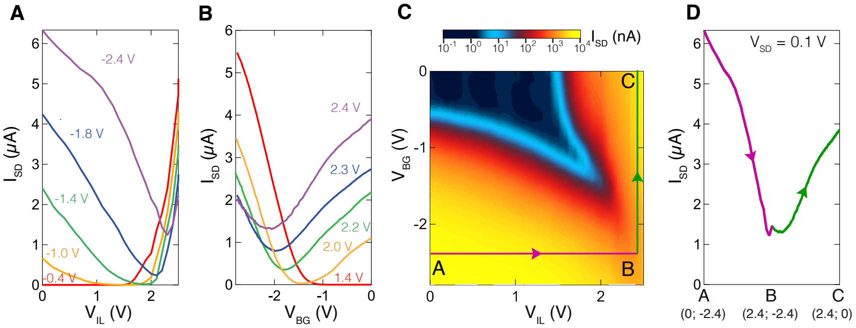

Figure 7.2: Electrical characteristics of a double-gated 2L-WSe$_2$ transistor. **A** Source-drain current I_{SD} measured on a 2L-WSe$_2$ device as a function of ionic liquid gate voltage V_{IL}, for different negative values of back gate voltage V_{BG}. The curves evolve from exhibiting textbook transistor behaviour at small negative V_{BG} (see also Fig. 7.1**B**), to not showing any sizable current suppression at large negative V_{BG}. **B** Same as **A**, with the source-drain current I_{SD} measured as a function of V_{BG} for different positive values of V_{IL}; the evolution of the transistor curves is fully analogous to the one shown in **A**. **C** colour plot of I_{SD} (in logarithmic scale) as a function of V_{BG} and V_{IL}. Note that the simultaneous application of a large negative V_{BG} and of an equally large positive V_{IL} causes the current in the transistor to increase by 4-to-5 orders of magnitude, despite leaving the potential of the transistor channel ($V^{\star} = V_{IL} + V_{BG}$) unchanged. **D** Evolution of I_{SD} along the A-B-C contour illustrated in panel (**D**) (the coordinates of A, B, and C in the (V_{IL}, V_{BG}) plane are indicated at the bottom). Transport in the transistor is mediated by holes at A and by electrons at C: finding that nowhere the current is fully suppressed implies that on part of the A-B-C contour the valence and conduction band of WSe$_2$ must overlap. In all measurements $V_{SD} = 0.1$ V.

energy of the 2L-WSe$_2$ bands, and a change in the voltage applied to one of the gates would only cause a rigid shift in the transfer curve measured as a function of the voltage applied to the other gate. The data, however, do not show a rigid shift. The observed behaviour is also not the one expected in devices in which the two gates are decoupled [158], i.e., in which transport is mediated by two accumulation layers of electrons and holes on opposite surfaces of the bilayer (see the Discussion section).

The reason is that the concomitant application of large positive V_{IL} and large negative V_{BG} also generates a perpendicular electric field that quenches the band gap. To gain further understanding, it is useful to look at the evolution of transport as V_{IL} and V_{BG} are varied continuously along the contour outlined by the coloured line in Fig. 7.2**C**. At point A, $V_{IL} = 0$ V and $V_{BG} = -2.4$ V. The negative potential V_{BG} results in the accumulation of holes (see Fig. 7.1**B**), and sets the chemical potential in the WSe$_2$ valence band (the square resistance is $R_{sq} \sim 15$ kΩ, Fig. 7.2**B**). As V_{IL} is increased from 0 to 2.4 V at fixed $V_{BG} = -2.4$ V, we travel from points A to B (green line), and the electrostatic potential $V^\star$ applied to the channel goes back to zero. Nevertheless, the current remains large. If then V_{BG} is decreased from -2.4 to 0 V at fixed $V_{IL} = 2.4$ V we move from B to C (purple line), where transport is mediated by electrons accumulated by the large positive voltage V_{IL} (see Fig. 7.1**C**). Transport therefore evolves from being mediated by holes at point A (with the chemical potential in the valence band), to being mediated by electrons at point C (with the chemical potential in the conduction band), without ever passing through a highly insulating state (see Fig. 7.2**D**). This is possible because the gap closes and the conduction and valence band overlap in some part of the contour, with electrons and holes coexisting in the transistor channel. Indeed, this happens in the neighborhood of B, where the electric field perpendicular to the 2L-WSe$_2$–proportional to $E^\star$– is maximum.

We now plot the current I_{SD} as a function of $V^\star = V_{IL}+V_{BG}$ and $E^\star = V_{IL} - V_{BG}$ (Fig. 7.3**A**), as originally planned. Fig. 7.3**B** shows I_{SD}-vs-$V^\star$ curves measured at fixed values of $E^\star$. As expected, at small $E^\star$, I_{SD} is finite for sufficiently large negative and positive $V^\star$ –with current mediated by holes and electrons respectively– and vanishes over an extended $V^\star$ interval, as the chemical potential in 2L-WSe$_2$ is swept across the gap (the square resistance in this regime is larger than the sensitivity of our measurements). The $V^\star$ interval with vanishing current shrinks as $E^\star$ increases and for $E^\star > E_c^\star$, no highly resistive state is observed. This signals a transition to a highly conductive state with increasing applied perpendicular electric field, which becomes apparent by looking at the evolution of I_{SD}-vs-$E^\star$ at fixed values of $V^\star$, i.e., by looking at vertical cuts of the colour plot shown in Fig. 7.3**A**. In Fig. 7.3**C** we plot such a cut for $V^\star = 0.5$ V (dashed green line in Fig. 7.3**A**), showing that for sufficiently large values of $E^\star$ (> 3V) I_{SD} increases with increasing $E^\star$ without a change in the electrostatic potential applied to the channel. We conclude that in the presence of a sufficiently large electric field a finite conductivity of order e^2/h is present irrespective of the position of the Fermi level, indicating that states are available at all energies to mediate transport. This implies that no gap is present and that the application of a sufficiently large electric field can fully quench the band gap in a 1 nm thick semiconductor.

To determine $E_c^\star$, we extract the threshold voltages for electron and hole conduction ($V_{T-e}^\star$ and $V_{T-h}^\star$), plot the difference $\delta = V_{T-e}^\star - V_{T-h}^\star$ as a function of $E^\star$, and look at when δ vanishes (Fig. 7.3**D**). The corresponding electric field is then approximately given by $E_c^\star/t_{TMD} \simeq 3.0$ V/nm, where $t_{TMD} = 1.3$ nm is the thickness of 2L-WSe$_2$. This is a slight overestimate, because part of the voltage drops across the screening length of the two electrolytes. However, as we discuss in detail in **Section 3.5**, the very large capacitance of the gate electrolytes ($C \approx 50$ μF/cm^2 [76, 77, 80–82]) ensures that the voltage drop across the electrolytes is small, from which we conclude

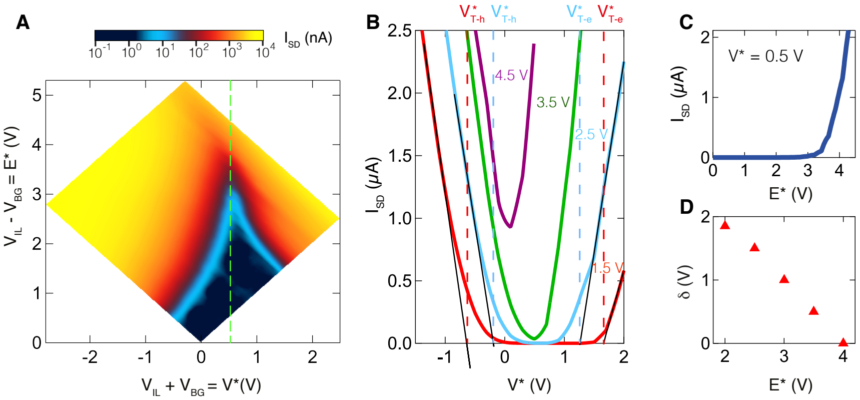

Figure 7.3: Band gap evolution as a function of electric field. A Colour plot of the source-drain current I_{SD} (in logarithmic scale) measured on a WSe$_2$ bilayer device as a function of $V^{\star} = V_{IL} + V_{BG}$, and $E^{\star} = V_{IL} - V_{BG}$ (respectively proportional to the electrostatic potential in the transistor channel and to the electric field perpendicular to the 2L-WSe$_2$ crystal). The width of the $V^{\star}$ interval over which the current I_{SD} is suppressed decreases monotonically upon increasing $E^{\star}$. **B** For a quantitative analysis, we look at horizontal cuts of the colour plot in (**A**), I_{SD}-vs-$V^{\star}$ at fixed $E^{\star}$ (values indicated in the figure). The curve measured at $E^{\star} = 4.5$ V exhibits a complete suppression of I_{SD}, and the black thin lines illustrate how we determine the threshold voltage for electron ($V^{\star}_{T-e}$) and hole ($V^{\star}_{T-h}$) conduction (by extrapolating I_{SD} to zero for positive and negative values of $V^{\star}$; the position of the threshold voltages are marked by the vertical dashed lines). **C** Cut of the colour plot in **A**, taken at fixed $V^{\star} = 0.5$ V, in correspondence of the vertical green dashed line. The data show a transition from a highly resistive state at low $E^{\star}$, to a state with resistivity of order h/e^2 at $E^{\star} > 4$ V. This transition, which occurs at fixed V^{*}, is a direct manifestation of the quenching of the band gap caused by the applied electric field. **D** We plot $\delta = V^{\star}_{T-e} - V^{\star}_{T-h}$ as a function of $E^{\star}$, and find the value $E^{\star}_{c}$ for which $\delta = 0$ V ($E^{\star}_{c} = 4$ V in our 2L-WSe$_2$ device) to determine the condition at which the gap closes.

that the electric field $\mathscr{E}_c$ needed to quench the gap of 2L WSe$_2$ is between 2.5 and 2.7 V/nm (note that this is the actual electric field, and not the displacement field, which is frequently referred to in the literature when analyzing experiments on double-gated transistors). We have performed similar experiments on 3L, 4L, 5L and 7L WSe$_2$ and succeeded in closing the band gap in all cases (see Fig. 7.4 for data measured on devices of different thickness). For some of these devices we have also looked carefully at the evolution of the I_{SD}-vs-V_{SD} curves upon increasing perpendicular electric field, and observed a behaviour confirming that the gap actually closes (see Appendix B.4). The critical electric field $\mathscr{E}_c$ required to close the gap –crosses in Fig. 7.4**G**– decreases upon increasing thickness, with thicker layers requiring a smaller electric field to quench the gap. As we discuss below, this systematic dependence of $\mathscr{E}_c$ on thickness matches quantitatively

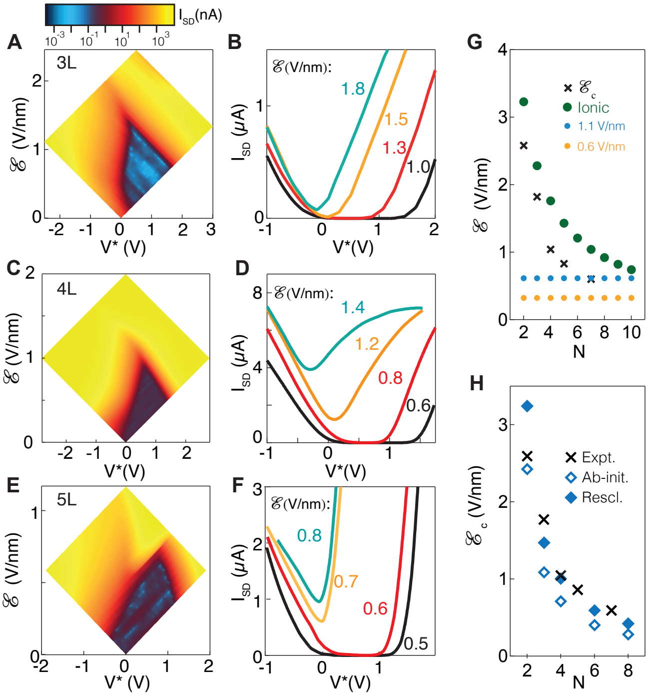

Figure 7.4: Quenching the gap in 3L, 4L and 5L WSe_2 devices. **A**,**C** and **E** show colour plots of I_{SD} as a function of V^* and $\mathscr{E}$ for 3L, 4L, and 5L devices. **B**,**D**,**F** show the corresponding cuts (I_{SD}-vs-V^*), for different fixed values of electric field $\mathscr{E}$ across each WSe_2 multilayer. **G** Comparison between the maximum electric fields that can be applied across WSe_2 N-layers, using different type of devices. Green dots: field achieved in ionic gated devices for $V_{IL} - V_{BG} = 5$ V (larger values are possible, as we repeatedly reached values between 5.5 and 6 V); blue and orange dots: maximum field reachable with hBN-based devices assuming a breakdown field of 1.1 V/nm and 0.6 V/nm, respectively (1.1 V/nm is the ultimate limit reached in ultra-thin hBN; 0.6 V/nm is a more realistic estimate for common hBN). For bilayer WSe_2, the electric field reachable with ionic gating is nearly one order of magnitude larger than the field accessible in hBN-based devices. The dark crosses are the field needed to close the gap, as extracted from our measurements: for all thicknesses investigated in our work, it would have not been possible to close the gap with hBN-based devices. **H** Comparison between the critical electric fields $\mathscr{E}_c$ extracted from experiments (dark crosses) and the corresponding theoretical values obtained from first principles calculations (empty diamonds). *Ab-initio* calculations slightly underestimate the gap, resulting in a small underestimate of $\mathscr{E}_c$. To take this into account, the full diamonds show the value of the critical electric field obtained using the ratio between the known and the calculated gap to rescale $\mathscr{E}_c$ (see Appendix B.5). The agreement with experiments is excellent.

theoretical predictions based on ab-initio calculations, showing that these calculations provide the correct scenario to interpret our experiments.

Note that earlier studies [159, 160] have reported a metallic state originating from a structural transition of $MoTe_2$ from the 2H structure to the so-called 1T' structure (or a variant of it), resulting from either gate-induced charge accumulation [159] or from the application of an electric field [160] in different device geometries. In both cases, the structural transition was accompanied by a very large hysteresis: upon reducing the accumulated charge density or the applied electric field, the system remained in the highly conducting state (which can be understood, since structural transitions of the type invoked are typically of first order). This is not what is seen in our data: neither a discontinuous transition nor any sizable hysteresis in conductivity is observed in the measurements (see Appendix B.3). We can therefore exclude a structural effect as the origin of the observed band closing.

7.4 Discussion

The experimental results show that in the presence of a sufficiently large perpendicular electric field, the atomically thin WSe_2 multilayers that we have investigated remain conducting, with a conductivity close to (or –depending on thickness– larger than) e^2/h, irrespective of the position of the chemical potential (which is controlled by $V^\star = V_{IL}+V_{BG}$). This observation directly indicates that at sufficiently large applied electric field a finite density of states is present at all energies, i.e. that the gap closes. Because the multilayers are only a few atom thick, a fully quantum mechanical calculation is needed to understand how the gap closes and the evolution of the electronic states upon increasing the perpendicular electric field. In simple qualitative terms, however, in the presence of a sufficiently large perpendicular electric field the gap closes because the electrostatic potential lifts the energy of the valence band edge at one crystal surface above the conduction band edge at the opposite surface. The conduction and valence bands then overlap, and the system becomes gapless.

In view of the simple qualitative explanation that we have just given, one may wonder whether the closing of the gap and the gate dependence of the conductivity that we observe is not simply due to the formation of two decoupled accumulation layers –one of electrons and one of holes– at the opposite multilayer surfaces. The formation of two virtually decoupled accumulation layers is what happens for macroscopically thick crystals [158].

Here, we illustrate that the behaviour observed in our atomically thin devices is qualitatively different from that expected in very thick devices, thereby providing additional evidence that the physics of atomically thin double gated devices cannot be accounted for in terms of two decoupled accumulation layers. To this end, we compare the electrical characteristics measured in thin double gated devices with the simulated electrical characteristics of double gated devices with electrostatically decoupled surfaces, and show clear differences in the behaviour. To further substantiate this conclusion, we also discuss data taken on a double gated device realized using a very thick (70 nm) WSe_2 exfoliated crystal, and show that in that case the source-drain current as a function of both gate voltage $I_{SD}(V_{BG}, V_{IL})$ does behave as expected for two decoupled accumulation layers. Having said this we emphasize again that there is no sharp transition from one regime to the other and that different physical phenomena associated to different length scales –wavefunction overlap, screening length, and other effects– can influence the results of the measurements in a way that changes continuously upon increasing the thickness of exfoliated layers.

Fig. 7.5**A-C** show the simulated electrical characteristics of a double gated transistor in which the top and bottom surfaces are decoupled. In this regime of electrostatically decoupled accumulation layers, it is simple to model the basic aspects of the gate dependence of the source-drain current, since the total current is given by the sum of the currents on the two surfaces, each of which only depends on only one gate voltage (that of the nearby ionic gate), i.e., $I_{SD} = I(V_{IL}) + I(V_{BG})$. For comparison with our experimental results in the calculations we have set parameters that resemble those of our devices (even though the precise value of the parameters is immaterial, because our comparison will focus solely on qualitative aspects). We have used as capacitance values for both ionic gates $C_G = 50\ \mu\text{F/cm}^2$, and we have selected electron and hole mobility values in line with those measured in earlier experiments on ionic gated WSe_2 FETs. The top gate (V_{IL}) is assumed to accumulate electrons above a threshold voltage of $V_{Th} = 1.5$ V and the bottom gate (V_{BG}) accumulates holes for negative values, below a threshold voltage of $V_{Th} = -1$ V.

To start the analysis we discuss Fig. 7.5**A**, which shows the dependence of $I_{SD} = I(V_{IL}) + I(V_{BG})$ on V_{IL}, for different fixed values of V_{BG}. In the absence of coupling between the two gates, the bottom gate does not shift the threshold for electron accumulation and its only effect is to offset the $I_{SD}(V_{IL})$ curve. The same is true if we plot I_{SD} as a function of $I(V_{BG})$ for different (fixed) values of V_{IL}: changing V_{IL} only generates an offset, without changing the shape of the curve (see Fig. 7.5**B**). The colour plot of I_{SD} as a function of V_{IL} and V_{BG} is shown in Fig. 7.5**C**. Clearly, since there is no cross coupling between the two gates, threshold for electron and hole conduction occurs for fixed values of V_{IL} and V_{BG}, respectively (i.e., the thresholds manifest themselves as a vertical and a horizontal line in the colour plot of I_{SD}).

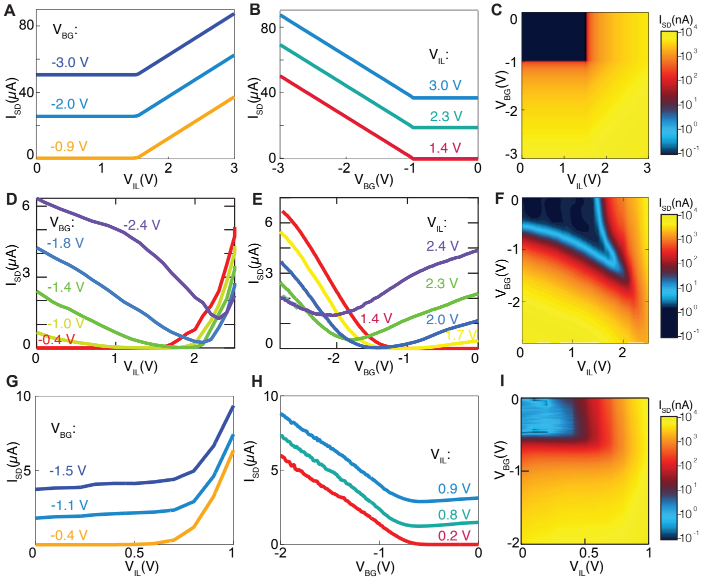

Figure 7.5: A-C Simulated electrical characteristics of a double gated transistor with decoupled electron and hole accumulation layers on top and bottom surfaces. **A** Source-drain current $I_{SD} = I(V_{IL}) + I(V_{BG})$ as a function of top gate voltage V_{IL} for different (fixed) negative values of back gate voltage V_{BG}. The application of a back gate voltage does not modify the threshold for electron accumulation only leading to the increase of the offset current. The same can be seen in **B**, which shows the dependence of I_{SD} on V_{BG} for different positive values of V_{IL}. **C** colour plot of the simulated I_{SD} as a function of V_{BG} and V_{IL}. The absence of coupling between the two gates results in the absence of any shift of the threshold voltage for electron and hole accumulations, resulting in vertical and horizontal lines that limit the region where conduction is suppressed. **D-F** Electrical characteristics of the 2L WSe_2 double-ionic gated FET discussed in the main text (the data are the same as in Fig. 7.2). **D**, **E** and **F** show the same type of measurements as **A**, **B** and **C**, respectively. A direct comparison between the corresponding panels shows that the electrical characteristics of our double ionic gated FETs based on atomically thin WSe_2 multilayers cannot be explained by the presence of two decoupled electron and hole accumulation layers. In our devices the application of a fixed V_{BG} (V_{IL}) not only shifts the electron (hole) threshold voltage but also changes the shape of the curve, which develop a non-monotonic behaviour characteristic of semimetals. The shift of electron and hole voltage –absent in **A**, **B** and **C**– is also apparent in **F**. **G**, **H** and **I** show experimental electrical charachteristics of a double-ionic gated 70 nm thick WSe_2 transistor. The behaviour of I_{SD} as a function of V_{IL} and V_{BG} is in line with the simulated electrical characteristics of a double-gated transistor in which an electron and hole accumulation layer exists on opposite surfaces, as shown by the comparison with the results of the simulations plotted in **A-C**.

All these qualitative features are distinct from the ones observed in the measurements shown in Fig. 7.5**D-F**, which we reproduce from Fig. 7.2. It is clearly apparent that shifting the voltage applied to one of the gates changes the shape of the source-drain current I_{SD} measured as a function of the voltage applied to the other gate, and it does not only generate an offset. This difference in behaviour is easily appreciated by comparing Fig. 7.5**A**,**B** to Fig. 7.5**D**,**F**. For sufficiently large V_{BG}, $I(V_{IL})$ exhibits a non-monotonic behaviour characteristic of semimetal containing both electrons and holes (see Fig. 7.5**D**, and similarly Fig. 7.5**E** for data taken at fixed V_{IL}, as a function of V_{BG}), which is absent for devices in which the two gates are decoupled. Also, in the colour plot of Fig. 7.5**F**, it is apparent that in the experimental data, the threshold in V_{IL} for electron conduction shifts by a large amount upon changing V_{BG} (and the same is true for the threshold in V_{BG} for hole conduction upon changing V_{IL}). All these observations show clearly that in thin double gated devices there is a strong coupling between the effect of the two gates. They also show that it is not possible to reproduce the experimental data, by modelling the WSe_2 mutilayers that we have studied in terms of two decoupled electron and hole accumulation layers on opposite surfaces.

For completeness, in Fig. 7.5**G**, **H** and **I** we show the results of double-ionic gated measurements performed on a 70 nm thick WSe_2 crystal (very similar curves have been recently reported for double gated experiments performed on a 57 nm thick MoS_2 crystal, using h-BN crystals as gate dielectrics [158]). As can be seen by the direct comparison of Fig. 7.5**A**, **B** and **C** with Fig. 7.5**G**, **H** and **I**, respectively, the qualitative behaviour of thick devices resembles the one expected in the presence of two electrostatically decoupled layers, and it is distinctly different from the behaviour observed in our thin double-ionic gated devices (see Fig. 7.5 **D-F**). In particular for the devices realized on the 70 nm thick WSe_2 layer, the threshold as a function of one of the two gate voltages (V_{IL} or V_{BG}) does not change when the voltage applied to the other gate is changed. Also the shape of the curve measured $I_{SD}(V_{IL})$ at fixed V_{BG} does not change when the value of V_{BG} changes, as the curve is only shifted rigidly (similar considerations hold true for $I_{SD}(V_{BG})$ upon changing V_{IL}).

These observations further substantiate that the experimental results presented –namely the gate dependence of the source-drain current from which we conclude that a perpendicular electric field quenches the gap of a semiconductor– cannot be explained in terms of two decoupled electron and hole accumulation layers. That is because, for atomically thin multilayers such as the ones that we study here (and certainly for 2L and 3L WSe_2), the extension of the electron and hole wavefunction is larger than the multilayer thickness, so that the two surfaces overlap in real space and are electronically coupled. Indeed, the extension of the wavefunction is governed by the electrostatic screening length that near charge neutrality (when the two gate voltages are equal and opposite) is longer than the multilayer thickness, because the electron and hole density is small (note that in double gated devices for fields across the multilayers $\mathscr{E}$ close to $\mathscr{E}_c$ the perpendicular electric field is large and the carrier density small, because electric field and density are controlled independently; such a regime of large field and small charge density cannot occur in single gated devices, in which a large electric field is necessarily accompanied by a large charge density). In these atomically thin multilayers, therefore, the electric field is large enough to bring spatially overlapping conduction and valence band states to the same energy, causing a drastic modification of the multilayer band structure. This is indeed what is predicted by *ab-initio* calculations, which show that at large electric field the gap closes as the minimum of the conduction band at the Q-point in the Brillouin zone touches the top of the valence band at the K-point (see Fig. 7.1**E**). We have extracted from these calculations the full thickness dependence of the critical electric field $\mathscr{E}_c$ needed to quench the gap and found excellent quantitative agreement with the values of $\mathscr{E}_c$ measured experimentally (see Fig. 7.4**H**). As we stated above, this agreement provides strong support for our interpretation.

The outlined mechanism for closing the gap in atomically thin multilayers provides a basic physical scenario for the nature of the resulting gapless electronic state. At charge neutrality and for applied electric fields $\mathscr{E} > \mathscr{E}_c$ the system is a compensated semimetal with a finite band overlap that increases with increasing $\mathscr{E}$, and with electron and hole states coexisting at the Fermi level. The semimetal intrinsically has broken inversion symmetry, owing to the large electric field present. It is uniform in the plane of the multilayer, but the "center of mass" of electrons and holes are displaced relative to each other in the direction perpendicular to the layers. As the electric field is increased further, the electron and hole states are pushed away from each other due both to the increasing potential difference between the two surfaces and to the fact that –as the density of electrons and holes increases– the screening length may eventually become shorter than the thickness. At that point, the system will effectively consist of electron and hole accumulation layers that are coupled only by Coulomb attraction. For the thinnest multilayers, such as 2L and 3L WSe_2, however, the thickness is so small that full overlap of the electron and hole wavefunctions is expected to remain relevant even at the largest experimentally accessible densities.

7.5 Conclusion and outlook

An investigation of the transport properties of atomically thin WSe_2 multilayers as a function of electron and hole density and temperature will be needed to explore all properties of the system as a function of applied electric field. Similarly, investigating the optical properties for $\mathscr{E} > \mathscr{E}_c$ (i.e., before the gap closes) will be essential to determine how the applied electric field modifies the semiconducting properties of these atomically thin multilayers. These studies go beyond this first exploration, whose goal is to establish experimentally the ability to quench a semiconducting band gap larger than 1.6 eV in 2D semiconductors as thin as a WSe_2 bilayer (i.e., just over 1 nm thick). That this is possible at all was far from obvious at the start, because the field needed to quench the gap in 2L WSe_2 is close to 3 V/nm, whereas the largest breakdown field of solid state dielectrics is approximately 1 V/nm [74]. Indeed, demonstrating that electric fields as large as 3 V/nm can be controllably and reversibly applied onto a 2D material is a key result of our work. Many theoretical studies have been made, predicting that the electronic properties of a variety of atomically thin crystals can be drastically altered if field of this strength can be reached in the experiments. Examples include topological transitions in transition metal dichalcogenides [56–58] and other 2D materials [59], the ability to switch the magnetic anisotropy [161] or the topological charge of magnetic excitations [60], and the control of the electronic state and other properties of different van der Waals materials and their heterostructures [61–63]. So far however, these theoretical predictions were considered to be exclusively of academic interest, because the required electric fields were nearly one order of magnitude larger than those reachable in practice. The results that we show here change the situation and open a large field of new possibilities, as they allow exploring a vast gamut of new electronic phenomena.

APPENDIX A

A.1 Photoluminescence excitation spectroscopy (PLE)

Photoluminescence excitation spectroscopy (PLE) measurements have been performed on several of the samples presented in the main text, to gain insight on the nature of the dynamics of the photogenerated electron and hole pairs prior to their radiative recombination. The results of the measurements are consistent with the band diagrams discussed in Fig. 5.4 of the main text, and support our interpretation of the observed interfacial photoluminescence as due to interlayer transitions at Γ.

The behaviour representative of the interfaces that we have studied is illustrated in Fig. A.1 with data measured on an interface formed by 2L-InSe and 2L-WS$_2$. In the experiments we record the spectrum of the photoluminescence signal in the interface region (in this case in the spectral region around 1.6 eV, corresponding to the interlayer transition as discussed in the main text (see Fig. 5.1(c)), while varying the laser excitation energy at constant power. The measured intensity of the PL signal plotted as function of the emitted photon energy and of laser excitation energy is shown in Fig. A.1**a** (see also Fig. A.1**b**). The intensity of the interfacial PL signal exhibits pronounced maxima when the excitation laser energy is approximately 2 and 2.5 eV, corresponding respectively to the resonant excitation of the A-exciton and B-exciton at the K-point of 2L-WS$_2$. This directly shows that the electron and hole generated from the excitation laser

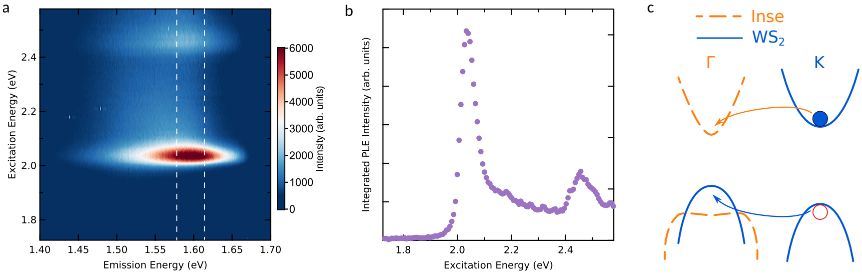

Figure A.1: **a**. colour plot of the PL intensity measured at $T = 5$ K on a 2L-InSe/2L-WS_2 interface, as a function of emitted photon energy (x-axis) and excitation energy of the laser (y-axis). The interface emits at energies close to 1.6 eV. For that energy the PL exhibits two peaks as a function of energy of the excitation laser, at 2.0 eV and 2.5 eV, resulting from the resonant excitation of respectively the A- and the B-exciton at the K-point of 2L-WS_2. The phenomenon is illustrated also in panel **b**, where the PL intensity –integrated over the energy interval delimited by the vertical dashed lines in a– is plotted as a function of excitation laser energy. **c**. Schematics of the relevant parts of the band structure of 2L-InSe/2L-WS_2 illustrating the charge transfer process leading to the measured PL. The photo-excited electrons and holes at the K-point of WS_2 reach the Γ-point (the electron is transferred into InSe, whereas the hole remains in WS_2) where eventually they recombine through a radiative interlayer transition.

initially reside in 2L-WS_2. Only in a subsequent stage, the electron and holes relax to the lowest energy states available. According to the band alignment discussed in the main text –shown again in Fig. A.1**c** for convenience– the lowest energy configuration corresponds to having the electron occupying a state at the minimum of the conduction band in InSe, with the hole residing at the maximum of the valence band of 2L-WS_2. As both these states are located at Γ, it is possible for the electron to recombine radiatively with the hole, through an interlayer transition that is direct in k-space. The PLE data presented here therefore show that all steps from photon absorption to photon emission are consistent both with the band diagram of the interface discussed in the main text (see Fig. 5.4**b** and Fig. A.1**c**) and with what is known about the properties of the individual layers (*e.g.* about the details of resonant absorption at the K-point of 2L-WS_2). We have further performed PLE experiments on the lamella sample discussed in the main text (see Fig. 5.2**d**). In Fig. A.2 we show the PL emitted from a 6L-InSe/2L-WS_2 interface centered around 1.3 eV, as a function of energy of the excitation laser, for two orthogonal linear polarizations of the laser beam (respectively parallel and perpendicular to the basal plane). A clear difference in the signal is observed only for excitation energies close to 1.6 eV, i.e. in the spectral region corresponding to intralayer absorption in InSe. Indeed, only when the polarization of the exciting laser is perpendicular to the plane, absorption due to an InSe intralayer transition occurs. Electrons and holes

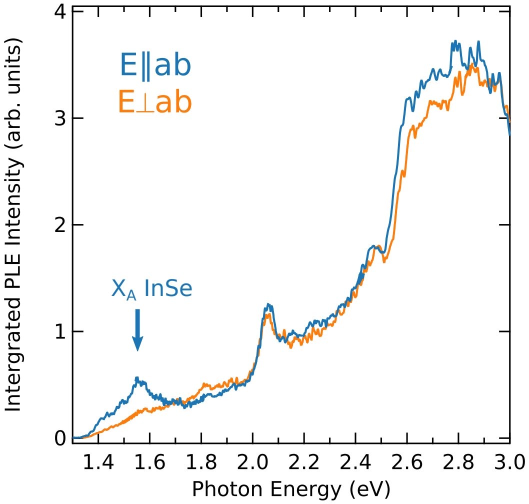

Figure A.2: Intensity of the PL measured at the energy of the emission peak of a 6L-InSe/2L-WS$_2$ interface (1.3 eV) as a function of excitation laser energy. The blue curve corresponds to having the incident excitation laser beam propagating in the interface plane (i.e., ab-plane), with the electric field polarized perpendicular to it. The orange curve corresponds to the case in which the excitation laser propagates in the direction perpendicular to the ab-plane with the electric field polarized in the plane. The only significant difference between the two cases is observed when the energy of the excitation laser beam is around 1.6 eV, corresponding to the energy of the intralayer transition in 6L-InSe. Due to the selection rules of the involved orbitals, this transition is excited only when the electric field is polarized perpendicular to the interface plane. As a result, only in this case electrons and holes are photogenerated by the incoming laser light. Subsequently, the holes are transferred to the Γ-point of 2L-WS$_2$ (see band diagram in Fig. 5.4**b** of the main text), so that the electrons –which remain in 6L-InSe– can recombine through an interlayer transition, leading to the enhancement of the PL signal observed in the measurements.

are then photogenerated in the InSe layer. Whereas the electrons stay in InSe, the holes can relax their energy and reach the top of the valence band in 2L-WS$_2$, located at Γ (see Fig. 5.4**b**). As a result, the electrons in the conduction band of InSe can radiatively recombine with the relaxed holes, increasing the intensity of the interlayer PL signal. Also these measurements therefore show that all steps from photon absorption to photon emission are consistent with both the band diagram of the interface discussed in the main text (see Fig. 5.4**b**) and with what is known about the properties of the individual layer (i.e., the requirement to induce an intralayer transition in InSe multilayers, namely the need for the polarization of the exciting light to be perpendicular to the InSe layer).

A.2 Valence and conduction band-offsets between NL-WS_2 and NL-InSe

In the main text we have discussed how we extract the value of the interfacial band gap from experiments, which enables the complete band alignment of NL-WS_2 and NL-InSe to be inferred from optical measurements. The analysis of the data also enables the relevant band offsets –i.e., not only the band-gaps– to be estimated. In the tables below we summarize the values of the band offsets that we extracted for all the interfaces discussed in the main text. Positive (Negative) values indicate that the band-edge of the system reported in the column lies above (below) the band-edge of the system reported in the line (compare with Fig. 5.4 of the main text).

Table A.1: Valence band maximum offsets in eV between NL-InSe and 2L-WS_2.

	2L-InSe	3L-InSe	4L-InSe
2L-WS_2 (Γ)	−0.39	−0.25	−0.25
2L-WS_2 (K)	−0.19	−0.05	−0.04

	5L-InSe	6L-InSe	7L-InSe
2L-WS_2 (Γ)	−0.18	−0.07	−0.07
2L-WS_2 (K)	0.03	0.13	0.13

Table A.2: Conduction band minimum offsets in eV at the interface between NL-InSe and 2L-WS_2.

	2L-InSe	3L-InSe	4L-InSe
2L-WS_2 (K)	−0.13	−0.333	−0.40

	5L-InSe	6L-InSe	7L-InSe
2L-WS_2 (K)	−0.44	−0.46	−0.48

Table A.3: Valence band maximum offsets in eV at the interface between NL-WS_2 and 4L-InSe.

	2L-WS_2 (Γ)	2L-WS_2 (K)	3L-WS_2 (Γ)	4L-WS_2 (Γ)	5L-WS_2 (Γ)
4L-InSe	0.24	−0.04	0.31	0.30	0.3

Table A.4: Conduction band minimum offsets in eV at the interface between NL-WS$_2$ and 4L-InSe.

	2L-WS$_2$ (K/Q)	3L-WS$_2$ (Q)	4L-WS$_2$ (Q)	5L-WS$_2$ (Q)
4L-InSe	0.42	0.26	0.19	0.13

Table A.5: Valence band maximum offsets in eV at the interface between 4L-InSe and 2L-TMD.

	2L-MoS$_2$ (Γ)	2L-MoS$_2$ (K)	2L-WS$_2$ (Γ)	2L-WS$_2$ (K)
4L-InSe	0.14	-0.14	0.24	0.04

	2L-MoSe$_2$ (Γ)	2L-MoSe$_2$ (K)	2L-WSe$_2$ (Γ)	2L-WSe$_2$ (K)
4L-InSe	0.43	0.36	0.73	0.67

Table A.6: Conduction band minimum offsets in eV at the interface between 4L-InSe and 2L-TMD.

	2L-MoS$_2$	2L-WS$_2$	2L-MoSe$_2$	2L-WSe$_2$
4L-InSe	0.17	0.42	0.34	0.82

A.3 Absolute PL intensity of the interface and the constituents

As discussed in the main text, the dependence of the PL signal measured on our TMD-InSe interfaces as function of temperature and laser power is characteristic of interlayer transitions direct in k-space, as expected, since the valence and conduction band edges of the constituent layers are centered at Γ. Here we show that these interlayer Γ-Γ transitions –being direct in momentum space– are in principle an efficient light emission process. Indeed, Fig. A.2**a** shows that the intensity of such an interlayer transitions (illustrated with data measured on a 2L-WS$_2$/2L-InSe sample at $T = 5$ K), can be brighter than that originating from intralayer transition in the constituent layers. This is an important consideration because, for comparison, the PL intensity in interfaces based on perfectly aligned monolayer TMDs is significantly lower than the PL emission intensity of the bare constituent layers [162].

Concerning the absolute emitted intensity, large sample-to-sample fluctuations are observed in all experiments on individual 2D materials, as well as their interfaces (*e.g.*, once again, also on interfaces of aligned TMD monolay-

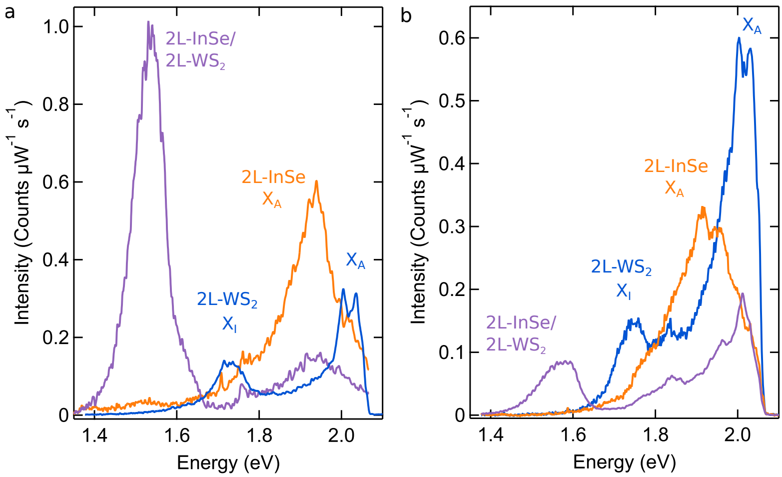

Figure A.3: **a**. Photoluminescence spectra measured at $T = 5$ K on 2L-InSe (orange line), 2L-WS$_2$ (blue line), and on their interface (purple line). The labels on the PL curves measured on the individual InSe and WS$_2$ bilayers refer to the transitions pointed to by the arrows in Fig. 5.1 of the main text. For this sample the intensity of the interface PL is larger than that of the PL emitted by constituent layers. **b**. Photoluminescence spectra measured on a different 2L-WS$_2$/2L-InSe interface, nominally identical to that shown in **a**. For this device the intensity of the interface PL is smaller than that of the constituent layers. Indeed, we find –as others have found before on interfaces of monolayer TMDs– that the PL intensity of both interface and constituent layers exhibits sizable sample-to-sample fluctuations, as it can be appreciated in the present case by comparing the two different samples shown in panel **a** and **b**.

ers, as well documented in the literature [162]). The experiments discussed in this work exhibit the same behaviour. To illustrate the issue, in Fig. A.3**a** and **b** we compare the PL intensity measured on two nominally identical 2L-InSe/2L-WS$_2$ interfaces. It is clear from the data that the observed absolute intensity depends on the specific device measured. It is also clear that this is not a specificity of the interfaces, since comparable sample-to-sample intensity fluctuations are present in the individual layers. For the systems investigated in our work (both constituent layers and interfaces), just as for TMD monolayers and their aligned interfaces reported in the literature [162], sample-to-sample variations in PL intensity of nominally identical structures can be as large as two orders of magnitude.

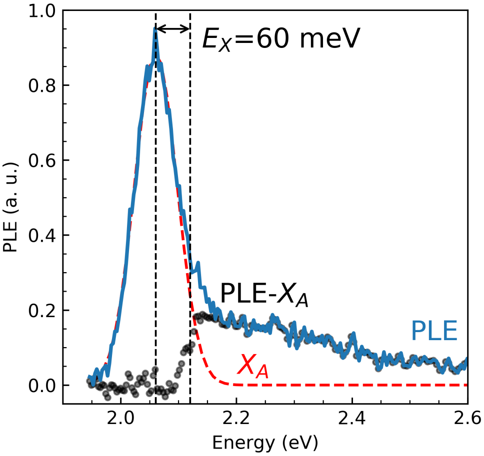

Figure A.4: PLE (solid blue line) from a standing alone InSe bilayer as function of the excitation energy of the laser. The single particle continuum onset (black circles) is obtained by substracting the exciton peak from the PLE curve. The exciton binding energy is simply the difference between the position of the exciton peak (red dashed line) and the onset of the single particle absorption continuum.

A.4 Estimate of the interlayer exciton binding energy

In the main text we have estimated the uncertainty in the energetics of the alignment of the band edges in TMD and InSe multilayers to be 100 meV or better. Part of the uncertainty comes from having neglected the interlayer exciton binding energy in our analysis. To put a bound on this quantity, we note that –owing to their larger spatial extent– interlayer excitons have binding energies that are typically smaller than for intralayer excitons. For InSe multilayers, the exciton binding energy has been recently obtained from PLE measurements, discussed in Ref. [163]. For convenience, we reproduce the basic aspects of the data here. The PLE intensity of 2L-InSe as function of the laser excitation energy (see Fig. A.4), displays an excitonic peak in the low energy part of the curve, followed by a slow monotonic decay due to single particle absorption. The difference between the peak energy and the onset of the continuum due absorption allows an exciton binding energy of approximately 60 meV to be extracted. Similar experiments –in overall agreement with theoretical calculations– show that the exciton binding energy decreases rapidly with increasing InSe thickness (20 meV for 3L, 18 meV for 4L, 14.5 meV for the bulk) [163, 164]. The exciton binding energy of WS_2 bilayers was also determined experimentally earlier (by means of a different method[165]), and found to be approximately 80 meV. We can then therefore safely conclude that for 2L-InSe/2L-WS_2 interfaces, the interlayer exciton binding energy –being smaller than that of the intralayer excitons in the consituent layers– is certainly significantly smaller than 100 meV. For interfaces based on thicker layers the value of the interlayer exciton binding energy are even much smaller.

APPENDIX B

B.1 Electrostatic gating using Li-ion conducting glass ceramics

Ionic liquid gating is a well-established technique that has been employed extensively over the last decade, and that has resulted in the observation of many fascinating phenomena [78, 166]. In contrast, the use of Li-ion glass substrates as electrolytes for electrostatic gating and for the realization of transistor devices is a much less explored technique that we introduced only a couple of years ago [81]. Because the technique is less established, in this section we present measurements performed using the ceramic back gate prior to the deposition of the ionic liquid, which confirm the proper operation of the Li-ion substrate for high-quality gating. The measurements shown here for a 4L WSe_2 device are representative of all the devices we have measured.

Fig. B.1**A** shows the source-drain current I_{SD} measured as a function of gate voltage V_{BG}, for different values of source-drain bias V_{SD}. For all values of V_{SD}, I_{SD} increases linearly past the threshold voltage, as expected for typical transfer curves of a transistor. Fig. B.1**B** shows the so-called transistor output curves, i.e. the source-drain current I_{SD} measured as a function of source-drain bias V_{SD}, for different values of gate voltage V_{BG}. The device exhibits virtually textbook behaviour, with well-defined linear and saturation regimes when sufficiently large V_{SD} values are applied with the same polarity of V_{BG}. Upon increasing V_{SD} for the opposite polarity of

V_{BG} (i.e., for positive V_{SD}), I_{SD} increases quadratically, also as expected. Finally, Fig. B.1**C** illustrates the stability of our devices, as subsequent measurements performed for negative V_{BG} over an interval of 3-4 hours show virtually no change in the current level nor in the threshold voltage V_{Th}. The overall performance of our devices is identical to that presented in Ref. [81], despite the more complex fabrication procedure involved in the realization of the structure (e.g., the presence of the Al_2O_3/Al/ Al_2O_3 tri-layer), demonstrating the robustness of Li-ion glass ceramic substrates for electrostatic gating.

Finally, we emphasize that we confine ourselves to the application of negative gate voltage to the back gate and positive gate voltage to the ionic liquid gate to operate the device under conditions in which intercalation of Li^+ ions in the WSe_2 crystal cannot occur. Actually, it is known that even with moderate positive voltage intercalation of Li-ions at room temperature does not occur [131], and that to induce intercalation very large positive gate voltages (4-7 V) are needed [25, 167]. Nevertheless, to exclude this possibility altogether we apply exclusively negative back gate voltages and positive voltages to the ionic liquid, corresponding to conditions in which Li-ions are pulled away from the WSe_2.

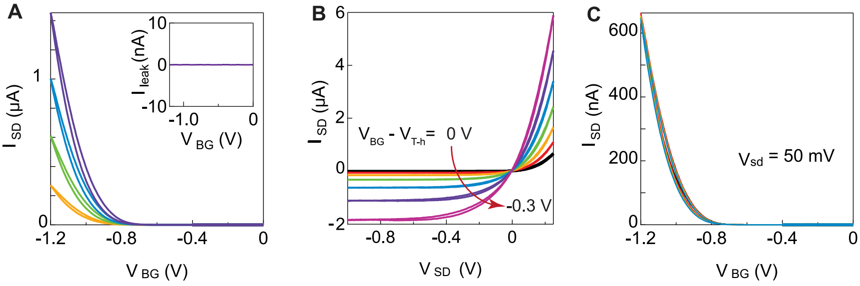

Figure B.1: A Transfer curves (I_{SD}-vs-V_{BG}) of a 4L-WSe_2 device measured prior to the deposition of the ionic liquid. For the different curves, V_{SD} is 25 mV (yellow), 50 mV (green), 75 mV (blue) and 100 mV (purple). The inset shows that the leakage current is negligibly low. **B** Output characteristics (I_{SD}-vs-V_{SD}) of the same device measured at different values of fixed $V_{BG} - V_{Th}$, showing clear linear and saturation regimes, as expected. **C** Multiple transfer curves (5 sweeps, each indicated by a different colour) measured at constant V_{SD}, acquired over a period of 3-4 hours. All the curves lie on top of each other demonstrating the reproducibility and stability of our devices.

B.2 Electrostatic decoupling of the ionic gates

In the main text we mention that to electrostatically decouple the ionic liquid and the Li-ion conductive glass ceramic we deposit an $Al_2O_3/Al/Al_2O_3$ layer between them, and ground the Al layer. This guarantees that the potential of the two electrolytes –the ionic liquid on top and the Li-ion glass on the bottom– are well defined during the double gating experiments, and controlled exclusively by the respective gate electrode, with no cross talk (i.e., the potential of the ionic liquid is insensitive to the voltage applied to the back gate, and the potential of the Li-ion glass is insensitive to the voltage applied to the gate in contact with the ionic liquid). In this section we briefly describe how we verify this condition experimentally.

As already mentioned above, ionic liquid gated transistors are commonly equipped with a reference electrode used to monitor the efficiency of the ionic liquid gate by measuring the potential between the channel of the device and the electrolyte [79]. In the case of our double ionic gated devices, two distinct reference electrodes are used, coupled to the Li-ion glass ceramic electrolyte and to the ionic liquid, consisting of two metal electrodes deposited respectively under (for the Li-ion glass) and above (for the ionic liquid) the $Al_2O_3/Al/Al_2O_3$ trilayer (see Fig B.2**A**). These reference electrodes monitor any possible coupling between the two electrolytes. Indeed, if a sizable coupling exists a change in voltage applied to one of the gates would lead to a change in the potential measured at the reference electrode coupled to the other gate.

The curves shown in Fig. B.2**B**,**C**, obtained during double gated experiments performed on a 4L WSe_2 device, show the absence of such a coupling. The data show clearly that the potential V_{Ref}^{IL}, measured at the reference electrode coupled to the ionic liquid, remains constant when sweeping the potential applied to the back gate V_{BG} (Fig B.2**B**). Similarly, the potential V_{Ref}^{BG}, measured by the reference electrode coupled to the Li-ion glass, remains constant when sweeping the voltage V_{IL} applied to the ionic liquid gate (Fig B.2**C**). The efficient decoupling of the ionic gates ensures that the potential of each electrolyte is the one expected. This is needed to ensure that the entire voltage drop occurs across the WSe_2 multilayers and that the electric field applied is estimated correctly (see **Chapter 3** for the estimate of the electric field value).

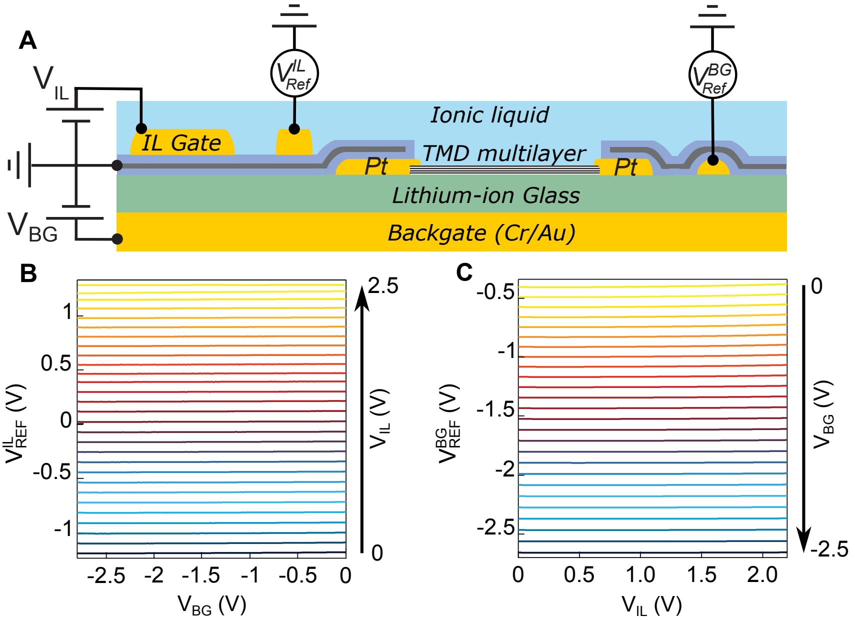

Figure B.2: **A** Side view schematics of a double ionic gated device, showing the reference electrodes in contact with the Li-ion gate (buried below the decoupling trilayer) and with the ionic liquid (deposited above the decoupling trilayer). The schematics also show the biasing configuration and the measurement units to record the voltage of the two reference electrodes. **B** Voltage of the reference electrode in contact with the ionic liquid gate (V^{IL}_{Ref}), measured as a function of the voltage applied to the Li-ion glass ceramic gate (V_{BG}) in a 4L WSe$_2$ device, for different values of V_{IL} (the voltage applied to the ionic liquid gate, which spans the range indicated by the arrow on the side; an offset is present between V^{IL}_{Ref} and V_{IL} due to the presence of a built-in potential between the gate electrode and the gated material, as it is common in ion gated devices [79]). Upon varying V_{BG}, V^{IL}_{Ref} does not change, indicating an excellent decoupling between the Li-ion glass electrolyte and the ionic liquid. **C** Voltage recorded by the reference electrode in contact with the Li-ion glass substrate (V^{BG}_{Ref}) measured as a function of voltage applied to the ionic liquid gate V_{IL} in the same 4L device, for different fixed values of V_{BG} (voltage applied to the Li-ion glass ceramic gate). The complete insensitivity of V^{BG}_{Ref} to V_{IL} shows again the perfect electrostatic decoupling of the Li-ion glass electrolyte and the ionic liquid gate.

B.3 Electrical characterisation of high quality double ionic gate devices

A number of aspects of ionic gating serve as indicators of the quality of the devices, which is essential to perform reliable measurements. This section addresses in detail the three main ones –hysteresis in the transfer curves, the level of leakage current, and measurement reproducibility– to demonstrate the excellent quality of our devices.

Hysteresis in the transfer curves originates from a time lag between changing the voltage applied to a gate electrode and having a stable potential on the transistor channel. It manifests itself as a difference in the source-drain current I_{SD} measured upon increasing and decreasing the gate voltage (i.e., a difference in the value of I_{SD} measured in the up and down sweeps of the voltage applied to the gate). Hysteresis is unavoidably present in all devices, but in poorly functioning devices –such as devices in which strong trapping of charge carrier occurs– hysteresis can drastically affect the shape of the transfer curve. In our experiments, we minimize hysteresis by sweeping the voltage applied to the gate extremely slowly –never faster than 5mV/s– to ensure that the slow ionic motion in the electrolytes can follow the change of the voltage applied to the gate electrodes. Indeed, the maps of the current I_{SD} in a 4L-WSe$_2$ device when the ionic liquid is swept down (from $\mathrm{V}_{IL} = 2.8\ V$ to $\mathrm{V}_{IL} = 0\ V$, see Fig. B.3**A**) and swept up (V_{IL} going from 0 V to 2.8 V, Fig. B.3**B**) exhibit an identical qualitative behaviour, and only minor quantitative deviations. Both maps show the closing of the semiconducting gap (as discussed in the main text) for nearly identical levels of applied gate voltages. The small hysteresis is further illustrated in Fig B.3**C**, which shows three cuts of the current I_{SD}, corresponding to measurements taken upon sweeping the voltage applied to the ionic liquid gate for fixed voltage applied to the Li-ion back gate (V_{BG}=0 V (orange), −1.5 V (green) and −2.5 V (blue)). The data show that hysteresis in our double gated devices is in all regards comparable to what is commonly observed in high quality single ionic gate transistors.

Fig. B.4**A-B** show the full map of gate leakage currents measured as a function of V_{IL} and V_{BG}, during the measurements plotted in Fig. B.3**A**. The leakage current levels are extremely small, below 1 nA (close to the noise floor of our system), throughout the entire range of gate voltages. Panel **C** shows cuts of the maps respectively at $V_{IL} = 0$ V and $V_{BG} = 0$ V, in which we can see clearly the level of the leakage current. Similar behaviour has been observed for all devices in which we observed the quenching of the band gap.

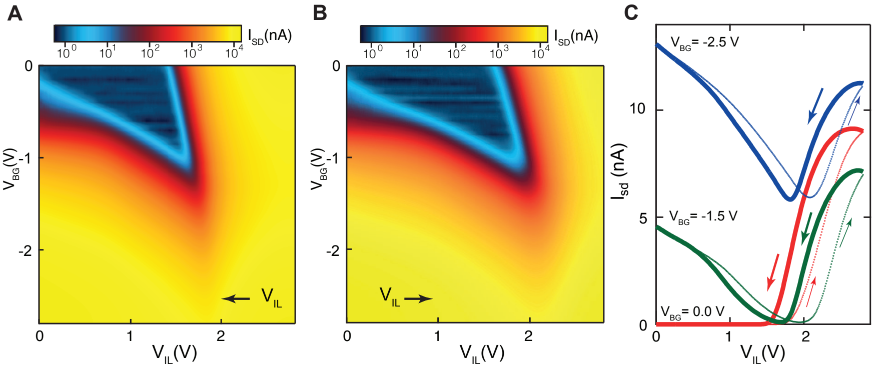

Figure B.3: **A**-**B** Maps of the current in a 4L-WSe$_2$ device measured upon sweeping the voltage applied to the ionic liquid down (i.e., from high to low voltage; **A**) and up **B**, as indicated by the black arrow on the maps (the data in panel **A** is the same as that shown as a function of $V*$ and $\mathscr{E}$ in Fig. 4**C** in the main text). The behaviour observed is virtually identical for both sweeping directions, except for a small threshold voltage shift, which we attribute to bias stress (as commonly observed in ionic gate transistors). **C** Cuts of I_{SD} vs V$_{IL}$ measured at different fixed values of back gate voltages (V$_{BG} = 0$ V, -1.5 V and -2.5 V) showing both up-sweeps (from 0 V to 2.8 V, dashed line) and down-sweeps (from 2.8 V to 0 V, solid line) directions.

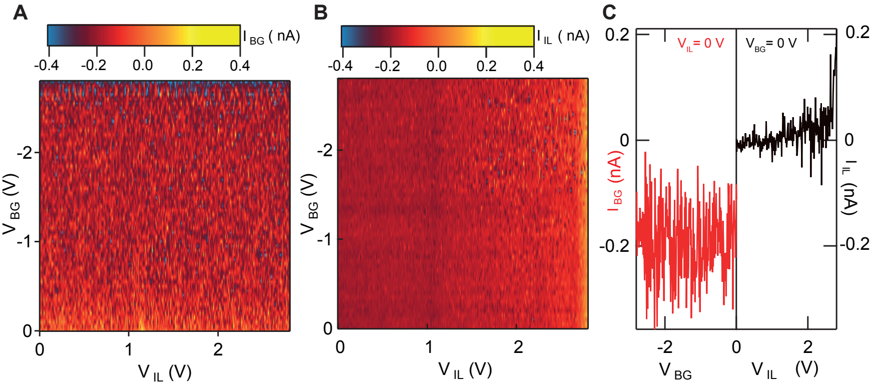

Figure B.4: **A** Backgate and **B** ionic liquid gate leakage current maps measured concomitantly with the data presented in Fig. B.3**A**. In both cases, the leakage current remains well below 1 nA over the whole measurement. **C** Representative back gate (red) and IL gate (black) leakage current curves, measured respectively for $V_{IL} = 0$ and $V_{BG} = 0$.

The third aspect showing the high quality of our measurements and

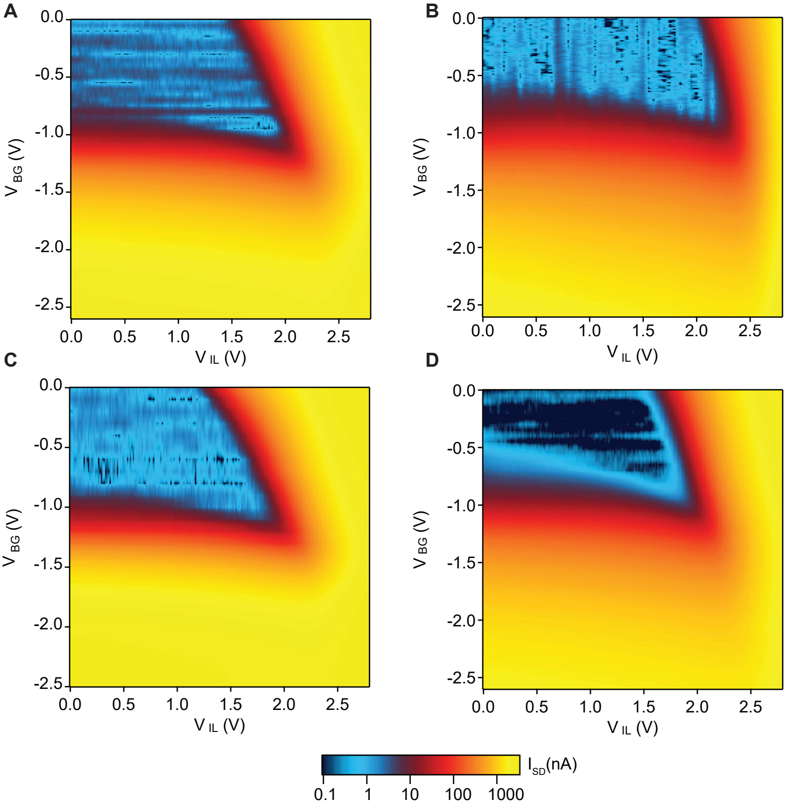

Figure B.5: Reproducibility of double ionic gated devices. **A**-**D** show 2D maps of the current measured in a 7L-WSe$_2$ device as a function of V_{IL} and V_{BG} ($V_{SD} = 50$ mV) during four subsequent measurements runs. In **A**-**C** the measurements were performed by sweeping V_{IL} down (from 2.8 V to 0 V) and varying V_{BG} at the end of each sweep. In **D** V_{BG} was swept down and V_{IL} was varied at the end of each sweep.

the robustness of the findings reported in the main text is the high level of reproducibility of the measurements performed in our double ionic gated devices. In Fig. B.5**A**-**D** we plot the dependence of the source-drain current I_{SD} (measured at fixed $V_{SD} = 50$ mV) as a function of V_{IL} and V_{BG}, obtained from experiments performed on a 7L-WSe$_2$ device, whose behaviour is completely compatible with that of the thinner multilayers discussed in the main text (its critical field is shown in Fig. 7.4**G** of the main text). As each one of the 2D maps shown requires 20-30 hours of continuous measurements, the data shown confirm the stability of the device of a period of several days. The maps shown in Fig. B.5**A**, **B**, and **C** were obtained by sweeping the voltage applied to the ionic liquid gate, while incrementing at the end of each sweep the voltage applied to the Li-ion glass ceramic gate. The opposite procedure (sweeping the voltage applied to the Li-ion glass ceramic gate at fixed voltage applied to ionic liquid gate) was followed to acquire the data shown in Fig. B.5**D**. As it can be seen, the features displayed in the four 2D maps –such as the suppression of the off-state, the values of the threshold voltages, or the maximum current levels recorded– are nearly identical in all measurements. The variations between the maps are small and can be attributed to bias stress.

In summary, all measurements shown in this section indicate the high quality of our devices and the reliability and reproducibility of our measurements.

B.4 Evolution of output characteristics with applied electric fields

In the main text, we illustrate the possibility to quench the band gap of WSe_2 multilayers with an applied perpendicular electric field via double gated experiments performed at fixed V_{SD} value. The reduction and eventual quenching of the band gap of the multilayers with electric field should also result in an evolution of the I_{SD}-vs-V_{SD} curves of the device; from the absence of any sizeable current at low electric field (with the chemical potential initially inside the gap) to a linear dependence of I_{SD} on V_{SD} at high field when the gap is quenched.

In this section we present the evolution of the I_{SD}-vs-V_{SD} curves upon increasing perpendicular electric field on a 4L WSe_2 device (see Fig. B.6), confirming that the gap closes for large electric fields. For small values of $\mathscr{E}_{TMD}$ a pronounced suppression of I_{SD} over a broad V_{SD} range is observed when the device is biased at $V^\star = V_{IL} + V_{BG} = 0.2$ V, corresponding –for $V_{SD} = 0$ V– to setting the chemical potential well inside the gap. Upon increasing $\mathscr{E}_{TMD}$ (with $V^\star$ fixed), the I_{SD} suppression becomes less pronounced and eventually the I_{SD}-vs-V_{SD} curve becomes perfectly linear. That is what happens after the gap has closed, when the overlap of valence and conduction band is sufficiently large.

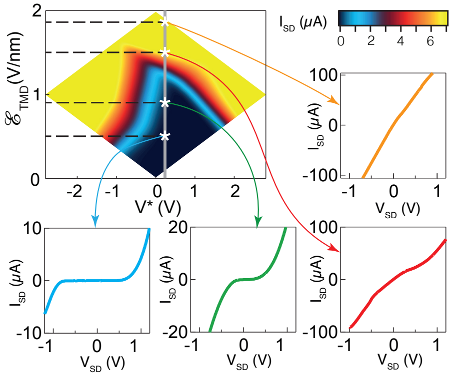

Figure B.6: Evolution of the I_{SD}-vs-V_{SD} curves with increasing electric field. The top left panel is a linear-scale colour plot of I_{SD} in a 4L WSe$_2$ device measured as a function of $V^\star = V_{IL} + V_{BG}$ and of perpendicular electric field $\mathscr{E}_{TMD}$. The other surrounding panels –with curves of different colour– show the I_{SD}-vs-V_{SD} characteristics of our transistor measured at $V^\star = 0.2$ V for different values of $\mathscr{E}_{TMD}$ (indicated by the white starts in the colour plot). At $\mathscr{E}_{TMD} = 0.5$ V/nm (blue curve) a very strong non-linearity with a large suppression of I_{SD} at small V_{SD} is clearly visible, as expected (because $V^\star = 0.2$ V corresponds to having the chemical potential inside the band gap of 4L-WSe$_2$). Upon increasing the perpendicular electric field, the non-linearity in the I_{SD}-vs-V_{SD} characteristics becomes less pronounced (green curve, $\mathscr{E}_{TMD} = 0.87$ V/nm). Increasing the perpendicular electric field further fully quenches the gap, causing the suppression of I_{SD} at low V_{SD} to become negligible (red curve, $\mathscr{E}_{TMD} = 1.5$ V/nm), and eventually resulting in a virtually perfectly linear I_{SD}-vs-V_{SD} curve (orange curve, $\mathscr{E}_{TMD} = 1.9$ V/nm).

B.5 Thickness dependence of critical field from first-principles simulations

In order to compute the critical electric field $\mathscr{E}_c$ at which the energy gap of a WSe$_2$ multilayer vanishes, we have carried out first-principles density-functional-theory (DFT) simulations within the Perdew-Burke-Ernzerhof (PBE) [168] generalized-gradient approximation as implemented in the Quantum ESPRESSO distribution [169, 170]. Here we outline the main technical aspects of our calculations and present the results.

In our calculations, the crystal structure of multilayers is obtained from the experimentally reported structure of bulk WSe$_2$, by cutting out a certain number of layers, without further relaxations. The Brillouin zone is sampled with $12 \times 12 \times 1$ k-points in a uniform Γ-centered Monkhorst-Pack grid. Electron-ion interactions are treated with a fully-relativistic pseudopotential approach using the norm-conserving procedure as refined in the optimized norm-conserving Vanderbilt pseudopotential (ONCVPSP) approach [171] with parameters from the Pseudo DOJO library [172] and a cutoff energy on wavefunctions of 80 Ry. Spurious interactions with periodic replicas of the multilayers in the direction orthogonal to the layers are suppressed by using a cutoff on long-range interactions [173]. The band structure is computed over a fine grid using Wannier interpolation [174] and the gap is computed as the energy difference between the bottom of the conduction bands and the top of the valence bands.

For each multilayer the energy band gap is computed for several values of the electric field $\mathscr{E}$ by putting charged sheets with uniform and opposite charge densities $\pm\sigma$ at the two sides of the multilayers –thus mimicking a double-gate set up– through the implementation of Ref. [173]. Fig. B.7 shows the band structure of different multilayers for several values of $\mathscr{E}_{TMD}$, obtained by taking the potential difference ΔV_{TMD} between the two sides of the multilayer associated with the total potential (external + Hartree) and dividing by the multilayer thickness t_{TMD}, that is $\mathscr{E}_{TMD} = \Delta V_{TMD}/t_{TMD}$. Fig. B.8 shows the energy gap of different multilayers as a function of the internal electric field. The gap is monotonically decreasing with increasing electric field, and vanishes at a critical value $\mathscr{E}_c$. Such critical field, emphasised with vertical dashed lines, is reported as a function of the number of layers in Fig. 7.4**H** of the main text with empty diamonds. We note that, in agreement with the experimental observation, $\mathscr{E}_c$ decreases with the thickness of the multilayer.

The quantitative comparison with experiments reported Fig. 7.4**H** of the main text shows that the theoretical value is slightly suppressed with respect to the one extracted from measurements, as a result of the well-known underestimation of energy band gaps in standard DFT approximations [175]. For instance, the experimentally reported [79] zero-field band gaps of WSe_2 mono- and bilayers are 1.81 and 1.62 eV, respectively, while PBE-DFT calculations provide slightly lower values, $E_g = 1.34$ and 1.21 eV for $N = 1$ and 2, respectively. To show that the main source of discrepancy between theory and experiments is indeed only the underestimation of the zero-field band gap, in Fig. 7.4**H** of the main text we also show with filled diamonds the theoretical results for the critical field rescaled by the same factor necessary to correct the predicted energy gap and reproduce measured data [176]. Once the zero-field DFT-PBE energy gap is corrected, we then have a much better agreement between theory and experiments for the critical field at which the energy gap vanishes.

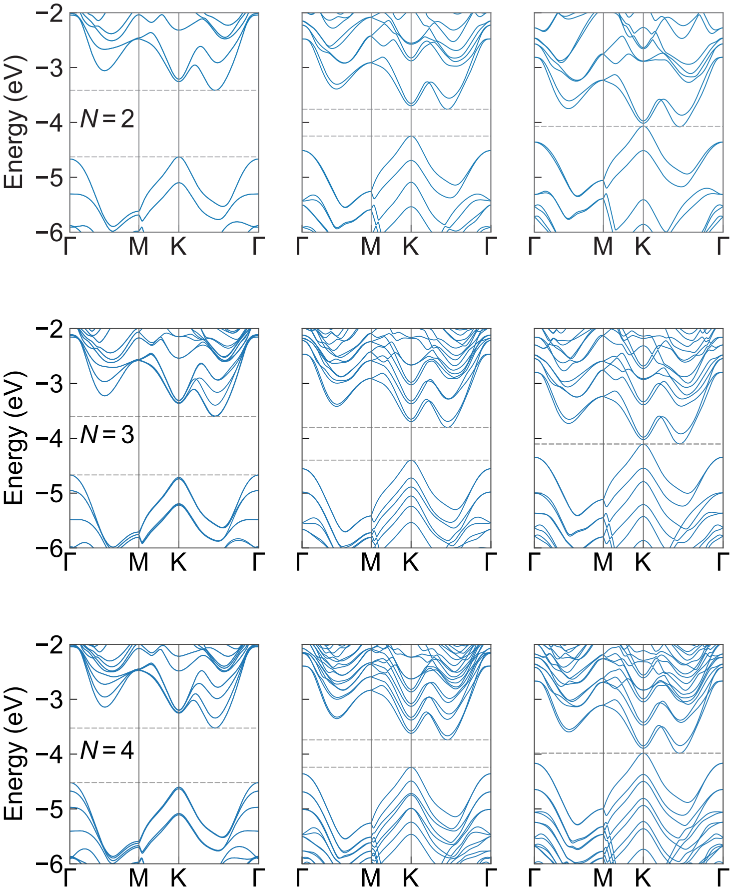

Figure B.7: Computed band structure of multilayers. Band structure of WSe_2 multilayers computed within density-functional theory along a high-symmetry path in the Brillouin zone. Panels are arranged so that different rows correspond to different multilayer thicknesses ($N = 2, 3, 4$ from top to bottom) and different columns to different electric fields (zero, intermediate and critical field, from left to right). Dashed lines emphasize the energy of the valence band maximum and conduction band minimum, which coincide at the critical field corresponding to the gap-closing condition (rightmost panels). Similar results have been obtained also for thicker multilayers ($N = 6, 8$, not shown).

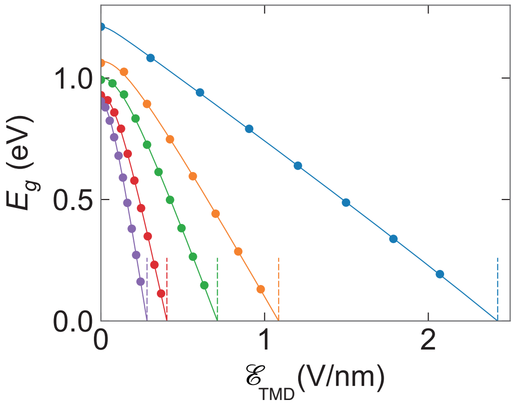

Figure B.8: Electric-field dependent band gap of WSe_2 multilayers. First-principles results for the evolution of the energy gap in WSe_2 multilayers with $N = 2$ (blue), 3 (orange), 4 (green), 6 (red), and 8 (violet) as a function of electric field. Vertical dashed lines mark the critical electric field at which the energy gap vanishes, $\mathscr{E}_c$, which is also reported in Fig. 7.4**H** of the main text. The qualitative trend of $\mathscr{E}_c$ with the number of layers reproduces very well the experimental results, although theoretical predictions tend to underestimate the critical field. The lower theoretical values are to be expected as a result of the frequently reported tendency of approximate DFT to underestimate the energy gap. Better agreement with experiments is indeed recovered when theoretical results are rescaled to reproduce measured band gaps (see filled diamonds in Fig. 7.4**H** of the main text).

Bibliography

[1] S. M. Girvin and K. Yang, *Modern condensed matter physics* (Cambridge University Press, Feb. 2019).

[2] K. S. Novoselov et al., “Electric Field Effect in Atomically Thin Carbon Films”, Science **306**, 666–669 (2004).

[3] A. K. Geim and K. S. Novoselov, “The rise of graphene”, Nature Materials **6**, 183–191 (2007).

[4] C. Barceló, S. Liberati, and M. Visser, “Analogue Gravity”, Living Rev. Relativ. **14**, 3 (2011).

[5] Y. Dong et al., “Fizeau drag in graphene plasmonics”, Nature **594**, 513–516 (2021).

[6] A. Iorio and G. Lambiase, “Quantum field theory in curved graphene spacetimes, Lobachevsky geometry, Weyl symmetry, Hawking effect, and all that”, Phys. Rev. D **90**, 025006 (2014).

[7] P. Avouris, T. F. Heinz, and T. Low, eds., *2D Materials: Properties and Devices* (Cambridge University Press, Cambridge, 2017).

[8] M. I. Katsnelson, K. S. Novoselov, and A. K. Geim, “Chiral tunnelling and the Klein paradox in graphene”, Nature Phys **2**, 620–625 (2006).

[9] K. S. Novoselov et al., “Two-dimensional atomic crystals”, PNAS **102**, 10451–10453 (2005).

[10] N. Mounet et al., “Two-dimensional materials from high-throughput computational exfoliation of experimentally known compounds”, Nature Nanotechnology **13**, 246–252 (2018).

[11] M. Gibertini et al., “Magnetic 2D materials and heterostructures”, Nature Nanotechnology **14**, 408–419 (2019).

[12] A. V. Kolobov and J. Tominaga, *Two-Dimensional Transition-Metal Dichalcogenides*, Vol. 239, Springer Series in Materials Science (Springer International Publishing, Cham, 2016).

[13] S. Manzeli et al., “2D transition metal dichalcogenides”, Nature Reviews Materials **2**, 1–15 (2017).

[14] K. F. Mak et al., “Observation of an Electric-Field-Induced Band Gap in Bilayer Graphene by Infrared Spectroscopy”, Phys. Rev. Lett. **102**, 256405 (2009).

[15] K. F. Mak et al., “Atomically Thin MoS_2: A New Direct-Gap Semiconductor”, Phys. Rev. Lett. **105**, 136805 (2010).

[16] B. Radisavljevic et al., “Single-layer MoS_2 transistors”, Nature Nanotechnology **6**, 147–150 (2011).

[17] F. H. L. Koppens et al., “Photodetectors based on graphene, other two-dimensional materials and hybrid systems”, Nature Nanotechnology **9**, 780–793 (2014).

[18] D. Akinwande, N. Petrone, and J. Hone, “Two-dimensional flexible nanoelectronics”, Nature Communications **5**, 5678 (2014).

[19] A. Avsar et al., “Probing magnetism in atomically thin semiconducting $PtSe_2$”, Nat Commun **11**, 4806 (2020).

[20] M. N. Ali et al., “Large, non-saturating magnetoresistance in WTe_2”, Nature **514**, 205–208 (2014).

[21] X. Qian et al., “Quantum spin Hall effect in two-dimensional transition metal dichalcogenides”, Science **346**, 1344–1347 (2014).

[22] Y. Zhao et al., “Anisotropic magnetotransport and exotic longitudinal linear magnetoresistance in WTe_2 crystals”, Phys. Rev. B **92**, 041104 (2015).

[23] I. Cucchi et al., “Microfocus Laser–Angle-Resolved Photoemission on Encapsulated Mono-, Bi-, and Few-Layer 1T-WTe_2”, Nano Lett. **19**, 554–560 (2019).

[24] B. Sipos et al., “From Mott state to superconductivity in 1T-TaS_2”, Nature Mater **7**, 960–965 (2008).

[25] Y. Yu et al., “Gate-tunable phase transitions in thin flakes of 1T-TaS_2”, Nature Nanotechnology **10**, 270–276 (2015).

[26] G. Wang et al., “Colloquium: Excitons in atomically thin transition metal dichalcogenides”, Rev. Mod. Phys. **90**, 021001 (2018).

[27] Y. Jiang et al., “Interlayer exciton formation, relaxation, and transport in TMD van der Waals heterostructures”, Light Sci Appl **10**, 72 (2021).

[28] A. K. Geim and I. V. Grigorieva, “Van der Waals heterostructures”, Nature **499**, 419–425 (2013).

[29] K. S. Novoselov et al., “2d materials and van der Waals heterostructures”, Science **353**, aac9439 (2016).

[30] R. Dingle et al., “Electron mobilities in modulation-doped semiconductor heterojunction superlattices”, Appl. Phys. Lett. **33**, 665–667 (1978).

[31] A. Ohtomo and H. Y. Hwang, “A high-mobility electron gas at the $LaAlO_3/SrTiO_3$ heterointerface”, Nature **427**, 423–426 (2004).

[32] C. Huang et al., “Lateral heterojunctions within monolayer $MoSe_2$ –WSe_2 semiconductors”, Nature Materials **13**, 1096–1101 (2014).

[33] Z. Wang et al., “Tunneling Spin Valves Based on $Fe_3GeTe_2/hBN/Fe_3GeTe_2$ van der Waals Heterostructures”, Nano Lett. **18**, 4303–4308 (2018).

[34] P. Rivera et al., “Observation of long-lived interlayer excitons in monolayer $MoSe_2$-WSe_2 heterostructures”, Nat. Commun. **6**, 6242 (2015).

[35] E. Ponomarev et al., “Semiconducting van der Waals Interfaces as Artificial Semiconductors”, Nano Lett. **18**, 5146–5152 (2018).

[36] B. A. Reddy et al., “Synthetic Semimetals with van der Waals Interfaces”, Nano Lett. **20**, 1322–1328 (2020).

[37] N. Ubrig et al., “Design of van der Waals interfaces for broad-spectrum optoelectronics”, Nature Materials **19**, 299–304 (2020).

[38] D. J. Rizzo et al., “Charge-Transfer Plasmon Polaritons at Graphene/α-RuCl $_3$ Interfaces”, Nano Lett. **20**, 8438–8445 (2020).

[39] Y. Wang et al., “Modulation Doping via a Two-Dimensional Atomic Crystalline Acceptor”, Nano Lett. **20**, 8446–8452 (2020).

[40] Y. Yu et al., “High-temperature superconductivity in monolayer Bi_2 $Sr_2CaCu_2O_{8+\delta}$”, Nature **575**, 156–163 (2019).

[41] S. Y. F. Zhao et al., “Sign-Reversing Hall Effect in Atomically Thin High-Temperature $Bi_{2.1}Sr_{1.9}Ca$ $Cu_{2.0}O_{8+\delta}$ Superconductors”, Phys. Rev. Lett. **122**, 247001 (2019).

[42] Y. Cao et al., “Unconventional superconductivity in magic-angle graphene superlattices”, Nature **556**, 43–50 (2018).

[43] H. Yu et al., “Anomalous Light Cones and Valley Optical Selection Rules of Interlayer Excitons in Twisted Heterobilayers”, Phys. Rev. Lett. **115**, 187002 (2015).

[44] B. A. Reddy et al., “Synthetic semimetals with van der Waals interfaces”, Nano Letters **20**, 1322–1328 (2020).

[45] L. Tao et al., “Silicene field-effect transistors operating at room temperature”, Nature Nanotechnology **10**, 227–231 (2015).

[46] R. A. Bromley, R. B. Murray, and A. D. Yoffe, “The band structures of some transition metal dichalcogenides. III. Group VIA: trigonal prism materials”, J. Phys. C: Solid State Phys. **5**, 759–778 (1972).

[47] L. F. Mattheiss, “Band Structures of Transition-Metal-Dichalcogenide Layer Compounds”, Phys. Rev. B **8**, 3719–3740 (1973).

[48] A. Splendiani et al., “Emerging photoluminescence in monolayer MoS_2”, Nano Lett. **10**, 1271–1275 (2010).

[49] S. Manzeli et al., “2D transition metal dichalcogenides”, Nat Rev Mater **2**, 1–15 (2017).

[50] G.-B. Liu et al., “Three-band tight-binding model for monolayers of group-VIB transition metal dichalcogenides”, Phys. Rev. B **88**, 085433 (2013).

[51] S. Fang et al., “Ab initio tight-binding Hamiltonian for transition metal dichalcogenides”, Phys. Rev. B **92**, 205108 (2015).

[52] A. Ramasubramaniam, D. Naveh, and E. Towe, “Tunable band gaps in bilayer transition-metal dichalcogenides”, Physical Review B **84**, 205325 (2011).

[53] X. Dai et al., “Bandstructure modulation of two-dimensional WSe_2 by electric field”, Journal of Applied Physics **117**, 084310 (2015).

[54] J. B. Oostinga et al., “Gate-induced insulating state in bilayer graphene devices”, Nature Materials **7**, 151–157 (2008).

[55] Y. Zhang et al., “Direct observation of a widely tunable bandgap in bilayer graphene”, Nature **459**, 820–823 (2009).

[56] X. Qian et al., “Quantum spin Hall effect in two-dimensional transition metal dichalcogenides”, Science **346**, 1344–1347 (2014).

[57] Q. Tong et al., “Topological mosaics in Moiré superlattices of van der Waals heterobilayers”, Nature Physics **13**, 356–362 (2017).

[58] Q. Zhu et al., “Gate tuning from exciton superfluid to quantum anomalous Hall in van der Waals heterobilayer”, Science Advances **5**, eaau6120 (2019).

[59] A. Marrazzo et al., “Prediction of a large-gap and switchable Kane-Mele quantum spin Hall insulator”, Phys. Rev. Lett. **120**, 117701 (2018).

[60] C. Xu et al., “Electric-field switching of magnetic topological charge in type-I multiferroics”, Phys. Rev. Lett. **125**, 037203 (2020).

[61] S. Wang et al., “Tunable Schottky barrier in graphene/graphene-like germanium carbide van der Waals heterostructure”, Scientific Reports **9**, 5208 (2019).

[62] J. Wang et al., “Electric field-tunable structural phase transitions in monolayer tellurium”, ACS Omega **5**, 18213–18217 (2020).

[63] C. Ke et al., “Tuning the electronic, optical, and magnetic properties of monolayer GaSe with a vertical electric field”, Phys. Rev. Applied **9**, 044029 (2018).

[64] Y. Sun et al., “InSe: a two-dimensional material with strong interlayer coupling”, Nanoscale **10**, 7991–7998 (2018).

[65] V. Zólyomi, N. D. Drummond, and V. I. Fal’ko, “Band structure and optical transitions in atomic layers of hexagonal gallium chalcogenides”, Phys. Rev. B **87**, 195403 (2013).

[66] S. J. Magorrian, V. Zólyomi, and V. I. Fal’ko, “Electronic and optical properties of two-dimensional InSe from a DFT-parametrized tight-binding model”, Phys. Rev. B **94**, 245431 (2016).

[67] M. J. Hamer et al., “Indirect to Direct Gap Crossover in Two-Dimensional InSe Revealed by Angle-Resolved Photoemission Spectroscopy”, ACS Nano **13**, 2136–2142 (2019).

[68] H. Henck et al., “Evidence of direct electronic band gap in two-dimensional van der Waals indium selenide crystals”, Phys. Rev. Materials **3**, 034004 (2019).

[69] D. A. Bandurin et al., “High electron mobility, quantum Hall effect and anomalous optical response in atomically thin InSe”, Nat. Nanotechnol. **12**, 223–227 (2017).

[70] Y. Li et al., “Accurate identification of layer number for few-layer WS_2 and WSe_2 via spectroscopic study”, Nanotechnology **29**, 124001 (2018).

[71] V. O. Özçelik et al., “Band alignment of two-dimensional semiconductors for designing heterostructures with momentum space matching”, Phys. Rev. B **94**, 035125 (2016).

[72] M. Z. Bellus et al., “Type-I van der Waals heterostructure formed by MoS_2 and ReS_2 monolayers”, Nanoscale Horiz. **2**, 31–36 (2016).

[73] I. Ferain, C. A. Colinge, and J.-P. Colinge, “Multigate transistors as the future of classical metal–oxide–semiconductor field-effect transistors”, Nature **479**, 310–316 (2011).

[74] K.-C. Kao, *Dielectric phenomena in solids: with emphasis on physical concepts of electronic processes* (Elsevier Academic Press, San Diego, 2004).

[75] J. Verweij and J. Klootwijk, “Dielectric breakdown I: a review of oxide breakdown”, Microelectronics Journal **27**, 611–622 (1996).

[76] T. Fujimoto and K. Awaga, “Electric-double-layer field-effect transistors with ionic liquids”, Physical Chemistry Chemical Physics **15**, 8983–9006 (2013).

[77] E. Schmidt et al., “Characterization of the Electric Double Layer Formation Dynamics of a Metal/Ionic Liquid/Metal Structure”, ACS Applied Materials & Interfaces **8**, 14879–14884 (2016).

[78] S. Z. Bisri et al., “Endeavor of Iontronics: From Fundamentals to Applications of Ion-Controlled Electronics”, Advanced Materials **29**, 1607054 (2017).

[79] I. Gutiérrez-Lezama et al., “Ionic gate spectroscopy of 2D semiconductors”, Nature Reviews Physics, 1–12 (2021).

[80] H. Yuan et al., “High-Density Carrier Accumulation in ZnO Field-Effect Transistors Gated by Electric Double Layers of Ionic Liquids”, Advanced Functional Materials **19**, 1046–1053 (2009).

[81] M. Philippi et al., “Lithium-ion conducting glass ceramics for electrostatic gating”, Applied Physics Letters **113**, 033502 (2018).

[82] H. Zhang et al., “Band Filling and Cross Quantum Capacitance in Ion-Gated Semiconducting Transition Metal Dichalcogenide Monolayers”, Nano Letters **19**, 8836–8845 (2019).

[83] P. Blake et al., “Making graphene visible”, Appl. Phys. Lett. **91**, 063124 (2007).

[84] I. Jung et al., “Simple Approach for High-Contrast Optical Imaging and Characterization of Graphene-Based Sheets”, Nano Lett. **7**, 3569–3575 (2007).

[85] Z. H. Ni et al., “Graphene Thickness Determination Using Reflection and Contrast Spectroscopy”, Nano Lett. **7**, 2758–2763 (2007).

[86] A. Castellanos-Gomez, N. Agraït, and G. Rubio-Bollinger, “Optical identification of atomically thin dichalcogenide crystals”, Appl. Phys. Lett. **96**, 213116 (2010).

[87] M. M. Benameur et al., “Visibility of dichalcogenide nanolayers”, Nanotechnology **22**, 125706 (2011).

[88] C. R. Dean et al., “Boron nitride substrates for high-quality graphene electronics”, Nature Nanotechnology **5**, 722–726 (2010).

[89] L. A. Ponomarenko et al., “Tunable metal–insulator transition in double-layer graphene heterostructures”, Nat. Phys. **7**, 958–961 (2011).

[90] S. J. Haigh et al., “Cross-sectional imaging of individual layers and buried interfaces of graphene-based heterostructures and superlattices”, Nature Materials **11**, 764–767 (2012).

[91] L. Britnell et al., “Field-Effect Tunneling Transistor Based on Vertical Graphene Heterostructures”, Science **335**, 947–950 (2012).

[92] A. Castellanos-Gomez et al., “Deterministic transfer of two-dimensional materials by all-dry viscoelastic stamping”, 2D Mater. **1**, 011002 (2014).

[93] P. J. Zomer et al., “Fast pick up technique for high quality heterostructures of bilayer graphene and hexagonal boron nitride”, Applied Physics Letters **105**, 013101 (2014).

[94] D. Domaretskiy et al., “Identifying atomically thin crystals with diffusively reflected light”, 2D Materials **8**, 045016 (2021).

[95] N. Ubrig et al., “Design of van der waals interfaces for broad-spectrum optoelectronics”, Nature Materials **19**, 299–304 (2020).

[96] H. Fang et al., “Strong interlayer coupling in van der Waals heterostructures built from single-layer chalcogenides”, Proceedings of the National Academy of Sciences **111**, 6198–6202 (2014).

[97] P. Rivera et al., “Interlayer valley excitons in heterobilayers of transition metal dichalcogenides”, Nat. Nanotechnol. **13**, 1004 (2018).

[98] A. Castellanos-Gomez et al., “Local Strain Engineering in Atomically Thin MoS_2”, Nano Lett. **13**, 5361–5366 (2013).

[99] J. S. Ross et al., “Interlayer Exciton Optoelectronics in a 2d Heterostructure p-n Junction”, Nano Lett. **17**, 638–643 (2017).

[100] L. Mennel, M. Paur, and T. Mueller, “Second harmonic generation in strained transition metal dichalcogenide monolayers: MoS_2, $MoSe_2$, WS_2, and WSe_2”, APL Photonics **4**, 034404 (2018).

[101] A. Ciarrocchi et al., “Polarization switching and electrical control of interlayer excitons in two-dimensional van der Waals heterostructures”, Nat. Photonics **13**, 131 (2019).

[102] C.-H. Lee et al., “Atomically thin p–n junctions with van der Waals heterointerfaces”, Nat. Nanotechnol. **9**, 676–681 (2014).

[103] M. M. Furchi et al., “Photovoltaic Effect in an Electrically Tunable van der Waals Heterojunction”, Nano Lett. **14**, 4785–4791 (2014).

[104] T. Mueller, A. Pospischil, and M. M. Furchi, “2d materials and heterostructures for applications in optoelectronics”, in Micro- and Nanotechnology Sensors, Systems, and Applications VII, Vol. 9467 (May 2015), p. 946713.

[105] J. Binder et al., “Upconverted electroluminescence via Auger scattering of interlayer excitons in van der Waals heterostructures”, Nat. Commun. **10**, 2335 (2019).

[106] H. Zhu et al., “Interfacial Charge Transfer Circumventing Momentum Mismatch at Two-Dimensional van der Waals Heterojunctions”, Nano Lett. **17**, 3591–3598 (2017).

[107] G. W. Mudd et al., “Tuning the Bandgap of Exfoliated InSe Nanosheets by Quantum Confinement”, Adv. Mater. **25**, 5714–5718 (2013).

[108] E. O. Göbel and K. Ploog, “Fabrication and optical properties of semiconductor quantum wells and superlattices”, Prog. Quantum Electron. **14**, 289–356 (1990).

[109] L. He et al., “MBE growth of (111) CdTe on Zn-stabilized and Se-stabilized (100) ZnSe”, J. Cryst. Growth **101**, 147–152 (1990).

[110] K. P. O’Donnell and B. Henderson, “The Zn(Cd)S(Se) family of superlattices”, J. Lumin. **52**, 133–146 (1992).

[111] E. T. Yu, J. O. McCaldin, and T. C. McGill, “Band Offsets in Semiconductor Heterojunctions”, in *Solid State Physics*, Vol. 46, edited by H. Ehrenreich and D. Turnbull (Academic Press, Jan. 1992), pp. 1–146.

[112] L. V. Butov et al., “Photoluminescence kinetics of indirect excitons in GaAs/$\mathrm{Al}_x\mathrm{Ga}_{1-x}\mathrm{As}$ coupled quantum wells”, Phys. Rev. B **59**, 1625–1628 (1999).

[113] H. Kroemer, “Nobel Lecture: Quasielectric fields and band offsets: teaching electrons new tricks”, Rev. Mod. Phys. **73**, 783–793 (2001).

[114] C. F. Klingshirn, *Semiconductor Optics*, 4th ed., Graduate Texts in Physics (Springer-Verlag, Berlin Heidelberg, 2012).

[115] L. V. Butov, “Excitonic devices”, Superlattices Microstruct., Indirect Excitons: Physics and Applications **108**, 2–26 (2017).

[116] W. Zhao et al., “Evolution of Electronic Structure in Atomically Thin Sheets of WS_2 and WSe_2”, ACS Nano **7**, 791–797 (2013).

[117] W. Zhao et al., “Origin of Indirect Optical Transitions in Few-Layer MoS_2, WS_2, and WSe_2”, Nano Lett. **13**, 5627–5634 (2013).

[118] G. W. Mudd et al., “High Broad-Band Photoresponsivity of Mechanically Formed InSe–Graphene van der Waals Heterostructures”, Adv. Mater. **27**, 3760–3766 (2015).

[119] G. W. Mudd et al., “The direct-to-indirect band gap crossover in two-dimensional van der Waals Indium Selenide crystals”, Sci. Rep. **6**, 39619 (2016).

[120] L. V. Butov et al., “Magneto-optics of the spatially separated electron and hole layers in GaAs/Al_xGa_{1-x}As coupled quantum wells”, Phys. Rev. B **60**, 8753–8758 (1999).

[121] B. Laikhtman and R. Rapaport, “Exciton correlations in coupled quantum wells and their luminescence blue shift”, Phys. Rev. B **80**, 195313 (2009).

[122] P. Nagler et al., “Interlayer exciton dynamics in a dichalcogenide monolayer heterostructure”, 2D Mater. **4**, 025112 (2017).

[123] B. Miller et al., “Long-Lived Direct and Indirect Interlayer Excitons in van der Waals Heterostructures”, Nano Lett. **17**, 5229–5237 (2017).

[124] M. Brotons-Gisbert et al., “Out-of-plane orientation of luminescent excitons in two-dimensional indium selenide”, Nat. Commun. **10**, 3913 (2019).

[125] D. J. Terry et al., “Infrared-to-violet tunable optical activity in atomic films of GaSe, InSe, and their heterostructures”, 2D Mater. **5**, 041009 (2018).

[126] P. V. Nguyen et al., “Visualizing electrostatic gating effects in two-dimensional heterostructures”, Nature **572**, 220–223 (2019).

[127] N. R. Wilson et al., “Determination of band offsets, hybridization, and exciton binding in 2d semiconductor heterostructures”, Sci. Adv. **3**, e1601832 (2017).

[128] Y. Zhang et al., “Experimental observation of the quantum Hall effect and Berry’s phase in graphene”, Nature **438**, 201–204 (2005).

[129] B. Huang et al., “Layer-dependent ferromagnetism in a van der Waals crystal down to the monolayer limit”, Nature **546**, 270–273 (2017).

[130] R. V. Gorbachev et al., “Hunting for Monolayer Boron Nitride: Optical and Raman Signatures”, Small **7**, 465–468 (2011).

[131] M. H. Alam et al., “Lithium-ion electrolytic substrates for sub-1V high-performance transition metal dichalcogenide transistors and amplifiers”, Nature Communications **11** (2020).

[132] Q. Zhao et al., “Thickness Identification of Thin InSe by Optical Microscopy Methods”, Advanced Photonics Research **1**, 2000025 (2020).

[133] N. J. G. Couto, B. Sacépé, and A. F. Morpurgo, “Transport through Graphene on $SrTiO_3$”, Phys. Rev. Lett. **107**, 225501 (2011).

[134] N. S. Taghavi et al., “Thickness determination of MoS_2, $MoSe_2$, WS_2 and WSe_2 on transparent stamps used for deterministic transfer of 2D materials”, Nano Res. **12**, 1691–1695 (2019).

[135] K. Nakajima et al., “Lithium Ion Conductive Glass Ceramics: Properties and Application in Lithium Metal Batteries”, 28 (2010).

[136] H. Li et al., “Rapid and Reliable Thickness Identification of Two-Dimensional Nanosheets Using Optical Microscopy”, ACS Nano **7**, 10344–10353 (2013).

[137] Y. Y. Wang et al., “Thickness identification of two-dimensional materials by optical imaging”, Nanotechnology **23**, 495713 (2012).

[138] A. Ishimaru, *Electromagnetic Wave Propagation, Radiation, and Scattering: From Fundamentals to Applications* (John Wiley & Sons, Oct. 2017).

[139] O. Stenzel, *The Physics of Thin Film Optical Spectra: An Introduction*, 2nd ed., Springer Series in Surface Sciences (Springer International Publishing, 2016).

[140] M. (M. Fox, *Optical properties of solids*, Second edition., Oxford master series in physics ; 3. Condensed matter physics (Oxford University Press, 2010).

[141] C. Hsu et al., “Thickness-Dependent Refractive Index of 1L, 2L, and 3L MoS_2, $MoSe_2$, WS_2, and WSe_2”, Advanced Optical Materials **7**, 1900239 (2019).

[142] D. Domaretskiy et al., “Quenching the band gap of 2D semiconductors with a perpendicular electric field”, arXiv:2108.06117 [cond-mat] (2021).

[143] K. S. Novoselov et al., “Two-dimensional atomic crystals”, PNAS **102**, 10451–10453 (2005).

[144] N. D. Drummond, V. Zólyomi, and V. I. Fal’ko, “Electrically tunable band gap in silicene”, Physical Review B **85**, 075423 (2012).

[145] T. Chu et al., “Electrically Tunable Bandgaps in Bilayer MoS_2”, Nano Lett. **15**, 8000–8007 (2015).

[146] J. Kim et al., “Observation of tunable band gap and anisotropic Dirac semimetal state in black phosphorus”, Science **349**, 723–726 (2015).

[147] B. Deng et al., “Efficient electrical control of thin-film black phosphorus bandgap”, Nature Communications **8**, 14474 (2017).

[148] H. Overweg et al., “Electrostatically Induced Quantum Point Contacts in Bilayer Graphene”, Nano Letters **18**, 553–559 (2018).

[149] P. Chen et al., “Band evolution of two-dimensional transition metal dichalcogenides under electric fields”, Appl. Phys. Lett. **115**, 083104 (2019).

[150] O. Zheliuk et al., “Josephson coupled Ising pairing induced in suspended MoS_2 bilayers by double-side ionic gating”, Nat. Nanotechnol. **14**, 1123–1128 (2019).

[151] Y. Yamada et al., “Electrically induced ferromagnetism at room temperature in cobalt-doped titanium dioxide”, Science **332**, 1065–1067 (2011).

[152] J. T. Ye et al., “Superconducting Dome in a Gate-Tuned Band Insulator”, Science **338**, 1193–1196 (2012).

[153] S. Wang et al., “Hopping transport and the Hall effect near the insulator–metal transition in electrochemically gated poly(3-hexylthiophene) transistors”, Nature Communications **3**, 1210 (2012).

[154] J. M. Lu et al., “Evidence for two-dimensional Ising superconductivity in gated MoS_2”, Science **350**, 1353–1357 (2015).

[155] D. Costanzo et al., “Gate-induced superconductivity in atomically thin MoS_2 crystals”, Nature Nanotechnology **11**, 339–344 (2016).

[156] C. Leighton, “Electrolyte-based ionic control of functional oxides”, Nature Materials **18**, 13–18 (2019).

[157] E. Ponomarev et al., “Semiconducting van der waals interfaces as artificial semiconductors”, Nano Letters **18**, 5146–5152 (2018).

[158] H. Ji et al., “Thickness effect on low-power driving of MoS_2 transistors in balanced double-gate fields”, Nanotechnology **31**, 255201 (2020).

[159] Y. Wang et al., “Structural phase transition in monolayer $MoTe_2$ driven by electrostatic doping”, Nature **550**, 487–491 (2017).

[160] F. Zhang et al., “Electric-field induced structural transition in vertical $MoTe_2$- and $Mo_{1-x}W_xTe_2$-based resistive memories”, Nature Materials **18**, 55–61 (2019).

[161] D. Kim et al., “Drastic change of magnetic anisotropy in Fe_3GeTe_2 and Fe_4GeTe_2 monolayers under electric field studied by density functional theory”, Scientific Reports **11**, 17567 (2021).

[162] A. T. Hanbicki et al., “Double Indirect Interlayer Exciton in a $MoSe_2/WSe_2$ van der Waals Heterostructure”, ACS Nano **12**, 4719–4726 (2018).

[163] J. Zultak et al., “Ultra-thin van der Waals crystals as semiconductor quantum wells”, arXiv:1910.04215 [cond-mat] (2019).

[164] J. Camassel et al., “Excitonic absorption edge of indium selenide”, Phys. Rev. B **17**, 4718–4725 (1978).

[165] S. Jo et al., “Mono- and Bilayer WS_2 Light-Emitting Transistors”, Nano Lett. **14**, 2019–2025 (2014).

[166] Y. Saito, T. Nojima, and Y. Iwasa, "Gate-induced superconductivity in two-dimensional atomic crystals", Superconductor Science and Technology **29**, 093001 (2016).

[167] W. Shi et al., "Superconductivity Series in Transition Metal Dichalcogenides by Ionic Gating", Scientific Reports **5**, 12534 (2015).

[168] J. P. Perdew, K. Burke, and M. Ernzerhof, "Generalized Gradient Approximation Made Simple", Physical Review Letters **77**, 3865–3868 (1996).

[169] P. Giannozzi et al., "QUANTUM ESPRESSO: a modular and open-source software project for quantum simulations of materials", Journal of Physics: Condensed Matter **21**, 395502 (2009).

[170] P. Giannozzi et al., "Advanced capabilities for materials modelling with Quantum ESPRESSO", Journal of Physics: Condensed Matter **29**, 465901 (2017).

[171] D. R. Hamann, "Optimized norm-conserving Vanderbilt pseudopotentials", Physical Review B **88**, 085117 (2013).

[172] M. J. van Setten et al., "The PseudoDojo: Training and grading a 85 element optimized norm-conserving pseudopotential table", Computer Physics Communications **226**, 39–54 (2018).

[173] T. Sohier, M. Calandra, and F. Mauri, "Density functional perturbation theory for gated two-dimensional heterostructures: Theoretical developments and application to flexural phonons in graphene", Physical Review B **96**, 075448 (2017).

[174] G. Pizzi et al., "Wannier90 as a community code: new features and applications", Journal of Physics: Condensed Matter **32**, 165902 (2020).

[175] P. Borlido et al., "Large-Scale Benchmark of Exchange–Correlation Functionals for the Determination of Electronic Band Gaps of Solids", Journal of Chemical Theory and Computation **15**, 5069–5079 (2019).

[176] Y. Li et al., "Accurate identification of layer number for few-layer WS_2 and WSe_2 via spectroscopic study", Nanotechnology **29**, 124001 (2018).